Universidade do Minho

Escola de Ciências

Joana Francisca Marinho Parente Ribeiro

Development of exosome-inspired nanovectors for RNA delivery

outubro de 2023

Development of exosome-inspired nanovectors for RNA delivery

Joana Francisca Marinho Parente Ribeiro

UMinho | 2023

Universidade do Minho
Escola de Ciências

Joana Francisca Marinho Parente Ribeiro

Development of exosome-inspired nanovectors for RNA delivery

Dissertação de Mestrado
Mestrado em Bioquímica Aplicada

Trabalho efetuado sob a orientação da
Professora Doutora Andreia Ferreira de Castro Gomes e do
Doutor Ivo Edgar Araújo Lopes

outubro 2023

COPYRIGHT AND TERMS OF USE OF THE WORK BY THIRD PARTIES

This is an academic work that can be used by third parties as long as they respect internationally accepted rules and good practices, with regard to copyright and related rights. Thus, the work may be used under the terms of the license indicated below.

If the user needs permission to use the work under conditions not provided for in the licensing, should contact the author through the RepositóriUM of the University of Minho.



Atribuição-NãoComercial-SemDerivações

CC BY-NC-ND

https://creativecommons.org/licenses/by-nc-nd/4.0/

Acknowledgments

Em primeiro lugar, um agradecimento muito especial à Professora Doutora Andreia Gomes, a minha orientadora, pela oportunidade de realizar esta dissertação com um tema atual, interessante e muito desafiante, que me ajudou a crescer a nível profissional. Agradeço ainda todo o apoio, todos os desafios que me propôs e por acreditar nas minhas capacidades. Agradeço também o rigor científico que me incutiu e todas as aprendizagens que levei deste ano, que tão úteis foram para o desenvolvimento desta dissertação, como para o resto da minha carreira profissional.

Ao Doutor Ivo Lopes, o meu segundo orientador, agradeço também pelas críticas construtivas e assertivas e por toda a ajuda disponibilizada neste percurso.

Ao Mário agradeço por todo o apoio incondicional que me dedicou durante este ano de dissertação. Graças ao seu grande profissionalismo, levo comigo várias aprendizagens. Um obrigada não chega por todo o suporte, todo o empenho e força que me foram dados. Ao Henrique tenho a agradecer, também por toda a ajuda no decorrer deste ano, por estar sempre presente e por me apoiar contra todos os desafios. Não podia estar mais grata por ter tido o Mário e o Henrique, dois amigos, a acompanhar o meu trabalho durante este ano, pois estar rodeada de pessoas como eles, que proporcionam conhecimento e bom ambiente de trabalho torna tudo mais fácil.

À Anabela e à Vanessa por estarem também sempre presentes e prontamente disponíveis quando precisei e por estarem sempre lá para me esclarecer dúvidas. Foram um apoio indispensável no decorrer deste ano e estou muito agradecida por ter tido a oportunidade de trabalhar perto de vocês.

Um agradecimento muito grande aos meus colegas, Ana Paula, Erica, Inês, Nelson, Cristina, e Bruna, que foram indispensáveis neste percurso e estou muito feliz terem estado presentes no decorrer da minha dissertação. Obrigada, também, a vocês por todo o apoio e por terem sempre uma palavra amiga.

Um agradecimento especial às minhas amigas por me ajudarem em mais uma etapa da minha vida.

Aos meus pais e à minha irmã por serem o meu maior apoio em tudo o que faço. Tenho uma sorte enorme por vos ter na minha vida.

STATEMENT OF INTEGRITY

I hereby declare having conducted this academic work with integrity. I confirm that I have not used plagiarism or any form of undue use of information or falsification of results along the process leading to its elaboration.

I further declare that I have fully acknowledged the Code of Ethical Conduct of the University of Minho.

Desenvolvimento de exosomas inspirados em nanovetores para entrega de RNA

Resumo

As doenças neurodegenerativas, como a doença de Alzheimer (DA), são uma preocupação crescente na saúde pública, como resultado da falta de tratamentos que impedem a progressão da doença e também, devido à complexa fisiopatologia da DA que ainda não é completamente compreendida. Sabe-se, no entanto, que a acumulação no cérebro das proteínas Aβ e Tau são marcas características da DA, tal como a elevada acumulação de espécies reativas de oxigénio e a maior atividade da acetilcolinesterase (AChE) nos neurónios. A terapia baseada no ácido ribonucleico (ARN) é uma ferramenta recente, que poderá mudar o padrão de tratamento de muitas doenças, incluindo a DA. No entanto, o ARN necessita de um sistema de entrega seguro e eficaz para ultrapassar todos os obstáculos inerentes à sua entrega, e para permitir uma acumulação e libertação direcionada no cérebro. Lipossomas miméticos de exossomas (Exo-lip) são nanopartículas lipídicas que combinam as características desejáveis quer dos exossomas naturais, quer dos lipossomas, sendo um sistemas híbrido de entrega de moléculas, com benefícios únicos. Além das moléculas de ARN, estes sistemas também podem transportar outras moléculas com propriedades terapêuticas, como compostos naturais com bioatividades de interesse para o tratamento da DA (por exemplo, curcumina e petrosamina).

Para cumprir o objetivo principal desta tese, foram produzidos Exo-lip para entrega de ARN (siRNA ou mRNA), que foram caracterizados físico-quimicamente e testados, relativamente à sua estabilidade, em condições fisiológicas. Adicionalmente a internalização de Exo-lip, encapsulando siRNA e mRNA, foi confirmada na linha celular HEK293. Um modelo robusto de DA é um requisito essencial à compreensão dos mecanismos desta doença e, também, para testar medicamentos de modo eficaz. Deste modo, dois modelos de neurotoxicidade, induzida por alumínio, utilizando a linha celular de neuroblastoma SH-SY5Y e embriões de peixe-zebra, foram implementados para validar as diferentes terapias que se pretendiam testar. Estes modelos permitiram-nos confirmar a bioatividade dos Exo-lip, encapsulando siRNA anti-Tau e curcumina, na modulação de parâmetros que refletem as características da DA, como a atividade de AChE ou a expressão do gene Tau. Finalmente, a petrosamina isolada de uma esponja brasileira, por colaboradores do nosso grupo de investigação, foi testada diretamente nos dois modelos estabelecidos de DA, validando-a como um composto muito promissor para o tratamento desta doença, devido à sua elevada inibição da atividade da AChE.

Palavras-chave: Doença de Alzheimer, Lipossomas miméticos de exossomas, Terapia baseada em ARN, petrosamina

Development of exosome-inspired nanovectors for RNA delivery

Abstract

Neurodegenerative diseases such as Alzheimer's Disease (AD) are a rising public health concern, as a result of the lack of treatments to stop disease progression, and of the complex pathophysiology of the disease that is not completely understood. Nevertheless, it is known that the accumulation of Aβ and Tau proteins in the brain are characteristic hallmarks of AD, along with higher accumulation of reactive oxygen species and higher activity of acetylcholinesterase in the neurons.

RNA therapy is a rapidly expanding category of therapy that will change the standard of care for many diseases, including AD. However, RNA needs a safe and effective delivery system to mitigate all the hindrances inherent to its delivery, and to allow a targeted accumulation and release in the brain.

Exosome-like liposomes are lipid nanoparticles that combine the desirable features of natural exosomes and liposomes, leading to an advanced delivery systems with unique benefits. Additionally, besides RNA molecules, these systems may also carry other therapeutic cargos, such as natural compounds with bioactivities of interest to AD treatment (e.g. curcumin and petrosamine).

To accomplish the main objective of this thesis, exosome-like liposomes loaded with RNA (siRNA or mRNA) were produced, characterized physicochemically and their stability was tested in physiological conditions. The uptake of labelled exosome-like liposomes, encapsulating siRNA and mRNA, was confirmed in HEK293 cells.

A robust AD model is a primary requirement to understand the underlying mechanisms of the disease and to conduct effective drug screening. Therefore, in this work, two AD-like aluminium induced neurotoxicity models, using the neuroblastoma cell line SH-SY5Y and zebrafish embryos, were implemented to validate the different therapeutic solutions we intended to test. This enables us to confirm the bioactivity of exosome-like liposomes, loaded with anti-Tau siRNA and natural compound curcumin, in modulating parameters that mirror hallmarks of AD, such as AChE activity or Tau gene expression, in the established in vitro and in vivo neurotoxicity models. Finally, petrosamine, which was isolated de novo from a Brazilian sponge by collaborators, was directly tested in the two established AD models, validating it as a very promising compound for AD treatment, due to its potent AChE activity inhibition.

Keywords: Alzheimer's disease, Exosome-like liposomes, RNA therapy, petrosamine

TABLE OF CONTENTS

Resumo IV

Abstract V

Abbreviations IX

Figure Index XI

Table Index XIV

Equation Index XV

1. Introduction 1

1.1 Neurodegenerative diseases 1

1.2 Alzheimer's Disease 3

1.2.1 Amyloid-beta plaques 4

1.2.2 Tau protein 5

1.2.3 Accumulation of Reactive Oxygen Species 6

1.2.4 Dysregulated acetylcholinesterase activity 7

1.3 Challenges in the treatment of AD 8

1.3.1 Blood-Brain Barrier 8

1.4 Establishment of an AD model 10

1.4.1 The involvement of Aluminium in AD 11

1.4.2 AD model in neuroblastoma cell line 12

1.4.3 AD model in zebrafish embryos 13

1.5 Therapeutic natural compounds for AD 13

1.5.1 Petrosamine 14

1.5.2 Curcumin 14

1.6 RNA-based therapeutics 15

1.6.1 Types of RNA therapeutics 15

1.6.2 RNA-based therapeutics for AD: siRNA and mRNA 17

1.7 Nanotechnology: Application of Delivery systems 19

1.7.1 Promising delivery systems for brain delivery 20

1.7.2 Exosomes 21

1.7.3 Exosome-like liposomes 23

2. Objective 24

3. Materials and Methods 25

3.1 Materials 25

3.2 Cell culture 25

3.2.1 HEK293 cell line 25

3.2.2 SH-SY5Y cell line 25

3.3 AD Model in neuroblastoma cell line SH-SY5Y 26

3.3.1 Cell viability - Resazurin assay 26
3.3.2 Cell viability – SRB assay 26
3.3.3 Acridine Orange (AO)/ Propidium Iodide (PI) assay 27
3.3.4 Determination of the Reactive Oxygen Species by the DCFDA assay 27
3.3.5 Determination of Lipid Peroxidation 28
3.3.6 Determination of AChE activity 28
3.4 AD Model in zebrafish embryos 30
3.4.1 Zebrafish Embryo Maintenance 30
3.4.2 Embryo treatment for Fish Embryo Test (FET) 30
3.4.3 Phenotypic Parameters evaluation 31
3.4.4 Ethical statement 32
3.4.5 Analysis of Apoptosis 32
3.4.6 Determination of lipid peroxidation 32
3.4.7 Determination of the AChE activity 32
3.5 Exosome-like liposomes 34
3.5.1 Production of exosome-like liposomes for RNA delivery 35
3.5.2 Exosome-like liposome's purification by molecular size exclusion chromatography 35
3.5.3 Physical characterization of the exosome-like liposomes 36
3.5.3.1 Size and polydispersity determination by dynamic light scattering (DLS) 36
3.5.3.2 Surface charge measurement by electrophoretic light scattering (ELS) 37
3.5.4 Determination of exosome-like liposome's cholesterol 38
3.5.5 Encapsulation efficiency of mRNA 38
3.5.6 Stability of exosome-like liposomes 39
3.5.7 Exosome-like liposomes hemolysis 40
3.5.8 Uptake of exosome-like liposomes for siRNA delivery 40
3.5.9 Transfection of Luciferase mRNA 41
3.6 Strategies for the treatment of AD after stablished AD models 41
3.6.1 Delivery of exosome-like liposomes loaded with anti-Tau siRNA and curcumin *in vitro* 41
3.6.2 Delivery of exosome-like liposomes loaded with anti-Tau siRNA and curcumin *in vivo* 42
3.6.3 Petrosamine as a therapy for AD 42
3.6.3.1 Biocompatibility of petrosamine 42
3.6.3.2 Effect of petrosamine in the established neuroblastoma cell line AD model 43
3.6.3.3 Effect of petrosamine in the established zebrafish embryos AD model 43
3.7 Statistical Analyses 43
4. Results 44
4.1 Establishment of AD model in neuroblastoma cell line 44
4.1.1 Resazurin assay 44
4.1.2 SRB assay 45

4.1.3 Acridine Orange (AO)/ Propidium Iodide (PI) assay 46
4.1.4 Determination of Reactive Oxygen Species - DCFDA assay 48
4.1.5 Determination of lipid peroxidation 49
4.1.6 Determination of AChE activity 50
4.2 Establishment of AD model in zebrafish embryos 51
4.2.1 Survival rate and Hatching rate of zebrafish embryos 51
4.2.2 Phenotypic Parameters of zebrafish embryos 52
4.2.3 Analysis of Apoptosis 55
4.2.4 Determination of Lipid peroxidation 58
4.2.5 Determination of AChE activity 59
4.3 Characterization of exosome-like liposomes for RNA delivery 61
4.3.1 Size, PDI and zeta potential of exosome-like liposomes loaded with RNA 61
4.3.2 Encapsulation efficiency of mRNA 62
4.3.3 Stability in physiological conditions 62
4.3.3.1 Stability with HEPES pH 7.4 at 37°C 62
4.3.3.2 Stability with HEPES pH 5.0 at 37°C 63
4.3.3.3 Stability with FBS at 37°C 64
4.3.4 Hemolysis of empty exosome-like liposomes 65
4.3.5 Uptake of exosome-like liposomes with siRNA in the HEK293 cell line 65
4.3.6 Transfection of Luciferase mRNA 67
4.4 Strategies for the treatment of AD after stablished AD models 67
4.4.1 Delivery of loaded anti-Tau siRNA and curcumin exosome-like liposomes *in vitro* 68
4.4.1.2 LDH activity 68
4.4.1.2 RT-PCR 69
4.4.2 Delivery of loaded anti-Tau siRNA and curcumin exosome-like liposomes *in vivo* 70
4.4.2.1 Cardiac Frequency 70
4.4.2.2 Measurement of AChE activity 72
4.4.3 Petrosamine as a promising therapy for AD 73
4.4.3.1 Biocompatibility of Petrosamine 73
4.4.3.2 Effect of petrosamine in the established AD model *in vitro* 74
4.4.3.3 Effect of petrosamine in AD model *in vivo* 75
5. Discussion 77
6. Conclusion and Future Perspectives 84
7. References 86

Abbreviations

Aβ	Amyloid-beta
$AlCl_3$	Aluminium chloride
AChE	Acetylcholinesterase
AD	Alzheirmer's Disease
Alu	Aluminium
AO	Acridine Orange
APP	Amyloid Precursor Protein
ASO	Antisense Oligonucleotide
CNS	Central Nervous System
BACE1	Beta Secretase Enzyme
BBB	Blood Brain Barrier
BSA	Bovine Serum Albumin
DMEM	Dulbecco's Modified Eagle Medium
DLS	Dynamic Light Scattering
DODAP	1,2-dioleoyl-3- dimethylammonium-propane
DPPC	Dipalmitoylphosphatidylcholine
DTNB	5-5'-dithiobis(2-nitrobenzoic acid)
ELS	Electrophoretic Light Scattering
FBS	Fetal Bovine Serum
FDA	Food and Drug Administration
FET	Fish Embryo Test
hpf	Hours-post fertilization
KPBS	potassium phosphate buffer solution
MDA	Malondialdehyde
mRNA	Messenger RNA
miRNA	microRNA
n	Independent Experiments

NDDs	Neurodegenerative Diseases
NFTs	Neurofibrillary Tangles
PDI	Polydispersity Index
PI	Propidium Iodide
ROS	Reactive Oxygen Species
siRNA	small interfering RNA
SRB	Sulforhodamine B
SOP	Standard Operation Procedure
SD	Standard Deviation
TBARS	Thiobarbituric acid
TNB	5-thio-2-nitrobenzoic acid

Figure Index

Figure 1. Hallmarks of neurodegenerative diseases.

Figure 2. Molecular factors associated with Alzheimer's disease pathogenesis. Created with BioRender.com.

Figure 3. Amyloid precursor protein (APP) process that leads to the accumulation of neurotoxic Aβ plaques by the amyloidogenic pathway. Created with BioRender.com.

Figure 4. Irregular hyperphosphorylation of Tau protein leads to the formation of neurofibrillary tangles (NFTs) Created with BioRender.com.

Figure 5. Schematic diagram of BBB structure. Created with BioRender.com.

Figure 6. Effects of aluminium on the central nervous system. Created with BioRender.com.

Figure 7. Mechanism of action of the RNA-based therapies. Diverse cellular molecules can be targeted by RNA therapy. Created with BioRender.com.

Figure 8. How delivery systems overcome the limitations of free RNA. Created with BioRender.com.

Figure 9: Scheme of the natural exosome's formation and their composition. Created with BioRender.com.

Figure 10. Ellman's reaction to detect AChE activity. Created with ChemDraw.

Figure 11. Standard protein curve of BSA solutions at different concentrations.

Figure 12. Different zebrafish embryo phenotypic parameters measured and corresponding timepoints they were observed. Created with Biorender.com.

Figure 13. Standard protein curve of BSA solutions at different concentrations.

Figure 14. Representation of the polydispersity index. Schematic representation of typical particle size graphs indicating a (a) polydisperse sample and (b) a monodisperse sample. Representation of the particle size distribution of a sample containing a (c) polydisperse population of particles (with a high PDI value); and (d) a sample containing a monodisperse population of particles (with a low PDI value).

Figure 15. Calibration curve of cholesterol.

Figure 16. Calibration curve of mRNA to identify mRNA encapsulation efficiency in exosome-like liposomes.

Figure 17. Cell viability (**3n**) after SH-SY5Y cell's exposure to three different concentrations of $AlCl_3$ (50 μM, 200 μM, and 1000 μM) for 24h. The results were expressed in relation to negative control (100%). Significant differences were identified ** $p < 0.01$, *** $p < 0.001$, **** $p < 0.0001$ as compared to negative control.

Figure 18. Cell viability (**3n**) after SH-SY5Y cell's exposure to three different concentrations of $AlCl_3$ (50 μM, 200 μM, and 1000 μM) for 24h. The results were expressed in relation to negative control (100%). No significant statistical differences were detected.

Figure 19. Microscopy of fluorescence of AO/PI assay showing SH-SY5Y cell line exposed to different concentrations of $AlCl_3$ for 24h. (a) Negative Control; (b) 50 μM $AlCl_3$; (c) 200 μM $AlCl_3$; (d) 200 μM $AlCl_3$; (e) Positive Control (30% DMSO). Scale bar = 50 μm. Graph (f) represents the number of viable cells (green), early apoptotic cells (yellow), and apoptotic cells (red) in each condition.

Figure 20. Reactive oxygen species quantified with the DCFH-DA probe (**2n**) after SH-SY5Y cell's exposure to three different concentrations of $AlCl_3$ (50 μM, 200 μM, and 1000 μM) for 24h. Verified a significant statistical difference among means. ** $p < 0.01$, *** $p < 0.001$, **** $p < 0.0001$ as compared to the oxidant t-BHP (1mM).

Figure 21. Lipid peroxidation percentage (**3n**) after SH-SY5Y cell's exposure to three different concentrations of $AlCl_3$ (50 μM, 200 μM, and 1000 μM) for 24h. The results were expressed in relation to negative control (100%). No significant differences were detected.

Figure 22. AChE activity (**4n**) after SH-SY5Y cell's exposure to three different concentrations of $AlCl_3$ (50 μM, 200 μM, and 1000 μM) for 24h. Verified a significant statistical difference among means. * $p < 0.05$, *** $p < 0.001$ as compared to the negative control.

Figure 23. Analysis of zebrafish embryos development: (a) survival rate and (b) hatching rate.

Figure 24. Phenotypic parameters. (a) Epiboly percentage, (b) Yolk volume, (c) Pupil volume, (d) Cardiac frequency, and (e) Larvae length.

Figure 25. Zebrafish embryos submitted to 50 μM of $AlCl_3$ at (a) 6hpf, (b) 24hpf, (c) 48hpf, and (d) 72hpf. Arrow represents a pericardial edema.

Figure 26. Acridine orange staining in zebrafish larvae with 120 hpf. (a) Whole body of Control larvae; (b) Whole body of larvae exposed to 50 μM $AlCl_3$; (c) Whole body of larvae exposed to 200 μM $AlCl_3$; and (d) Total fluorescence of green spots spots indicating identified apoptotic cells. Particular fluorescent cellular accumulations are indicated by arrows. Scale bar= 500 μm.

Figure 27. Schematic overview of the lateral line in zebrafish. (a) Location of the neuromasts in a zebrafish larva at 120 hpf. (b) Location of the neuromasts under apoptosis of zebrafish larvae submitted to 50 μM of $AlCl_3$ at 120 hpf. The neuromasts, the anterior and posterior sensory ganglia and the projections they send to the neuromasts and into the brain are indicated.

Figure 28. Lipid peroxidation percentage of whole body of larvae with 120 hpf after exposure to two different concentrations of $AlCl_3$ (50 μM and 200 μM). Not verified a significant difference among means.

Figure 29. AChE activity of whole body of larvae with 120 hpf after exposure to two different concentrations of $AlCl_3$ (50 μM and 200 μM). Verified a significant statistical difference in $AlCl_3$ 50 μM * $p < 0.05$ as compared to the control.

Figure 30. Characterization of empty exosome-like liposomes, exosome-like liposomes loaded with siRNA, and exosome-like loaded with mRNA. (a) Size and polydispersity index (PDI); (b) ζ-potential.

Figure 31. Stability of siRNA-loaded liposomes in HEPES pH 7.4 at 37°C. (a) Size and PDI. (b) ζ-potential.

Figure 32. Stability of siRNA-loaded liposomes in HEPES pH 5.0 at 37°C. (a) Size and PDI. (b) ζ-potential.

Figure 33. Stability of siRNA-loaded liposomes in FBS at 37°C. (a) Size and PDI. (b) ζ-potential.

Figure 34. Evaluation of toxicity in erythrocytes incubated with empty exosome-like liposomes.

Figure 35. Internalization of exosome-like liposomes with siRNA stained with Oil Red O in 293T cells by microscopy of fluorescence in brightfield at (a) 1h, (c) 3h, (e) 4h and in TRITC filter at (b) 1h, (d) 3h, (f) 4h. Scale bar = 100 μm.

Figure 36. LDH activity (**1n**) after SH-SY5Y cell's exposure to 200 μM for 24h and further treatment with loaded exosome-like liposomes anti-Tau siRNA and curcumin for 24h.

Figure 37. Fold change expression of Tau gene in SH-SY5Y cells exposed to $AlCl_3$ at 200 μM with a posterior incubation with exosome-like liposomes with anti-tau siRNA and curcumin.

Figure 38. Cardiac frequency of zebrafish at 48, 72, 96 and 120 hpf. The embryos were submitted to (a) $AlCl_3$ 50 μM and to (b) $AlCl_3$ 200 μM the first 72 hpf and then treated with loaded exosome-like liposomes anti-Tau siRNA and curcumin until 120 hpf. Verified a significant difference among means. ** $p < 0.01$, **** $p < 0.0001$ as compared to the control.

Figure 39. AChE activity of zebrafish submitted to (a) $AlCl_3$ 50 μM and to (b) $AlCl_3$ 200 μM the first 72 hpf and then treated with loaded exosome-like liposomes anti-Tau siRNA and curcumin until 120 hpf. Verified a significant difference among means. * $p < 0.05$ and ** $p < 0.01$.

Figure 40. Biocompatibility of petrosamine. (a) Hemolysis assay and (b) Survival rate of zebrafish embryos.

Figure 41: AChE activity (**3n**) after SH-SY5Y cell's exposure to three different concentrations of $AlCl_3$ (50 μM, 200 μM, and 1000 μM) for 24h and then treated with petrosamine (c= 0.05 mg/ml) for 24h. Verified a significant difference among means. * $p < 0.05$, *** $p < 0.001$ as compared to negative control.

Figure 42. Lipid peroxidation percentage (**3n**) after SH-SY5Y cell's exposure to three different concentrations of $AlCl_3$ (50 μM, 200 μM, and 1000 μM) for 24h and then treated with petrosamine (c= 0.05 mg/ml) for 24h. The results were expressed in relation to negative control (100%). Not verified a significant difference among means.

Figure 43: Analysis of zebrafish embryos development: (a) survival rate and (b) hatching rate.

Figure 44: Effect of petrosamine after aluminium toxicity in zebrafish embryos yolk volume during 120 hpf.

Figure 45: Effect of petrosamine after aluminium toxicity in zebrafish embryos cardiac frequency during 120 hpf.

Figure 46: AChE activity of zebrafish embryos after exposure to two concentrations of $AlCl_3$ (50 and 200 μM) until 72 hpf, and then treated with petrosamine (c= 0.05 mg/ml), until 120 hpf. A significant difference among means was verified.**** $p < 0.0001$ as compared to negative control.

Table Index

Table 1. Available siRNA and mRNA therapeutical strategies for AD.

Table 2: Promising delivery system to target the CNS.

Table 3. Lipid percentage (mol:mol) and concentration of the stock solution of the various lipids used in the preparation of the exosome-like liposomes.

Table 4. Encapsulation efficiency of exosome-like liposomes loaded with mRNA.

Table 5. Luminescence measured in HEK293 cells transfected with Luciferase mRNA using transfecting agent Lipofectamine 2000.

Equation Index

Equation 1. Equation for the determination of AChE activity. ΔAbs_{sample} is the variation of the absorbance of the samples per minute; ΔAbs_{blank} is the variation of the absorbance of the blanks per minute; Vt/Vs (total volume/volume of sample) is the dilution factor of the samples in the wells; Prot is the protein concentration of the samples (mg/mL); ε is the molar extinction coefficient of TNB (13,600 M^{-1} cm^{-1}) at 412 nm; and *d* is the light path length.

Chapter 1

Introduction

1. Introduction

1.1 Neurodegenerative diseases

Neurodegenerative diseases (NDDs) are a pathologically, clinically, and genetically, heterogeneous group of neurological disorders, which adversely affect the lives of millions of people worldwide. NDDs are characterized by the progressive loss of neurons in the central nervous system (CNS)[1,2]. Neuronal death, leads to a collapsed structure and loss of functional neural networks that cannot be renewed, resulting in neurodegeneration[1,3]. Consequently, since the brain controls several aspects of the body's function, NDDs affect multiple facets of human functioning and limit the ability to perform both basic (e.g. movement, stability, and balance) and cognitive tasks (e.g. decision-making, language, and thinking)[3]. A few examples of NDDs are Alzheimer's disease (AD), Parkinson's disease, Huntington's disease, and amyotrophic lateral sclerosis.

Despite the phenotypic differences across these NDDs, there are striking similarities at the cellular and molecular levels, including (1) protein aggregation; (2) disrupted proteostasis; (3) neuroinflammation; (4) oxidative stress; (5) synaptic failure; and (6) DNA defects[1,4] (**figure 1**). A key pathological hallmark of a variety of NDDs involves the misfolding and aggregation of specific proteins into abnormal, toxic species, that often serve for disease classification[5].

The term "proteostasis" refers to the integrated activity of cellular mechanisms that regulate protein production, folding, trafficking, degradation, and clearance. In healthy cells, misfolded proteins undergo clearance by protein degradation systems, such as the ubiquitin-proteosome system. Under conditions of proteotoxic stress, cellular aging, or in the presence of disease mutations, proteins can escape a cell's quality control system and begin to aggregate into non-native structures, such as oligomers and amorphous assemblies of fibrils and plaques[4,5]. Reactive microglia and astrocytes lead to neuroinflammation when activated by other hallmarks of the NDDs[1]. Microglia are the primary immune cells of the brain, providing housekeeping functions, and defense mechanisms[4]. When these cells are activated due to signs of damage (e.g. protein aggregates and accumulation of oxidative stress) and function failure, it results in chronic inflammation that can promote the neurodegenerative process. Additionally, microglia interact with astrocytes, critical cells in the maintenance of a healthy brain, and are activated in the proximity of damaged neurons, leading to astrogliosis - a process where astrocytes become reactive in response to CNS damage and disease by secreting and responding to a variety of molecular factors.

Neurons are particularly susceptible to accumulation of reactive oxygen species (ROS), due to high oxygen consumption, and low antioxidant defences, leading to increased oxidation of proteins and nucleic acids, and lipid peroxidation[4]. Synapses are the functional part of the connection between neurons and the key part of the physiological function of neurons. However, when some peripheral factor affects synapses, it leads to synaptic loss, supressing brain learning and memory functions[6]. Additionally, the accumulation of DNA damage and defects in RNA metabolism have been assigned a critical role in a wide range of NDDs.

All these factors are understood as the chain of events leading to gradual loss of neurons' functional properties until cell death, and consequently, to neurodegeneration[1].

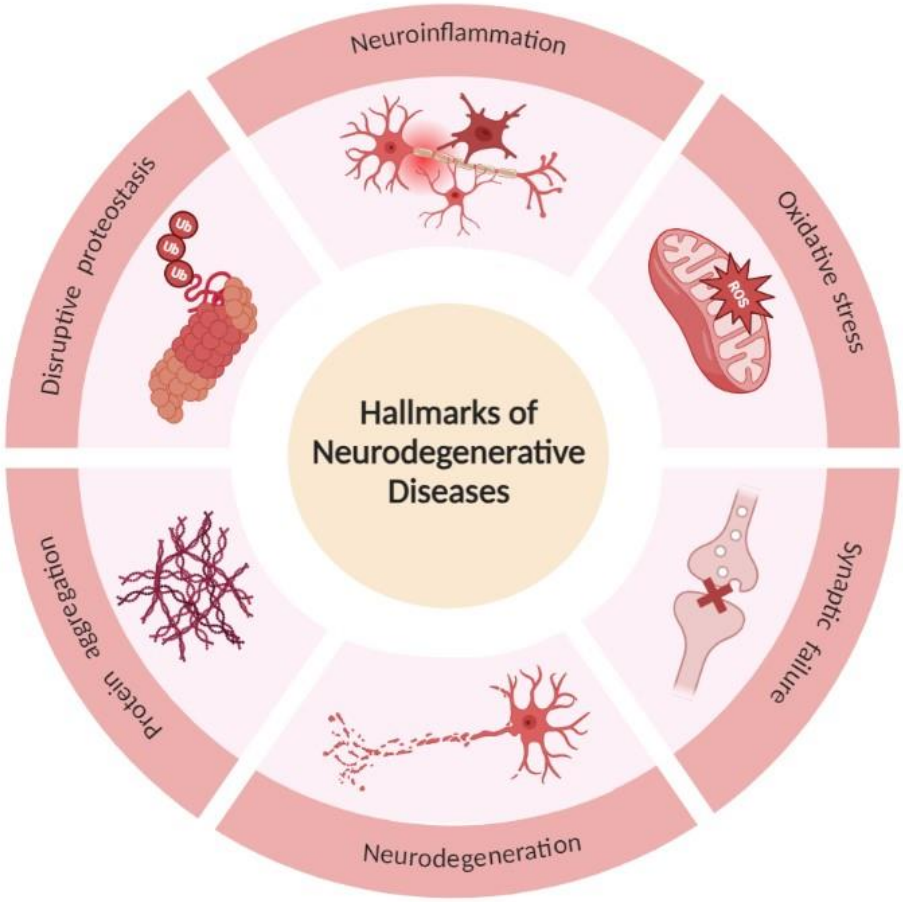


Figure 1. Hallmarks of neurodegenerative diseases.

1.2 Alzheimer's Disease

AD is a progressive neurodegenerative disorder characterized by initial memory loss, cognitive decline, affecting behaviour, speech, visuospatial orientation, and the motor system[7]. Ultimately, causing neuronal loss, brain atrophy, and death. AD is the most common form of dementia, accounting for 60 to 80% of the cases, and is quickly becoming one of the most expensive, lethal, and burdening diseases of this century[7,8].

According to World Health Organization (WHO)[9], AD and other forms of dementia were ranked as the 7th leading cause of death, in 2019. Globally, the incidence of AD and other dementias increased by 147.95% from 1990 to 2019, with 7.24 million cases in 2019[10]. People live longer, but unfortunately not all are able to enjoy healthy aging, once the primary factor is believed to be age, which is the root cause of AD development[11].

The pathophysiological development of AD is complex and multifactorial, and the exact mechanism remains unclear. At a molecular level, the progression of this disease is mainly characterized by the accumulation of two proteins: amyloid-beta (Aβ), that lead to the formation of Aβ plaques and neurofibrillary tangles (NFTs) composed by hyperphosphorylated Tau[3]. Additionally, there are a number of other hallmarks associated with AD (**figure 2**), including accumulation of reactive oxygen species, mitochondrial dysfunction, progressive decline in acetylcholine, and impaired acetylcholinesterase (AChE) activity - a key enzyme in the cholinergic nervous system[12]. Also, synapse loss is considered critical in AD and, to date, one of the main biological correlating factors to the cognitive decline caused by this disease[13]. This thesis will focus in the Aβ plaques, Tau protein, accumulation of ROS and AChE activity AD hallmarks.

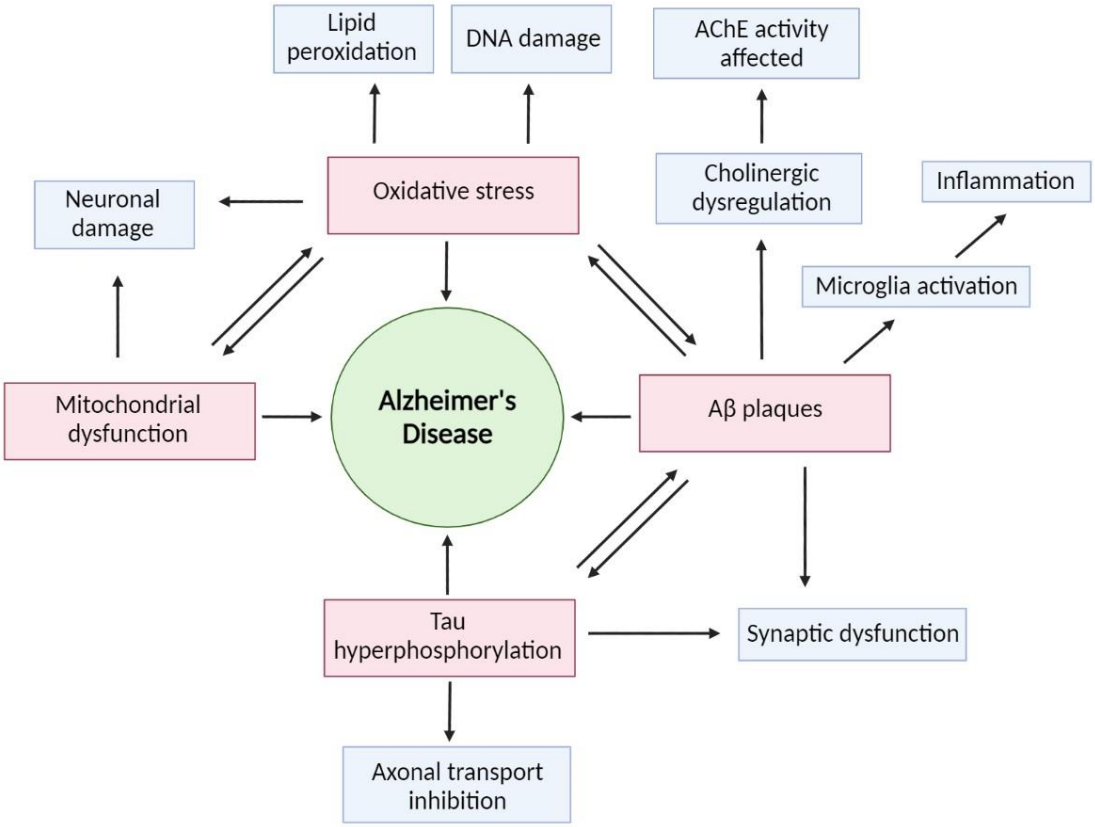


Figure 2. Molecular factors associated with Alzheimer's disease pathogenesis. Created with BioRender.com.

1.2.1 Amyloid-beta plaques

Aβ is the cleavage product of amyloid precursor protein (APP), a type I transmembrane protein that is expressed in various human tissues, including the brain. APP can be cleaved by a combination of different secretases complexes, following two pathways: the non-amyloidogenic and the amyloidogenic pathway[14,15] (**figure 3**). In the non-amyloidogenic pathway, there is the combined action of α- and γ-secretases, and soluble APPα is released. The amyloidogenic processing of APP is initiated by β-secretase (or β-site APP-cleaving enzyme 1 (BACE1)), instead of α-secretase, and afterwards γ-secretase generates Aβ peptides with two lengths, the $A\beta_{40}$ and $A\beta_{42}$ forms, the predominant form in amyloid plaques[15]. These oligomeric forms of Aβ are not cleared from the brain and aggregate to form insoluble Aβ plaques – neurotoxic protein aggregates. The molecular mechanisms underlying Aβ cytotoxicity are complex and not completely understood. However, established mechanisms that lead to synaptic dysfunction, dysregulation of cellular ionic homeostasis, either by modulation of glutamatergic, cholinergic dysregulation of metabolic pathways, inflammation, and oxidative stress have been documented[14,16,17].

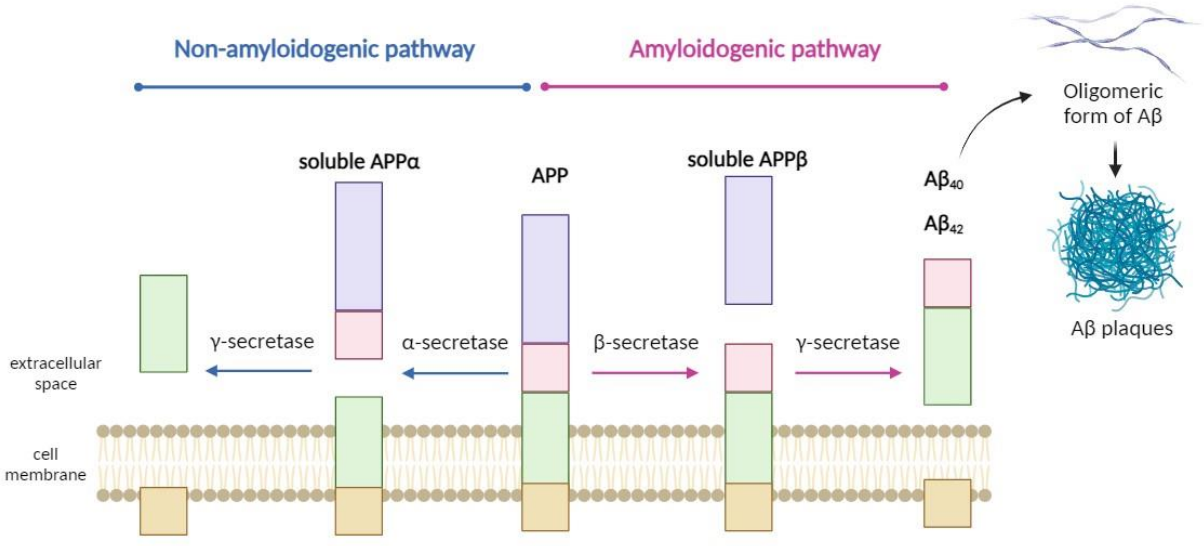


Figure 3. Amyloid precursor protein (APP) process that leads to the accumulation of neurotoxic Aβ plaques by the amyloidogenic pathway. Created with BioRender.com.

1.2.2 Tau protein

Tau protein is a microtubule-associated protein that supports the integrity and function of the microtubule to ensure proper cytoskeletal organization of neurons. It thus plays an important role in axonal transport and synaptic function[17,18]. In the brain, Tau is subjected to several post-translational modifications, being the phosphorylation of particular interest because of its involvement in AD[19]. Tau phosphorylation is essential for the neurons to maintain its normal physiological function. However, hyperphosphorylation of Tau plays a critical role in AD, since it undergoes through misfolding, aggregation and formation of NFTs (**figure 4**), leading to dysregulation of microtubule dynamics, axonal transport inhibition, synaptic failure and neuronal dysfunction[17,20]. It should be noted that the actual causes that lead to Tau hyperphosphorylation are still not clear[21]. Although Tau is mainly an intracellular protein, exosome driven extracellular Tau is also present in the brain, being that the spread of Tau aggregated assemblies may seed and promote aggregation along different brain regions[15].

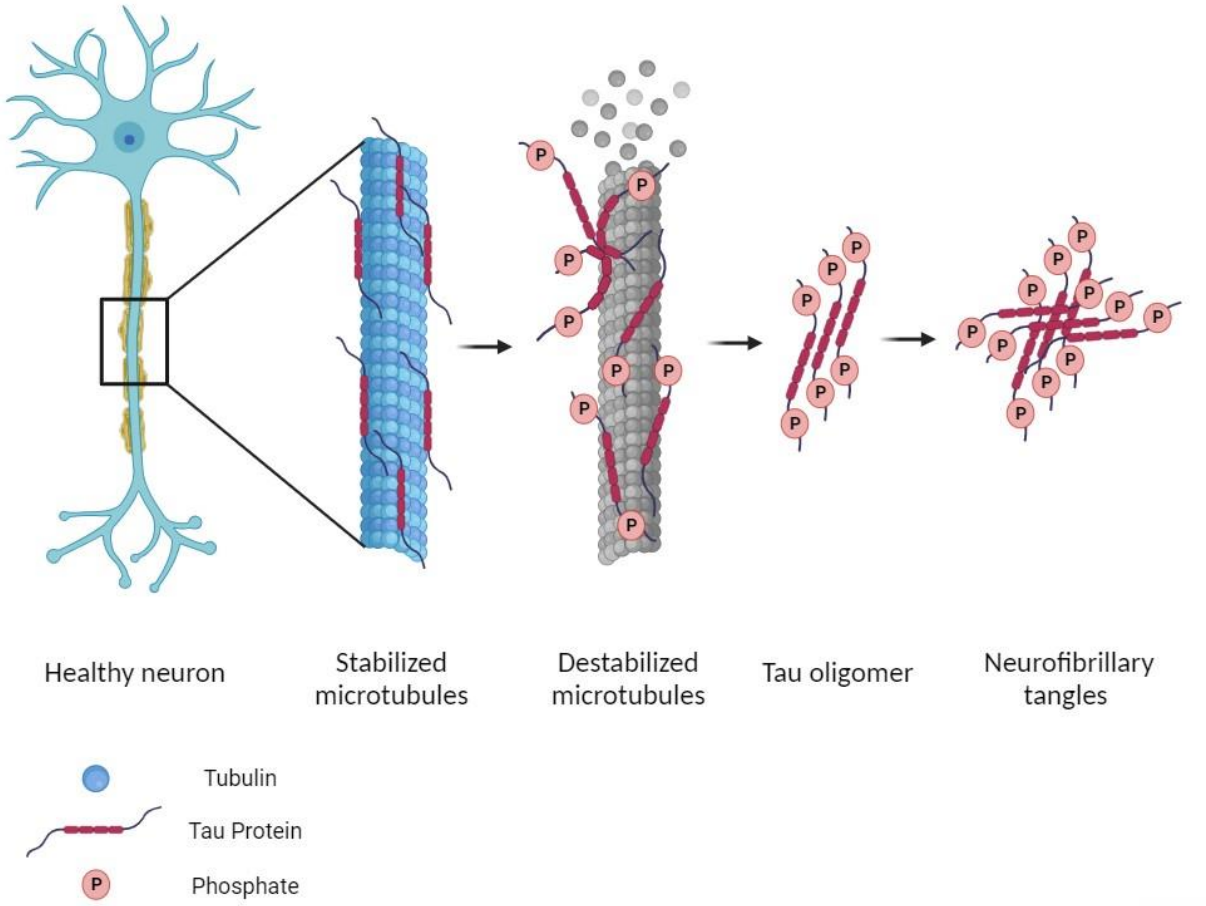


Figure 4. Irregular hyperphosphorylation of Tau protein leads to the formation of neurofibrillary tangles (NFTs) Created with BioRender.com.

1.2.3 Accumulation of Reactive Oxygen Species

ROS accumulation in neurodegenerative diseases, including AD, is induced by metal ions dyshomeostasis, mitochondrial dysfunction, glial cell activation, and protein misfolding, such as that observed with Aβ peptide, that has been reported to damage mitochondria and interfere with its functioning[22,23]. At the same time, the overproduction of ROS can also aggravate these four pathological processes[22].

The brain consumes high levels of oxygen but has a low level of antioxidants, being more susceptible to oxidative stress[24]. Apart from the low levels of antioxidant enzymes, neurons are also highly vulnerable to oxidative stress, since they are rich in phospholipids that contain polyunsaturated fatty acids. These phospholipids are engaged in the neuronal interaction and in the process of neurotransmission[25].

Studies have demonstrated that oxidative stress is responsible for the production of the high level of end products of lipid peroxidation, such as malondialdehyde (MDA) – an increased lipid in AD patients[25,26].

Under physiological conditions, the balance between the production of ROS and its clearance is extremely controlled. When the equilibrium is disturbed, due to pathogenic conditions, ROS levels rise and interfere with the function of biomolecules (nucleic acids, proteins, and lipids)[22,24]. Additionally, mitochondria, the powerhouse of the cell, are in increased levels in neurons, since they are needed for energy metabolism, buffering of calcium concentration for fundamental cellular processes, neurotransmission, and membrane potential generation[23]. Mitochondria are the main source of ROS generation, and any anomaly may not only damage several biomolecules, but also put the mitochondria themselves in a vulnerable situation to oxidative damage[25]. Ultimately, ROS can destroy the normal function of the cell, and induce neuronal apoptosis in the CNS[22,24].

1.2.4 Dysregulated acetylcholinesterase activity

The equilibrium of different neurotransmitters systems, such as acetylcholine, are essential for brain function, and, in the sense, acetylcholinesterase (AChE) plays a key role in the cholinergic nervous system[27]. AChE is located in the post-synaptic membrane of the cholinergic junctions, at the nerve level, and is the enzyme responsible for most of acetylcholine clearance[28].

In AD a deficient cholinergic neurotransmission, is involved in the pathophysiology of learning and memory impairment[27]. During the progression of this disease, many different types of neurons deteriorate, specially the forebrain cholinergic neurons, which is accompanied by a progressive decline in acetylcholine[12]. The decrease in acetylcholine levels can be due to an increased catalytic functioning of AChE[29]. Although the understanding of the relationship between AChE and the pathological features of AD is incomplete, increasing evidence suggests that both Aβ and NFTs can increase AChE activity[12]. At the moment, the enhancement of the cholinergic neurotransmission still represents a main approach in the treatment of symptoms of mild and moderate stages of AD[27].

1.3 Challenges in the treatment of AD

Despite all the scientific efforts, there are no available disease-modifying treatments for AD[30]. This neurodegenerative disease is among the pathologies that have the lowest rate of drug development success, with 99% of drug candidates being discontinued after showing no clinical benefit[17]. For years, only a few therapies were approved by Food and Drug Administration (FDA) for the treatment of this disease. Of these therapies, only three AChE inhibitors (donepezil, rivastigmine, galantamine) and one N-methyl-D-aspartate receptor antagonist (memantine) continue approved to date[27]. These therapies are symptomatic, having some effect on cognitive function only. A significant unmet medical need for treatments that focus on stopping the disease progression remains[30]. Two decades after memantine approval, FDA approved aducanumab in 2021, the first monoclonal antibody anti-Aβ. However, this new drug is expensive and there is some doubt related to its benefits[31].

The lack of success of novel disease-modifying treatments and failed clinical trials are due to an inadequate understanding of the complex pathophysiology of AD, which may necessitate a combination of treatments, rather than monotherapy[32,33]. This high failure rate can also be related to the premature translation of highly successful drugs in animal models that mirror only limited aspects of AD pathology to humans[34]. Additionally, AD diagnosis continues to be mainly based on clinical evaluation of cognitive and physical examination. However, pathological changes occur years before symptoms arise, and an earlier diagnosis should be accomplished[31]. Finally, this profound lack of progress in the treatment of AD can be attributed to the blood–brain barrier (BBB), a specialized barrier between the peripheral circulation and the CNS[35].

1.3.1 Blood-Brain Barrier

The BBB is constituted by blood vessels that vascularize the CNS and possess unique properties, which allow these vessels to tightly regulate the movement of ions, molecules, and cells between the blood and brain. Also, these vessels supply brain cells with oxygen, energy metabolites and nutrients and remove carbon dioxide and other metabolic waste products from the brain[35,36]. This precise control of CNS homeostasis allows proper neuronal function and protects the neural tissue from toxins and pathogens[36]. Around 98% of small molecule drugs do not cross the BBB, and ≈100% of biologic drugs do not cross the BBB, so BBB drug delivery technology is a urgent need in AD drug development[37].

The BBB is composed by endothelial cells, astrocytes, pericytes, neurons, and tight junctions[38] (**Figure 5**). Endothelial cells are the BBB's core anatomical structure for lining the cerebral blood vessels and interacting with different types of cells in the CNS. Endothelial cells present in the CNS have unique properties, when compared with endothelial cells in other tissues, allowing them to tightly regulate the movement of ions, molecules, and cells between the blood and the brain. These cells are held together by tight junctions, which greatly limit the paracellular flux of solutes and the endothelial monolayer is sheathed by pericytes and astrocyte end-feet[35,36]. Tight junctions are the main functional components in sustaining the permeability of the barrier and controlling tissue homeostasis. Astrocytes are glial cells, and their end feet link them with the basal membrane, via the binding of a set of proteins. In the CNS, they play a major role in dynamic signalling such as clearing waste, tuning brain blood flow, regulating vascular function, and balancing neuroimmune responses. Pericytes are central to the neurovascular unit function and because of the physical apposition, pericytes and endothelial cells are in close communication with each other[39].

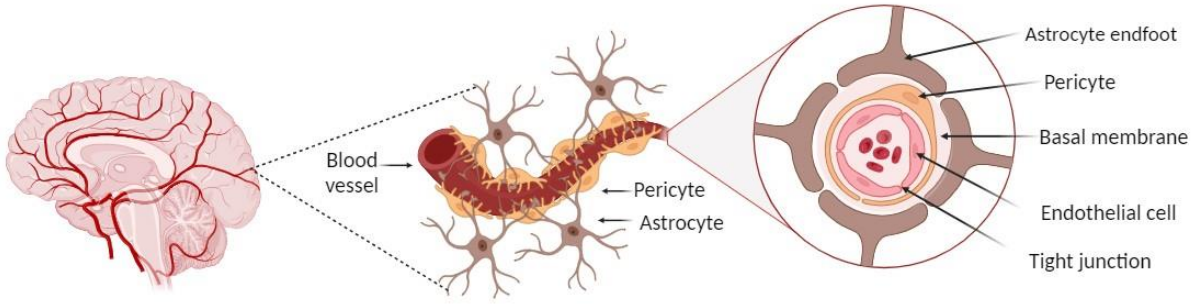


Figure 5. Schematic diagram of BBB structure. Created with BioRender.com.

1.4 Establishment of an AD model

The brain is one of the most complex organs in the human body due to its unique and structure and function. The development of effective therapeutics to treat AD is still a clinical challenge that has not been achieved so far, owing to a poor understanding of the disease. Consequently, there is a need for a model system that can reproduce the pathological and biochemical characteristics of AD with the aim to better study this pathology, and therefore allow adequate preclinical testing of novel therapeutics[40]. To study this disease, the most common experimental tools used are *in vitro* 2D and 3D models, and animal models[40,41].

2D cell culture systems are simplified platforms to understand biological processes under controlled conditions, and provide information about toxicity, inflammation, and neurodegeneration, with the activation of several cellular pathways[40,41]. However, these cell culture models do not accurately represent the complex environment that is found in the brain, which includes complex interactions between neurons and other cell types implicated in AD pathogenesis. Therefore, this obstacle is being partially addressed through the development of 3D cell culture models[34]. An ideal *in vivo* model of AD should have all the biochemical and behavioural characteristics of AD patients, as well as possessing reproducibility and robustness. Some examples are *Caenorhabditis elegans* (nematode), *Drosophila melanogaster* (fruit fly), *Danio rerio* (zebrafish) and transgenic *Mus musculus* (mice) and *Rattus norvegicus* (rats) that express human genes that result in the formation of Aβ plaques (by expression APP or in combination with human *PSEN1*) and NFTs (by expression of human *MAPT*)[34]. These rodents are very common in the research field of AD, since they provide a better understanding of behavioural changes and addresses the biological complexity of a living organism. Nevertheless, this model limits the accessibility to the tissue of interest, and present difficulties in real-time monitoring, and in measurements of biological changes occurring in AD[40]. Besides creating a model using genes that express certain AD hallmarks, various toxins have also been used to develop animal models of this disease. Several environmental toxins, including toxins produced by marine wildlife (e.g. cyanobacteria) act through a variety of molecular mechanisms, and are highly neurotoxic in humans[42]. Some of these toxins are saxitoxin, domoic acid, ciguatoxin, brevetoxin, tetrodotoxin, azaspiracid, mycrocistin, okadaic acid, and β-N-methylamino-L-alanine, which cause severe neurological symptoms in humans[43,44]. Other organic and inorganic substances have been identified as toxins that may cause cognitive decline. Examples of metal toxins include mercury, arsenic, cadmium, copper, zinc, iron and aluminium, playing an important role in Tau and Aβ metabolism and aggregation[45,46].

1.4.1 The involvement of Aluminium in AD

Whilst being environmentally abundant, aluminium (Alu) is not essential for life[47]. Actually, Alu is a recognized neurotoxin, causing various adverse effects in plants, animals, and humans. Although a direct relationship between Alu and AD has not been clearly demonstrated, evidence suggests that Alu exposure is linked to the progression of this neurodegenerative disease[48]. Mass spectrometry studies have demonstrated that Alu crosses the BBB and accumulates in a semipermanent manner, influencing more than 200 biologically relevant reactions and cause various adverse effects on the mammalian brain[49].

Alu can induce AD-like symptoms and be used as model for this disease[50], since it causes several adverse effects on the mammalian CNS, including crucial reactions for brain development such as the axonal transport, neurotransmitter synthesis, synaptic transmission, phosphorylation of proteins, protein degradation, gene expression, and inflammatory responses (**figure 6**)[47]. The involvement of Alu in AD came to light decades ago, when Klatzo *et al.* proved that injections of Alu salts into rabbit brain led to the formation of NFTs which appeared similar to the NFTs of AD. Since then, several studies have emerged, documenting the connection between Alu and AD, including a study by Savory *et al.* in which Al-maltolate treatment mimicked AD-like neuropathology in aged rabbits, by inducing Aβ deposition, NFTs, apoptosis, and oxidative stress in the brain[51].

In general, it has been reported that Alu induces mitochondrial dysfunction, and endoplasmic reticulum stress. Also, Alu causes the oligomerization of proteins, inducing conformational changes that can inhibit their degradation by proteases. This metal enhances the activity of the Tau kinases CDK5 and GSK-3β, inhibiting the dephosphorylation of Tau, and enhancing its aggregation[49]. Actually, strong binding of Alu to phosphorylated amino acids promotes the self-aggregation and accumulation of highly phosphorylated cytoskeleton proteins, including neurofilament and microtubule-associated proteins[47]. Although the effects of Alu on AD pathology were first attributed to its interaction with Tau, it was later demonstrated that it also affects Aβ by promoting its production, aggregation and by inhibiting its degradation[47,49]. Alu is preferentially taken up by glial cells, which induces the production of inflammatory cytokines (e.g. IL-6). Additionally, Alu leads to a higher production of ROS, stimulates iron-induced membrane lipid peroxidation, affects the cholinergic system, and ultimately causes the apoptotic death of both neurons and glial cells[49].

In this thesis, we propose the validation of two AD models induced by Alu toxicity: (1) AD model *in vitro* using a neuroblastoma cell line (which has not been reported yet) and (2) AD model *in vivo* with zebrafish embryos (implemented for the first time in our research laboratory).

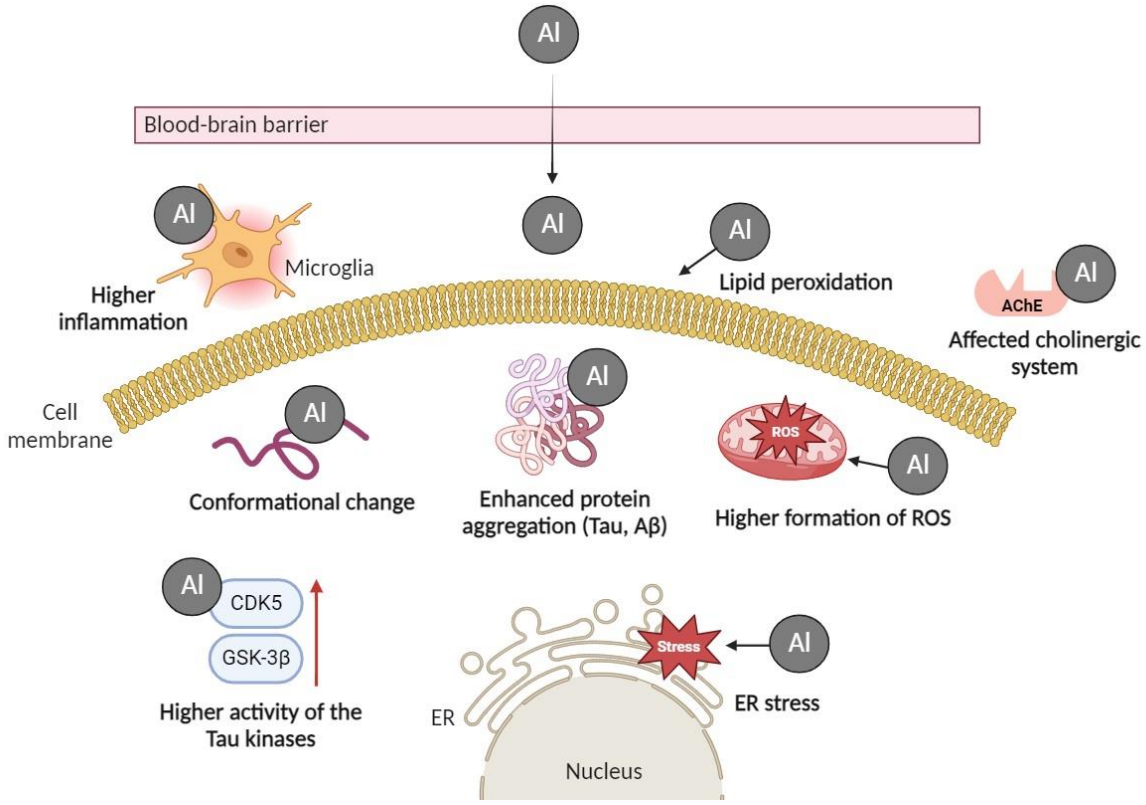


Figure 6. Effects of aluminium on the central nervous system. Created with BioRender.com.

1.4.2 AD model in neuroblastoma cell line

Live and adult human neurons for functional studies are not always promptly available. An alternative is using immortal cell lines, such as the neuroblastoma cell line SH-SY5Y. The expression of Aβ, Tau, synaptic factors, and other neuron specific hallmarks in SH-SY5Y cells makes them a suitable model to study the mechanism of neuron phenotype degeneration, including AD[52]. However, this cell line lacks some important features for the study of AD, such as the expression of neuron-specific proteins at levels comparable to mature neurons, including the expression of mature isoforms of Tau[53]. On the other hand, the neuroblastoma cell lines can potentially mimic the hallmarks of AD, upon treatment with various agents, including Alu[54].

1.4.3 AD model in zebrafish embryos

Zebrafish (*Danio rerio*) is a small aquatic vertebrate and tropical freshwater teleost fish, with a native natural habitat in southeast Asia, typically streams and rivers, silt-bottomed well-vegetated pools, and rice paddies adjacent to streams[55]. Temperature is one of the most important environmental factors for this species, since it should range between 26–29 °C[56].

Zebrafish is a popular animal model, since it carries several advantages, including the economical maintenance, fewer space requirements for setting up zebrafish husbandries, small size, short reproductive cycle, and high fertility, allowing it to produce at least 200 eggs per clutch every 2–3 days. Additionally, these fish produce transparent embryos with a diameter of about 0.7 mm[57]. This optical clarity observed in the initial stages of embryogenesis is crucial for investigators to analyse detailed developmental processes involving drug discovery. Furthermore, zebrafish embryos develop outside of the uterus, so they can be easily accessed post-fertilization for various studies[58]. On top of that, there is a high level of genome structure shared between zebrafish and humans (≈70% of human genes have zebrafish orthologs, compared to 80% of human genes with mouse orthologs), facilitating the use of zebrafish for the understanding of human genetic diseases[57,58]. Another important feature of zebrafish, especially, for the study of AD, is that the neuroanatomic and neurochemical pathways of zebrafish brain exhibit a profound resemblance with the human brain[59].

1.5 Therapeutic natural compounds for AD

Natural compounds are an emerging approach for AD therapy, as an alternative medicine, due to their efficacy and reduced side effects. Diverse natural products are capable to decrease the symptoms and alleviate the development AD, having shown anti-inflammatory, antioxidant, anti-amyloidogenic, and anti-cholinesterase properties[60–62]. Several natural agents such as eugenol, vitamin C, huperzine A, melatonin, quercetin, resveratrol, and rosmarinic acid have shown helpful results in protecting the brain in the process of neurodegeneration during aging and AD[63]. Petrosamine and curcumin are the natural compounds studied in this thesis.

1.5.1 Petrosamine

Petrosamine is a pyridoacridine alkaloid of intense colour that was initially isolated from a Thai marine sponge, *Petrosia* sp., that can be collected in the intertidal zone of Phuket Island, Thailand[64,65]. Since the discovery of the first pyridoacridine alkaloid (amphimedine), approximately 60 related alkaloids have been reported, and some have generated interest for their biological activities. These compounds have antifungal activity, anti-HIV activity, cytotoxic activity, and promote topoisomerase II inhibition through intercalation into DNA[65].

Numerous marine natural products, such as petrosamine, have been reported to exert AChE inhibition, which can become a possible avenue for the treatment of neurodegenerative diseases, where the AChE activity is affected, such is the case of AD[64]. Petrosamine is a potent AChE inhibitor, having an AChE inhibitory activity about six times the potency of the galanthamine, a current AChE inhibitor used in the treatment of AD[65].

1.5.2 Curcumin

Curcumin, commonly known as turmeric, a bright yellow plant pigment, isolated from the root of *Curcuma longa* L., is a popular spice widely used in South Asian and Middle Eastern countries. It exhibits many interesting photophysical and photochemical properties, and has been shown, by modern medicine to have an extensive range of biological activities, including antioxidant, anti-inflammatory, anti-carcinogenic, hepatoprotective, and neuroprotective activities[66].

Curcumin can be a favourable tool in the diagnosis of AD, since it effectively binds to Aβ plaques and emits a strong fluorescence signal, making it a powerful diagnostic reagent[67]. Moreover, curcumin has shown properties considered to be useful in inhibiting the hallmarks of this neurodegenerative disease, becoming a promising therapy. This natural product has anti-amyloidogenic ability, preventing deposition and accumulation of Aβ and promoting Aβ clearance, by attenuating APP maturation and supressing β-secretase[60,67]. Additionally, studies confirmed that curcumin has potential in decreasing hyperphosphorylated Tau aggregation[66]. Curcumin has excellent antioxidant properties, due to its free radical scavenging properties[66,68]. In addition, curcumin lowers oxidative stress-induced neuronal damage, by inhibiting lipid peroxidation. These diverse and attractive biological properties of curcumin may ameliorate the pathological features of AD. However, curcumin exhibits low bioavailability in the brain, so its use is limited[68].

1.6 RNA-based therapeutics

Currently, most therapeutic compounds used in a clinic setting are limited to proteins or small molecules. Small molecule- and protein-based therapies are effective and have been successful in many cases, although there are still numerous diseases that are untreatable with this strategy. Additionally, these proteins present other disadvantages, as most proteins are too large to enter their target cells and, therefore, are only effective when their target molecule is extracellular or excreted[69], while some still lack proteolytic stability and sufficiently long circulation times[70]. There is a demand for a therapy capable to target diseases that cannot be treated with other conventional drug groups. In this sense, RNA-based therapeutics have become a hot topic in science, and comprise a rapidly expanding category of drugs that will change the standard of care for many diseases, allowing for personalized medicine[71] and to control the expression of transiently altered genes, providing potential insight into developing treatments for various diseases[72].

RNA-based drugs comprehend several advantages, including: (1) ability to act on targets that are otherwise out of reach for a small molecule or a protein; (2) fast production and cost effective development; (3) long-term effect, when various modifications are applied to their synthesis or when these RNAs are encapsulated within carriers such as liposomes; and (4) no risk of genotoxicity compared to DNA-based therapies, where there is a possibility that they may integrate into the genome and cause a mutation[71,73].

1.6.1 Types of RNA therapeutics

The strategies for RNA therapeutics may involve the use of coding or non-coding RNAs. There are several types of therapeutic RNAs, such as RNAs that inhibit RNA activity, including: antisense oligonucleotide (ASO), small interfering RNA (siRNA), and microRNA (miRNA). Also, RNA that target proteins, such as RNA aptamer, and messenger RNA (mRNA) that encode potentially therapeutic proteins[72] (**figure 7**).

ASO has a length of 18–30 base pairs and is a single-stranded RNA/DNA molecule designed to specifically inhibit mRNA function. They bind to a specific complementary mRNA, triggering its inactivation to prevent it to be translated[72,74].

RNAs involved in the RNA interference (siRNA and miRNA) use a similar mechanism to ASO. RNA interference is an endogenous cellular process inducing certain RNAs to trigger degradation of RNA targets, providing an intrinsic defensive mechanism against invading viruses and transposable elements[75]. RNA interference involves the use of siRNAs to control gene function. siRNAs are small non-coding RNA with ≈20-24 nucleotide, fully complementary to the coding region of the target mRNA, allowing to knock down specific target genes. Because of this ability of siRNA, researchers can use such simple gene silencing tools to investigate gene function and advance disease therapy[73,75]. miRNAs are endogenous single-stranded small non-coding RNAs influencing gene expression, also via the RNA interference machinery. miRNAs regulate the expression of multiple mRNAs by blocking their translation or promoting degradation of the target mRNAs[71].

Aptamers are single-stranded oligonucleotides with well-defined three-dimensional structures that specifically bind and inhibit proteins. The ability of aptamers to form shapes offers high affinity as well as excellent specificity toward the target proteins. They are also known as chemical antibodies due to their synthetic origins and similar modes of actions to those of antibodies[72,75].

Finally, mRNAs are typically around 2 kb in length and serve as the intermediates between the coding genomic DNA and the encoded proteins, delivering genetic information to the translational machinery to generate the encoded proteins[73]. mRNA-based therapies can be divided into two subcategories based on their purpose: mRNA vaccines and protein replacement therapies, when diseases are caused by a lack of expression of a particular protein. In the first category, the mRNA transcript is designed to act as a vaccine against infectious diseases or cancer antigens. In the second category, exogenous mRNAs are introduced into cells to replace or supplement endogenous proteins[71].

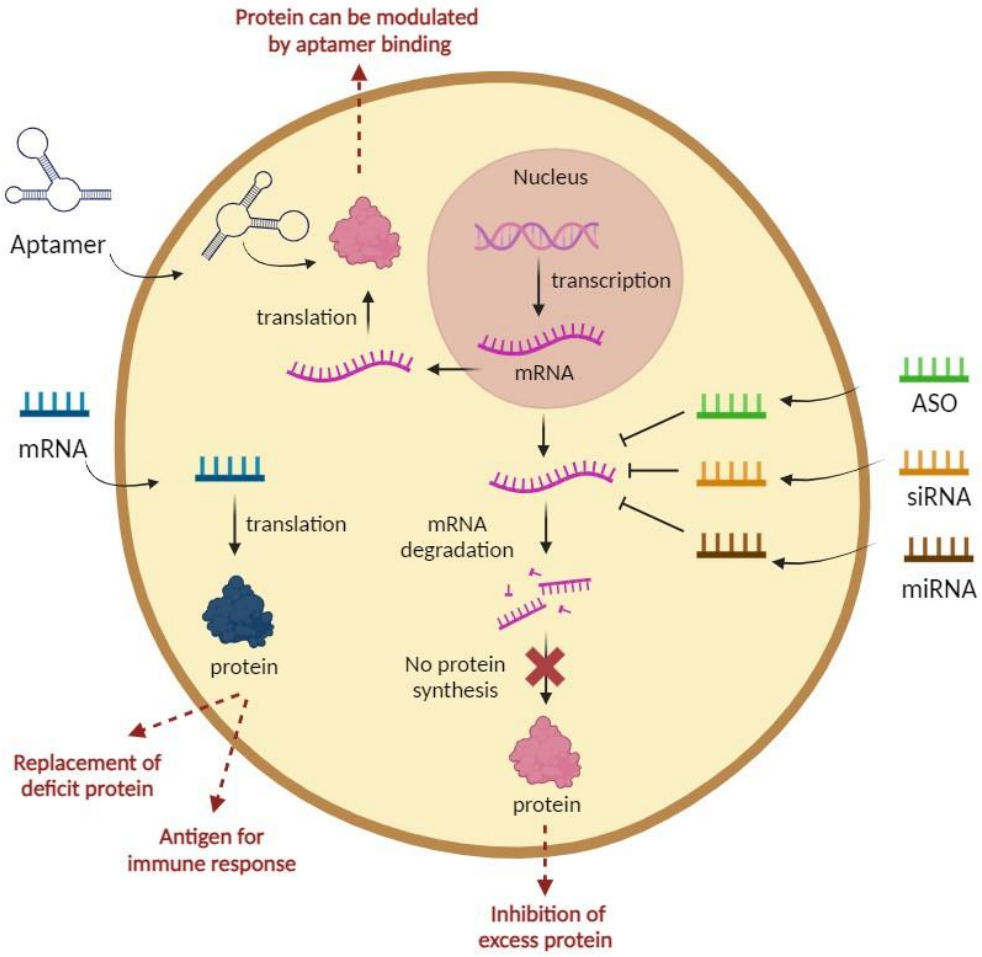


Figure 7. Mechanism of action of the RNA-based therapies. Diverse cellular molecules can be targeted by RNA therapy. Created with BioRender.com.

1.6.2 RNA-based therapeutics for AD: siRNA and mRNA

Silencing certain genes using suitable siRNA delivery systems can result in a significant breakthrough in AD therapy. Researchers silenced AD genes, such as APP, Tau, PS1, and BACE1, and verified that this silencing resulted in the reduction of mRNA levels of the targeted genes, indicating successful application of siRNA technology to the AD pathological process[76].

On the other hand, the brain has mechanisms to clear toxic proteins, including protein degradation pathways, that can be enhanced through mRNA expression for AD treatment. Accumulation of toxic proteins, inclusively of Aβ, triggers an inflammatory response by the immune cells of the brain (microglia and astrocytes) inducing phagocytosis and proteolytic degradation of plaques.

There are receptors on microglia (e.g. triggering receptor and toll-like receptors) that can recognize Aβ and trigger a phagocytic pathway. Also, there are two Aβ degrading enzymes (e.g. neprilysin and insulin degrading enzyme), which activity is reduced in AD, that can be released to remove Aβ extracellularly. The microglia receptors that recognize Aβ and the Aβ degrading enzymes are two ways to apply mRNA therapy in AD treatment[49]. However, in spite of the fact that the mRNA application in AD is a promising strategy, there is still a lack of studies regarding this subject. **Table 1** shows the available strategies for siRNA and mRNA therapy for AD, at the moment.

Table 1. Available siRNA and mRNA therapeutical strategies for AD.

	Role in AD	Reference
Targeted gene silencing by siRNA		
BACE1	Aβ derives from the APP through sequential cleavage by BACE1 and γ-secretase. Inhibition of BACE1 expression by siRNA therapy reduces the levels of Aβ.	[77]
APP	APP fragmentation leads to amyloid peptides. The APP expression can be reduced using siRNA.	[78]
VDAC1	VDAC1 is a voltage-dependent anion channel 1 found in the mitochondrial outer membrane, central in mitochondria-mediated apoptosis and overexpressed in post-mortem brains of AD patients. RNA-silenced VDAC1 genes cells showed effective results.	[76,79]
MAPT	Suppression of Tau expression has been shown to improve the disease. Experimentally this had been achieved by siRNA acting against in the human tau gene (MAPT).	[80]
PS1	y-Secretase cleavage is performed by a high molecular weight protein complex containing presenilin. Knock out of PS-1 dramatically reduced y-secretase cleavage of APP.	[81]
Proteins expressed by mRNA		
Neprilysin	Neprilysin plays a major role in the clearance of Aβ in the brain. mRNA effectively increased neprilysin in the brain, resulting in the significant decrease of Aβ concentration, showing the therapeutic potential of mRNA-based gene therapy for treating brain diseases.	[82]

1.7 Nanotechnology: Application of Delivery systems

One of the major challenges of RNA therapy is related to its delivery. RNA is a hydrophilic and negatively charged molecule, incapable of overcoming the extracellular and intracellular barriers, and gain entry in the cytoplasm to promote a successful delivery. Besides being unable to passively diffuse across the lipid bilayers, RNA is also susceptible to degradation by nucleases, and needs to effectively escape the endosome, upon cellular uptake[71,75]. Additionally, achieving a targeted delivery and high tissue accumulation are major hurdles for effective RNA therapeutics[73].

Nanotechnology represents an opportunity to overcome these challenges. Innovative nanoscale delivery systems transformed a former poorly performing RNA technology, with significant drawbacks, into a novel, must-have, therapeutic tool that is able to safely deliver RNA to the target, where it may exert its therapeutic effect more effectively[83] (**figure 8**).

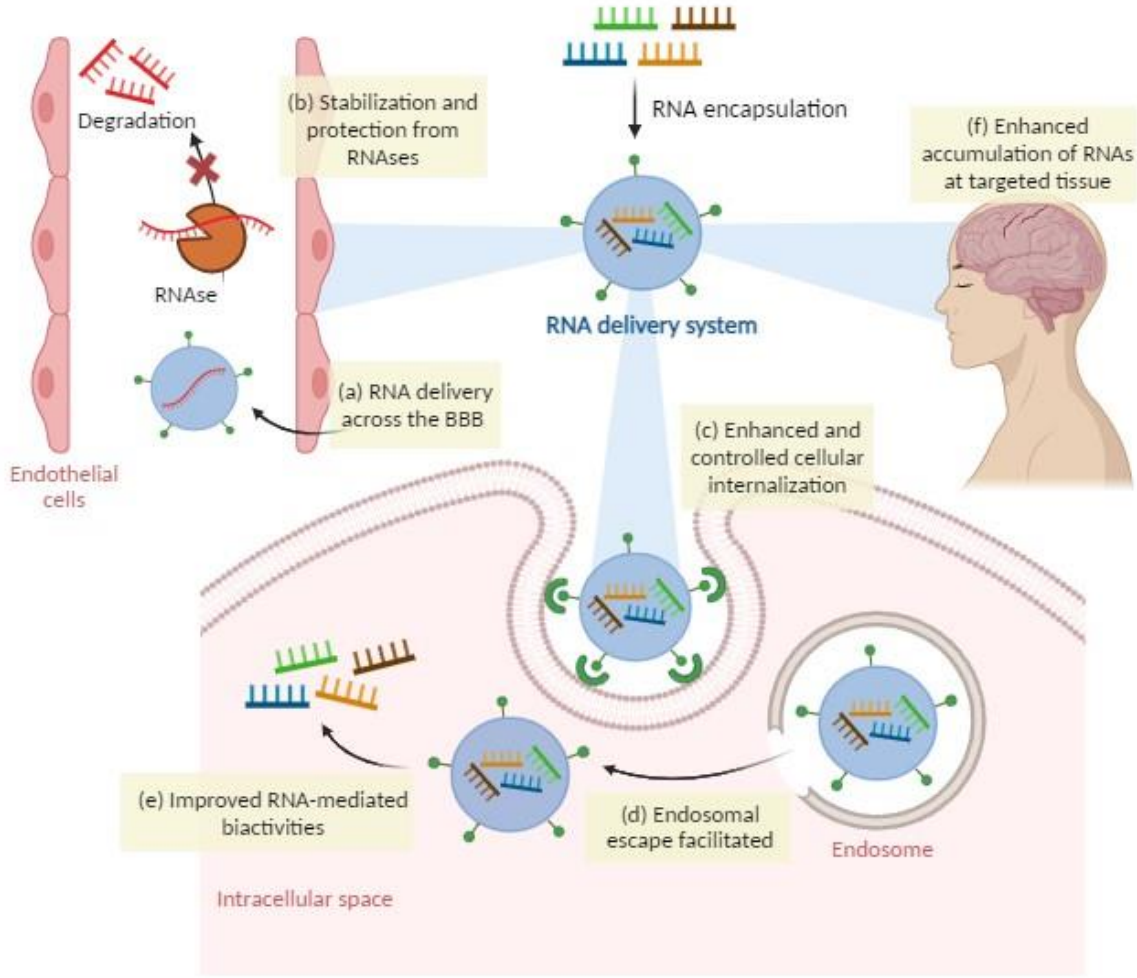


Figure 8. How delivery systems overcome the limitations of free RNA. Created with BioRender.com.

1.7.1 Promising delivery systems for brain delivery

One of the key challenges of the treatment of AD is the BBB. However, the development of nanotechnology-based approaches for brain delivery, such as liposomes, gold nanoparticles, dendrimers, polymeric nanoparticles, micelles, and carbon quantum dots, can be the solution for improved brain-targeting therapies[84] The most promising delivery systems to promote BBB transposition are indicated in **Table 2**.

Table 2. Promising delivery system to target the CNS.

Delivery system	Characteristics	Reference
Liposomes	Liposomes are constituted by a lipidic content, organized in a bilayer structure due to their amphipathic properties. Liposomes have plenty of advantages, including small size, ease to manufacture and of their production methods, scalability, capability of encapsulating either hydrophobic or hydrophilic drugs, and possibility of surface modifications for targeted, prolonged, sustained release and improved stability in the blood.	[85–87]
Gold Nanoparticles	Gold nanoparticles are biocompatible, nontoxic, with ultra-small size (1-100 nm), high surface area, and ability to be easily functionalized with biomolecules. For example, the effect of insulin-coated gold nanoparticle with 20 nm, showed widespread biodistribution and accumulation within the brain.	[84,88,89]
Dendrimers	Dendrimers are synthetic hyper-branched 3D macromolecules. The globular structure of dendrimers comprises a core, layers of branched repeat units emerging from the core, and functional end groups on the outside layer. This type of delivery system can transport diverse therapeutic agents across the BBB.	[84,90]
Polymeric Nanoparticles	Polymeric nanoparticles can be composed by a variety of compounds , such as proteins, lipid-polymer hybrids, and single polymers, influencing its properties. *In vitro* studies showed that the use of polymeric nanoparticles enhanced drug delivery to the brain. An example of polymeric nanoparticles for AD treatment is that of the poly(lactide-co-glycolic) acid nanoparticles.	[84,91]

Table 2: *Cont.*

Micelles	Micelles are amphiphilic molecules, since they have a polar region, facing the outside surface and the non-polar region that forms the core. Micelles have appealing characteristics for brain delivery, since they have a small size (5–50 nm), provide sustained and controlled release, provide stability for the encapsulated drugs, and improve the bioavailability of poorly water-soluble drugs.	[84]
Carbon quantum dots	Carbon dots are a promising nanoparticle for brain delivery, thanks to their properties, that include ultra-small size (below 10 nm), low toxicity, high drug-loading capacity, long-term stability, controlled drug release capabilities and, increased ability to cross the BBB.	[92]

1.7.2 Exosomes

Extracellular vesicles are lipid vesicles secreted by cells into the extracellular space[93]. These extracellular vesicles are classified into three groups based on their size, content, function, biogenesis, and release pathway: microvesicles, apoptotic bodies, and exosomes[93,94]. Microvesicles are produced by budding and blebbing from the plasma membrane and apoptotic bodies are released by cells undergoing programmed cell death[94].

Exosomes are a natural subpopulation of extravascular vesicles with a diameter of 30–150 nm, secreted by all cell types and have been found in plasma, urine, semen, saliva, bronchial fluid, cerebral spinal fluid, breast milk, serum, amniotic fluid, tears, lymph, bile, and gastric acid[93]. Exosomal vesicles form by inward budding of the limiting membrane of early endosomes, which mature into multivesicular bodies (MVB) during the process. MVB are eventually either sent to the lysosome to be degraded along with all of its components or fused with the cell's plasma membrane to release its content, including exosomes, into the extracellular space[93,95] (**figure 9**). Originally, exosomes were thought to be only mechanism of cellular dumping. However, it has been found that their main function is intercellular communication, being released into the extracellular environment where they are captured and internalised by neighbouring cells. This unique mode of communication between cells and tissues within the body, make it possible for the exosomes to potentially travel through the systemic circulation to access neighbouring tissues and being capable of reach very distant organism tissues[96].

Additionally, the information is transferred by exosomal cargo, composed by a wide variety of macromolecules such as nucleic acids, proteins, and lipids[95]. They have various other functions, for example, exosomes in the CNS have been found to contain pathogenic proteins, such as Aβ and Tau, that may aid in AD progression[93,95].

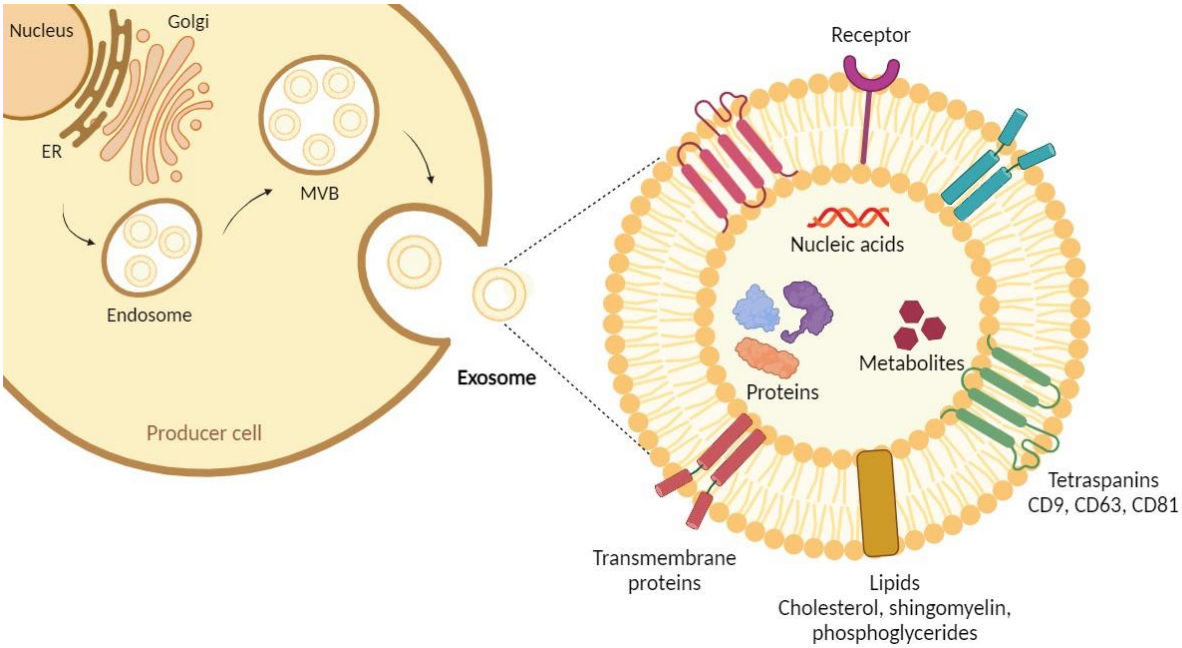


Figure 9: Scheme of the natural exosome's formation and their composition. Created with BioRender.com.

Natural exosomes are being explored as delivery systems for biomedical purposes, owing to their unique properties. These systems possess small size, high biocompatibility, and low toxicity, as well as their improved efficacy in crossing the blood-brain barrier, which is a key feature for drug delivery in AD[97]. However, their clinical application is limited by certain critical parameters, including the need for more robust and reproducible manufacturing processes, such as massive production and isolation methods, and lack of characterization. Other crucial drawbacks are that drug loading and/or retention of drugs in exosomes is limited , and their half-life in circulation and storage stability are short[97,98].

1.7.3 Exosome-like liposomes

Given the enumerated shortcomings of natural exosomes, other alternatives have been explored, taking inspiration by the composition of these vesicles. Exosome-like liposomes are liposomes that mimic the lipidic composition of natural exosomes, making them biocompatible. Exosomes are mainly composed by cholesterol, ceramide, sphingomyelin and phospholipids[93], and exosome-like liposomes were produced with a similar composition. Additionally, the exosome-like liposomes also share a similar composition to the recent developed lipid nanoparticles vaccines against COVID-19, which once again proves how promising this novel delivery system can be[99]. This new type of delivery system is mainly composed by four lipids: (1) cholesterol, (2) helper phospholipid, (3) pH-sensitive lipid, and (4) PEG-lipid. The cholesterol main functions are increasing the flexibility of the exosome-like liposome and potentiating biocompatibility. The helper phospholipid contributes for the stability and helps in the endosomal escape. The pH-sensitive phospholipid is constituted by an ionizable amine group, that confers a positive charge in an acidic environment, such as the endosome (pH 5.5), making it possible to fuse with the endosomal membrane and deliver the drug in the cytosol. The polyethylene glycol (PEG)-lipid is crucial to increase biocompatibility and biodistribution, improve surface properties, and maximize *ex vivo* stability[99,100]. Also, PEG plays a crucial role in the escape of the immune system, as it forms a protective layer on the surface of the liposomes, protecting the carrier from the binding of plasma proteins[101].

The exosome-like liposomes can be considered a hybrid delivery system combining advantageous features of exosomes and liposomes. When comparing the advantages and disadvantages of natural exosomes and liposomes, it is clear that these two systems can complement each other into one delivery system with several benefits, such as the manufacturing methods and easy production of liposomes and non-toxic/biocompatible and small size of exosomes[98,102].

To apply this system for delivery of therapeutic agents in AD, it is fundamental that the exosome-like liposomes possess the capacity to cross the BBB and deliver the drug in the brain. The gap between the tight junctions only allows passive diffusion of lipidic compounds with a molecular weight lower than 400-600 Da[39]. Exosome-like liposomes , being formulated with a lipidic composition that mimics natural exosomes, and have adequate physicochemical features that making them a promising system to cross the BBB and deliver the targeted therapy.

Chapter 2

Objective

2. Objective

A robust preclinical disease model is a necessary requirement to understand the underlying mechanisms and signalling pathways of AD, and to further execute drug screening to find a novel therapy. As such, one of the objectives of this theses was to establish tow AD models, by treatment with the known neurotoxin $AlCl_3$: one *in vitro* model using the neuroblastoma cell line SH-SY5Y, and one *in vivo* model using zebrafish embryos, which have a similar CNS to the human one.

RNA therapy is a rapidly growing field of therapies to fulfil the current gap in effective drugs for AD treatment. However, to effectively deliver this therapy, a safe and efficient delivery system, with the capacity to cross the BBB, is needed. For this reason, another principal objective of this thesis was to develop exosome-like liposomes for the encapsulation of RNA-based therapies. Namely, the specific objective was to produce, characterize and study the cellular uptake of the exosome-like liposomes loaded with siRNA and mRNA. Moreover, we intended to evaluate the ability of anti-Tau siRNA loaded exosome-like liposomes, to counteract the toxicity of $AlCl_3$ in the established AD models.

Finally, another aim of this thesis was to test the ability of other therapeutic compounds, such as petrosamine (that can be encapsulated or not), to counteract the toxicity of $AlCl_3$ in the two implemented models.

Chapter 3

Materials and Methods

3. Materials and Methods

3.1 Materials

Aluminium chloride was obtained from Centre of Molecular and Environmental Biology. Fetal bovine serum (FBS) and Penicillin/Streptomycin were purchased from Biochrom GmbH (Berlin, Germany). Dulbecco's Modified Eagle's Medium (DMEM) was acquired from Sigma-Aldrich (St. Louis, MI). Cholesterol, sphingomyelin, Dipalmitoylphosphatidylcholine (DPPC), 1,2-dioleoyl-3-dimethylammonium-propane (DODAP) and N-palmitoyl-sphingosine-1-{succinyl[methoxy(polyethylene glycol)2000]} (PEG ceramide) were purchased from Avanti Polar Lipids (Alabaster, AL). The RiboGreen kit was acquired from Invitrogen (Eugene, OR). Petrosamine isolated from a Thai sponge species (*Petrosia* n sp.) was obtained from Ceara State University of the QPNSZ Group, Brazil. siRNA anti-Tau with the sense sequence: 5′CAUCCAUCAUAAACCAGGATT3′ was purchased from Nzytech (Lisbon, Portugal). FireFly Luciferase mRNA that expresses luciferase protein was purchased from TriLink Biotechnologies (United States, California).

3.2 Cell culture

3.2.1 HEK293 cell line

HEK293 is an epithelial-like cell isolated from a patient's kidney and a highly transfectable cell line[103]. The cells were cultured in Dulbecco's modified Eagle's medium (DMEM), with phenol red supplemented with 10% fetal bovine serum (FBS) and, 1% penicillin/streptomycin mixture, in a humidified incubator with a 5% CO_2 atmosphere and at 37° C. When the cells reached 80% confluence they were treated with 0.05% trypsin. The cells were subcultured at a ratio of 1:5, every 4 days, in 25 cm^2 flasks.

3.2.2 SH-SY5Y cell line

The human neuroblastoma cell line SH-SY5Y were routinely grown in DMEM, with phenol red, supplemented with 15% of FBS, 1% (v/v) L-glutamine and 1% (v/v) penicillin/streptomycin in a humidified incubator with a 5% CO_2 atmosphere and at 37° C. The cells were allowed to proliferate until they reached 80% confluence and then treated with 0.25 % trypsin, in order to maintain the cell's properties. The cells were subcultured in 25 cm^2 flasks once a week with a dilution of 1:3 (v/v).

3.3 AD Model in neuroblastoma cell line SH-SY5Y

The key to understanding the etiology of AD lies in the development of effective disease models, which can ideally reproduce all characteristics of the disease. To study and acquire knowledge on the changes occurring in the AD brain, and consequently, to study promising therapies for the treatment of this disease, the most common experimental tools used are *in vitro* 2D models.

In the current study, three concentrations of $AlCl_3$ (50 µM, 200 µM, and 1000 µM)[104] were used to try to induce a similar phenotype of AD in the neuroblastoma cell line SH-SY5Y. To observe the changes caused by $AlCl_3$ several assays were performed.

3.3.1 Cell viability - Resazurin assay

The resazurin assay offers a simple, rapid, and sensitive measurement of the cell's viability. Living cells are metabolically active and able to reduce the non-fluorescent dye resazurin (Sigma-Aldrich) to the strongly fluorescent dye resorufin, with the fluorescence output being proportional to the number of viable cells[105]. The cells were seeded in 24-well plates at a density of 1 x 10^5 cells per well. After stabilization, SH-SY5Y cells were treated with $AlCl_3$ at different concentrations (50 µM, 200 µM and 1000 µM) for 24h. After the incubation, a death control was included in the assay, by adding 30 % DMSO in specific wells, and further incubating the cells for 30 mins. Then, the medium was removed and 300 µl of resazurin (c = 100 µg/mL) were added to each well and the cells were incubated for 2 h at 37° C. The fluorescence was measured at λ_{exc}=530 nm and λ_{em}=590 nm in a microplate reader (Tecan, Infinite MPlex).

3.3.2 Cell viability – SRB assay

Sulphorhodamine B (SRB) assay is used for cell density determination, based on the measurement of cellular protein content, since SRB dye binds to basic amino acid residues on proteins[106]. The cells were plated in 24-well plates at a density of 1 x 10^5 cells per well. After overnight seeding, SH-SY5Y cells were treated with $AlCl_3$ at different concentrations (50 µM, 200 µM and 1000 µM) and incubated for 24h. The medium was then removed, the cells were washed with PBS 1X (pH=7.4) and 400 µl of the fixation solution (1% of acetic acid in methanol) were added. The plate was placed at -20° C for 1h and 30 mins and left to dry at room temperature. Then, 250 µl of SRB (Sigma-Aldrich) were added to each well and left to incubate in the dark for 1h30 at 37° C.

The SRB was removed, and the cells were washed with 1% of acetic acid. Then, Tris Buffer (10 mM, pH=7.4) was added to each well and the absorbance was read at 510 nm in a microplate reader (Tecan, Infinite MPlex).

3.3.3 Acridine Orange (AO)/ Propidium Iodide (PI) assay

Acridine orange (AO) and Propidium iodide (PI) are applied for the simultaneous visualization of both viable and nonviable cells. AO is a membrane-permeable, cationic dye that emits a green fluorescence when bound to nucleic acids of viable cells. PI is impermeable to intact membranes but readily penetrates the membranes of nonviable cells and emits red fluorescence when bound to DNA or RNA[107].

The cells were incubated at a cellular density of 1 x 10^5 cells per well in a 24-well microplate. After overnight seeding, the cells were incubated with three different concentrations of $AlCl_3$ (50 µM, 200 µM and 1000 µM) for 24 h at 37° C. After the 24h incubation, a death control was included by adding 30 % of DMSO and incubating at 37°C in the dark for 45 mins. Then, 500 µl of PI (c=50 µM)[102] were added to each well and the plate was left in the dark at 37° C for 15 min. Subsequently, another 500 µl of AO (c=50 µM)[102] were added and the plate was again incubated in the dark at 37° C for 15 min. The final solution of each well was removed, and the fluorescence was then visualized using FITC and TRITC filters in an inverted fluorescence microscope Olympus IX71. Additionally, the percentage of viable cells, early apoptotic cells, and apoptotic cells in each condition was calculated using ImageJ software, according to the number of cells stained with red, yellow, and green.

3.3.4 Determination of the Reactive Oxygen Species by the DCFDA assay

The cells were incubated at a cellular density of 1 x 10^5 cells per well, in a 24-well microplate. After overnight seeding, the cells were incubated with three different concentrations of $AlCl_3$ (50 µM, 200 µM and 1000 µM) at 37° C, for 24 h. The medium was removed, 200 µl of DCF-DA (Sigma-Aldrich) (c=100 µM) were added, and the plate was incubated at 37°C, for 30 mins. The DCF was removed and 300 µl of t-BHP (c=1 mM) were added only to the oxidant control, and the plate was incubated at 37° C, for 15 mins. The cells were lised with 350 µl of DMSO:PBS 9:1 (v:v) and the fluorescence was measured at λ_{exc}=485 nm and λ_{em}=538 nm in a microplate reader (Tecan, Infinite MPlex).

3.3.5 Determination of Lipid Peroxidation

The cells were incubated at a cellular density of 2 x 10^4 cells/well in a 96-well microplate. After overnight stabilization, the cells were incubated with three different concentrations of $AlCl_3$ (50 µM, 200 µM and 1000 µM) for 24 h. The cells were lised with Lysis Buffer (10 mM Tris, 1 mM EDTA, 0.2% Triton 100X, pH=8). Each sample was collected to eppendorfs, and 1.5 ml of sodium phosphate buffer (pH = 7.4) were added, before incubating for 1 h, at 37°C. Then, a volume 1:1 (v/v) of trichloroacetic acid (5 %) and a 0.67% solution of Thiobarbituric acid (TBARS) (Sigma-Aldrich) were added to each sample, in 2:1 (v/v) proportion, and the samples were centrifuged at 2300 *g* for 15 mins. The supernatant was collected and heated at 100° C for 15 mins, and finally the absorbance was read at 532 nm in a microplate reader (Tecan, Infinite MPlex).

3.3.6 Determination of AChE activity

Ellman's reaction is the most frequently used technique to assess AChE activity, for biochemical analysis, due to its sensitivity and simplicity. The AChE enzyme hydrolyses acetylthiocholine into acetate and thiocholine. Thiocoline reacts with Ellman's reagent 5-5'-dithiobis(2-nitrobenzoic acid) (Sigma-Aldrich) (DTNB) to form a mixed disulfide and the yellow chromophore 5-thio-2-nitrobenzoic acid (TNB). TNB production may then be followed photometrically at 412 nm[108] (**figure 10**).

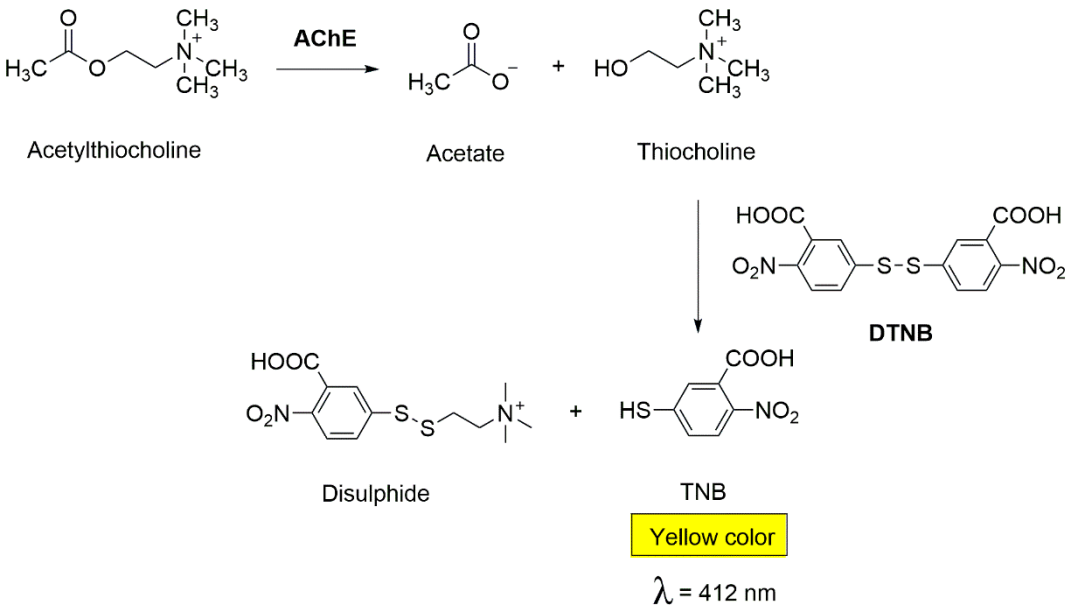


Figure 10. Ellman's reaction to detect AChE activity. Created with ChemDraw.

The cells were incubated at a cellular density of 2 x 10^4 cells/well in a 96-well microplate. After overnight seeding, the cells were incubated with three different concentrations of $AlCl_3$: 50 µM, 200 µM and 1000 µM for 24 h.

For normalization purposes, the total protein of the samples was quantified by the Bradford assay against a standard protein curve (**figure 11**) obtained using four different concentrations of Bovine Serum Albumine (BSA). The Bradford reagent was added to the 96-well plate. The plate was incubated at room temperature in dark, for 15 mins and the absorbance was then measured at 600 nm in a microplate reader (IndiaMART, Bio-Rad).

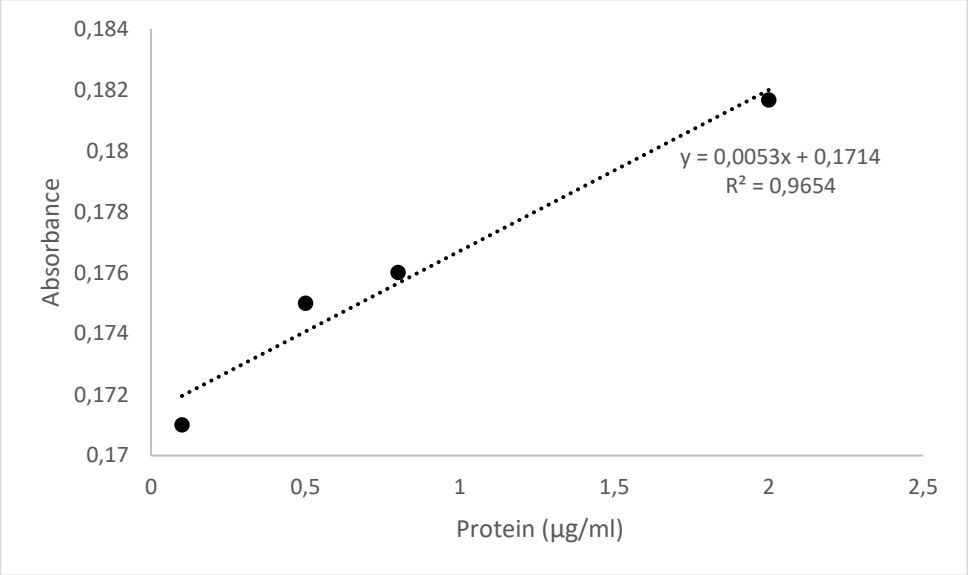


Figure 11. Standard protein curve of BSA solutions at different concentrations.

For the measurement of the AChE activity, a 1:1 (v/v) mixture of acetylthiocholine iodide (1mM) and DTNB (0,5 mM)[109] was prepared. The cell culture medium was removed by inverting the microplates and blotting them on a paper towel to take out as much of the medium as possible. Then, 100 µL of the reaction mixture was added to each well using a multichannel pipette. AChE activity was measured spectrophotometrically, according to Ellman's reaction, every minute for 60 mins at 412 nm in a microplate reader (IndiaMART, Bio-Rad). The AChE activity was obtained according to **Equation 1**.

$$AChE\ activity = \frac{\left(\Delta Abs_{sample} - \Delta Abs_{blank}\right) x\ Vt/Vs}{Prot\ x\ \varepsilon\ x\ d}$$

Equation 1. Equation for the determination of AChE activity. ΔAbs_{sample} is the variation of the absorbance of the samples per minute; ΔAbs_{blank} is the variation of the absorbance of the blanks per minute; Vt/Vs (total volume/volume of sample) is the dilution factor of the samples in the wells; Prot is the protein concentration of the samples (mg/mL); ε is the molar extinction coefficient of TNB (13,600 M^{-1} cm^{-1}) at 412 nm; and *d* is the light path length.

3.4 AD Model in zebrafish embryos

Another objective of this thesis was to establish a zebrafish embryo model of AD, to create a model that best reproduces the AD pathology *in vivo*, and also, to conduct drug screening. To do so, two concentrations of $AlCl_3$ (50 µM and 200 µM)[104] were tested and the phenotypic changes were evaluated. The evaluation of the phenotypic parameters of zebrafish embryos exposed to aluminium chloride is an important step, since it gives a great amount of information that allows to perceive changes that affect the development of this animal. Additionally, a few biochemical assays were performed to validate this model.

3.4.1 Zebrafish Embryo Maintenance

Breeder adult zebrafish (*Danio rerio*) were housed in a properly oxygenated tank, at a temperature of 26°C with a natural photoperiod of 12h:12h light/dark. The water quality parameters were checked regularly, and the fish were fed twice a day with a commercial diet (Tetra-Min).

3.4.2 Embryo treatment for Fish Embryo Test (FET)

The embryos were obtained from 7 healthy adult zebrafish (4 females and 3 males) at a temperature of 28°C. The embryos laid at the first light in the morning were collected in clean aquarium water (UV treated water) and selected with a stereomicroscope to eliminate unfertilized or unviable eggs.

According to the procedure of Fish Embryo Test (FET), newly fertilized zebrafish embryos are exposed to a chemical to test and every 24 hours-post fertilization (hpf) phenotypic parameters are observed[110]. Embryo treatments were performed in non-treated 24-well plates with 10 embryos per well.

Then, 2 ml of test solutions were added to each well, which were renewed every day of the treatment, and the plates were incubated at 26°C.

An $AlCl_3$ stock solution was diluted in aquarium water and then embryos were exposed to 50 and 200 µM of $AlCl_3$ during the first 72 hpf[104]. At this time point, the $AlCl_3$ solutions were substituted by aquarium water until 120 hpf. During the experiment, 20 embryos were used for control, being exposed only to aquarium water, also renewed every day. Dead embryos were removed from the wells to avoid intoxication of the living embryos due to the decomposition of dead ones. All of the test conditions were conducted applied up to 120 hpf to evaluate phenotypic parameters. At the end of the experiment, the larvae with 120 hpf were euthanized in cold and stored at -20°C in RNA Later (Invitrogen), until further analysis.

3.4.3 Phenotypic Parameters evaluation

Embryo development was monitored under Leica IL LED inverted microscope coupled with an ICC50 HD camera (Leica Biosystems, Germany) at a magnification of 4X. The survival rate was determined by counting the number of dead embryos at each time point. The hatching rate was checked until 72 hpf and the epiboly was recorded at 6 hpf. The embryo development was documented at 24, 48, 72, 96, and 120 hpf, by imaging, to determine the yolk volume, pupil volume and by video recordings to analyse the cardiac frequency. The larvae length was only measured from the 72 hpf until 120 hpf (**figure 12**).

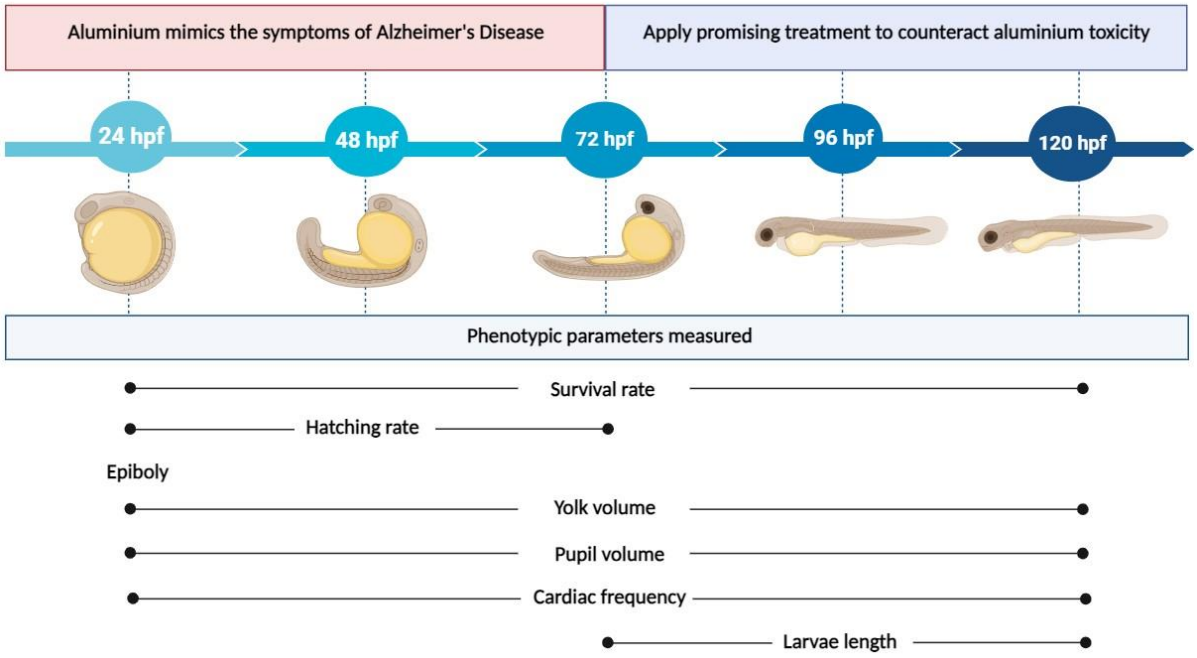


Figure 12. Different zebrafish embryo phenotypic parameters measured and corresponding timepoints they were observed. Created with Biorender.com.

3.4.4 Ethical statement

All the experiments were performed in accordance with the guidelines and policies dictated by European regulations on the wellness of animals employed for experimental purposes (Directive 2010/63/EU).

3.4.5 Analysis of Apoptosis

The analysis of apoptosis in zebrafish larvae exposed to 50 µM and 200 µM of $AlCl_3$ with 120 hpf was performed with AO staining protocol, according to Capriello *et al.*, 2021[111]. Briefly, untreated and treated zebrafish larvae were rinsed with PBS 1X and incubated in 2 ml of AO (c=5 µg/ml)[111]. Afterwards, 0.4% of Tricaine, a chemical anesthetic used in zebrafish research, was added to each well and left in the dark for 30 min[112]. Following the staining, the larvae were washed with PBS 1X (pH=7.4) to remove the excess dye. Stained larvae were examined under fluorescent microscope Olympus IX71, setting the FITC channel, that has its emission peak at 525 nm (green spectrum), to visualize the apoptotic cells like fluorescent spots. The intensity of the fluorescent spots for each condition was determined using ImageJ software.

3.4.6 Determination of lipid peroxidation

Lipid peroxidation was evaluated based on the formation of MDA in tissue homogenates by the TBARS method. The whole body of 10 embryos with 120 hpf were homogenized in 800 µl of potassium phosphate buffer solution (KPBS) (pH = 7.4) by sonication. Then, a volume of 1:1 (v/v) 5% trichloroacetic acid was added and the samples were incubated in ice for 15 min. To each sample 2:1 (v/v) of 0.67% thiobarbituric acid was added and centrifuged at 2200 x *g* for 10 min at 4°C[113]. The supernatant was incubated in a thermoblock at 100° C for 10 min and the absorbance was measured at 535 nm[114] in a microplate reader (Tecan, Infinite MPlex).

3.4.7 Determination of the AChE activity

Ellman's reaction was used for the determination of AChE activity of zebrafish embryos with 120 hpf, exposed to $AlCl_3$. The samples were kept on ice during the entirety of the procedure. First, the whole body of 10 embryos of each condition were homogenized in 800 µl of KPBS, by sonication during 10 s. The homogenates were centrifuged at 3000 x *g* for 10 min, at 4°C.

For normalization purposes, the total protein of the samples was quantified by the Bradford assay, another standard protein curve (**figure 13**) was obtained using five different concentrations of BSA, with higher concentrations from the one used in the AChE activity assay performed *in vitro* (section 3.3.6). The total protein was quantified adding Bradford reagent to the samples in a 96-well plate and incubated in the dark for 15 mins at room temperature. The absorbance was read at 600 nm in a microplate reader (IndiaMART, Bio-Rad).

To determine the AChE activity, according to Gravato *et al.,* 2021[115], an AChE reaction buffer, with DTNB (c=4 mM) and acetylthiocholine iodide (c=0.075 M) was prepared and added to the samples in a 96-well plate reader using a multichannel pipette. The absorbance was measured at 412 nm each 10 s during 3 mins in a microplate reader (IndiaMART, Bio-Rad). The AChE activity was obtained according to **Equation 1**.

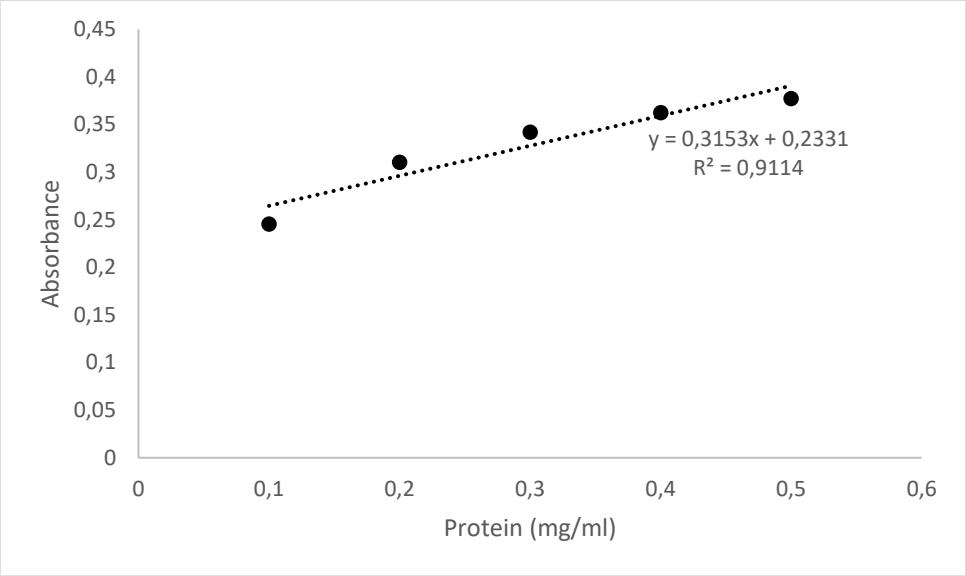


Figure 13. Standard protein curve of BSA solutions at different concentrations.

3.5 Exosome-like liposomes

This formulation of exosomes-like liposomes was prepared by the ethanolic injection method. This method involves the rapid injection of an ethanolic solution of lipids into an aqueous medium, which leads to rapid formation of vesicles without passing through any intermediate process[116]. Upon injection, the unfavourable exposure of the hydrophobic groups of the phospholipids to the aqueous phase, results in the arrangement of the lipids at the boundary phase between ethanol and water, in the form of bilayered phospholipid fragments. In this arrangement, the middle of the layer is composed of hydrophobic tails, with two molecules facing each other while the polar heads are directed outwards. Consequently, the phospholipid fragment generates an end-to-end fusion phospholipid bilayer to form a closed system, as an attempt to limit the exposure of the hydrophobic sides to water[117].

The lipids used in these systems are presented in **Table 3**.

Table 3. Lipid percentage (mol:mol) and concentration of the stock solution of the various lipids used in the preparation of the exosome-like liposomes.

Lipid	Lipid percentage in the formulation (%)	Concentration (mM)
Cholesterol	0.50	40
DPPC	0.30	30
Sphingomyelin	0.15	30
PEG-ceramide	0.05	20

These exosome-like liposomes were prepared, with DODAP for RNA delivery, encapsulating (1) luciferase encoding mRNA; (2) anti-Tau siRNA; and (3) standard siRNA and labelled with Oil Red O.

However, the production method, characterization and encapsulation efficiency of siRNA loaded exosome-like liposomes will not be mentioned in the following thesis, since these systems have already been described[118]. Additionally, exosome-like liposomes without DODAP with curcumin were produced. However, the production method and characterization will not be mentioned, since it was already described by Fernandes *et al.*[102].

3.5.1 Production of exosome-like liposomes for RNA delivery

In addition to the lipids described in **Table 3**, to incorporate nucleic acids into exosome-like liposomes, DODAP was included in the formulation. DODAP is an ionizable lipid, positively charged at low pH, used to promote efficient encapsulation of negatively charged molecules, such as nucleic acids, into the liposomes[119]. Hence, citrate buffer with an acidic pH (pH=3) was used to prepare these exosome-like liposomes.

For the preparation of these exosome-like liposomes encapsulating luciferase mRNA, a lipid film was made in a test tube by evaporating a mixture of 86.7 µl of DPPC and with 84.2 µl of DODAP (40 mM), dissolved in chloroform, in a rotatory evaporator. Subsequently, the lipid film is dissolved with 162.5 µl of cholesterol, 65 µl of sphingomyelin, and 32.5 µl of PEG-ceramide. Then, 60 µl of the pre-heated, at 60° C, solution was injected into 400 µl of pre-heated, at 60° C, citrate buffer with 40 µl of luciferase mRNA (c=0,5 µg/µl), under vortex. After the injection, both the lipid solution, and the forming liposome suspension were incubated in a water bath at 60° C, a temperature above the phase transition temperature of the lipid, and the procedure was repeated until the lipid solution was totally injected into the citrate buffer suspension. Empty exosome-like liposomes, without mRNA, were also produced.

The preparation of the exosome-like liposomes labelled with Oil Red O, and encapsulating standard siRNA, is similar to the protocol mentioned before, but, in this instance, including 318,7 µl of Oil Red O (c=5 mM) dissolved in an ethanol/chloroform 1:1 (v/v) mixture, in the lipid film formation along with the DPPC and DODAP.

All exosomes-like liposomes were stored at 4° C prior to analysis.

3.5.2 Exosome-like liposome's purification by molecular size exclusion chromatography

Exosome-like liposome purification was performed so that any free RNA does not interfere in the quantification of the encapsulated mRNA, and in the case of the exosome-like liposomes labelled with Oil Red O, this purification is performed to remove any free dye.

This process consisted in the passage of aliquots of 200 µl of the exosome-like liposomes with HEPES buffer through a house-prepared molecular exclusion column with Sepharose CL-4B and equilibrated in HEPES buffer (pH = 7.4), separating the exosome-like liposomes from the free mRNA and free Oil Red O.

3.5.3 Physical characterization of the exosome-like liposomes

Several key properties of these systems need to be efficiently and reliably measured, such as particle size, homogeneity and polydispersity, and surface charge. The average size and polydispersity index (PDI) were determined by dynamic light scattering (DLS), and the superficial charge was determined by electrophoretic light scattering (ELS).

3.5.3.1 Size and polydispersity determination by dynamic light scattering (DLS)

The principle behind the measurement of particle size by DLS is based in the fluctuations of elastic laser light scattering due to the particle's individual *Brownian motion* in a solvent. These can be utilized to determine particle size in real-time, as small particles move faster than large ones, making this random fluctuation of the scattering light also faster[120].

The PDI is a representation of the size distribution of the populations within a given sample. The numerical value of PDI ranges from 0.0 (for a perfectly uniform sample with respect to the particle size) to 1.0 (for a highly polydisperse sample with multiple particle size populations)[121] (**figure 14**). Colloidal particles with PDI bellow than 0.1 implies a monodisperse size distribution, whilst values greater than 0.1 may imply polydisperse particle size distributions[122]. However, in drug delivery applications using lipid-based nanoparticles, a PDI of 0.3 and below is considered to be acceptable and indicates a homogenous population of the phospholipid vesicles[121].

An aliquot of 10 µl of each exosome-like liposome sample was diluted in 990 µl of HEPES buffer (pH 7.4). This solution was placed in a polystyrene cuvette (Sarstedt, Nümbrecht - Germany) and the size and PDI were measured, using appropriate standard operation procedure (SOP) in a Zetasizer nano ZS (Malvern, Malvern - United Kingdom)

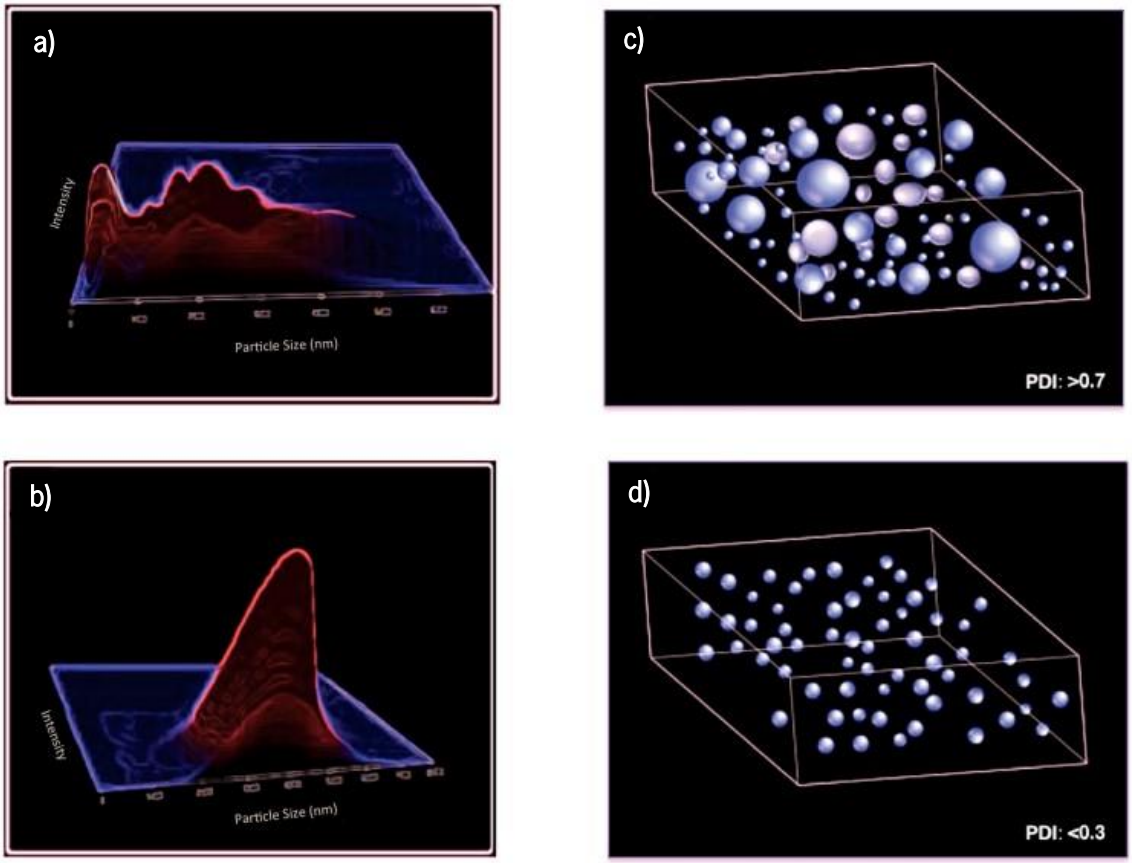


Figure 14. Representation of the polydispersity index. Schematic representation of typical particle size graphs indicating a (a) polydisperse sample and (b) a monodisperse sample. Representation of the particle size distribution of a sample containing a (c) polydisperse population of particles (with a high PDI value); and (d) a sample containing a monodisperse population of particles (with a low PDI value). Edited from [121].

3.5.3.2 Surface charge measurement by electrophoretic light scattering (ELS)

Electrophoretic light scattering is one of the main methods for the determination of the zeta (ζ) potential of particle dispersions, an indirect measurement of the superficial charge of the particle, based on the difference of potential between the Stern layer and the disused layer of the particles. The zeta potential is generally used to characterize the stability of the system because it is related to the particle surface charge. The principle of this technique is based on the application of an external electric field to the sample, so the charged particles in the solution move accordingly. The particles that have a net charge, will migrate towards the oppositely charge electrode[123,124].

For the measurement of the surface charge, an aliquot of 800 µl of the solution previously prepared for the DLS analysis was placed in the zeta cuvette (Paralab, Porto - Portugal), using appropriate standard operation procedure (SOP) in a Zetasizer nano ZS (Malvern, Malvern - United Kingdom).

3.5.4 Determination of exosome-like liposome's cholesterol

For a robust measurement of the mRNA encapsulation efficiency in the exosomes-like liposomes, it was necessary to quantify the lipid concentration of the exosome-like liposomes, by quantifying their cholesterol content. The cholesterol concentration of the liposomes samples was determined against a calibration curve, comprised by six different concentrations of cholesterol made with several dilutions of a standard solution (FUJIFILM) (**figure 15**), by measuring the absorbance at 600 nm. Having the cholesterol concentration, we can infer the total lipid concentration.

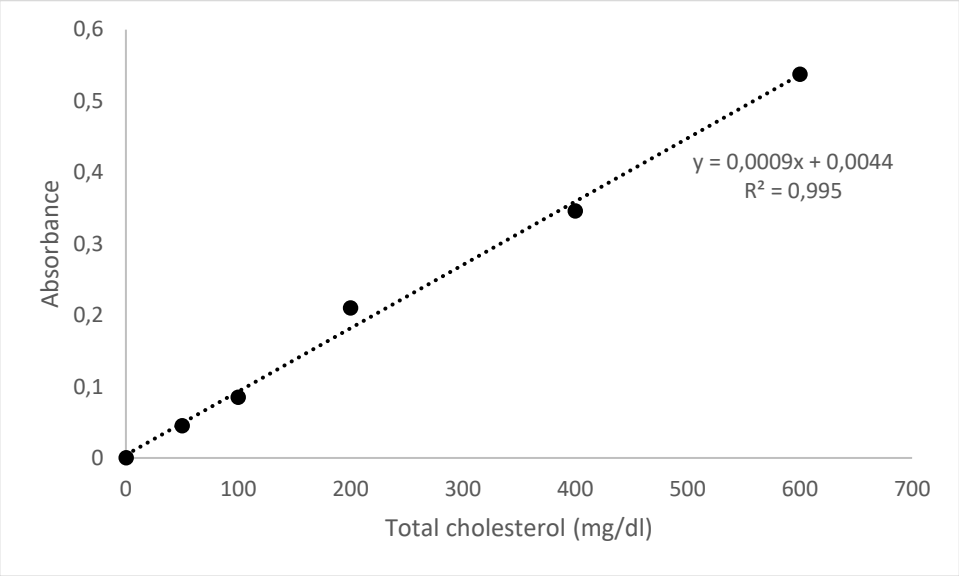


Figure 15. Calibration curve of cholesterol.

3.5.5 Encapsulation efficiency of mRNA

Encapsulation efficiency is one of the most important parameters for exosome-like liposome formulation as it directly reflects the concentration of active RNA molecules incorporated in these systems.

Encapsulated mRNA quantification was performed using RiboGreen, a dye that binds to nucleic acids, and effloresces when intercalated in the RNA molecules, allowing the detection of as little as 1.0 ng/ml RNA[125].

The liposome samples encapsulating RNA where lysed, using $C_{12}E_8$ as detergent, and vigorously pipetting the samples, and the RNA content was quantified against a calibration curve with RNA samples at four different known concentrations of mRNA to whom 10 µl of exosome-like liposomes without mRNA and RNAse free water (DEPC-treated water) were added (**figure 16**). Then, 100 µl of RiboGreen 200X were added to all samples in a 96-well fluorescence plate and the florescence was measured after incubating for 5 min protected from light, at λ_{exc}=485nm and λ_{em}=538 nm in a microplate reader.

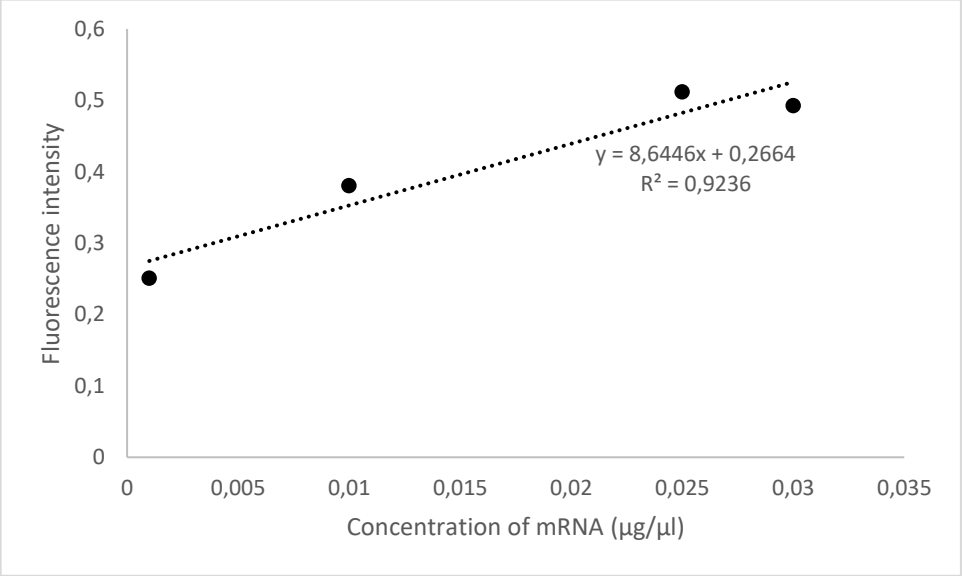


Figure 16. Calibration curve of mRNA to identify mRNA encapsulation efficiency in exosome-like liposomes.

3.5.6 Stability of exosome-like liposomes

Ideal drug carriers should be stable in biological environments and only release their drug load once inside the targeted cells. However, the successful delivery of these systems depends on the intrinsic instability of the physiological environment[126]. The stability of exosome-like liposomes loaded with siRNA was tested in three different conditions, at 37°C: (1) HEPES buffer with pH of 7.4; (2) HEPES buffer with pH of 5.0, and (3) 55% of FBS.

The potential use of liposomes as delivery systems can be limited by the stability of liposomes in the body. To mimic the stability of these systems in the human body, they were tested in HEPES pH 7.4 at 37°C. Additionally, for exosome-like liposomes successfully deliver their cargo, they need to escape the acidic environment of the endosome and then effectively deliver the therapeutic drug in the cytoplasm[127]. To simulate the stability of the liposomes in the endosome, they were submitted to HEPES pH 5.0 at 37°C.

Thus, the liposomes can interact adversely with serum proteins or lipoproteins, provoking irregularities in the lipid bilayer, ultimately leading to vesicle disruption and loss of their contents[128]. To mimic the *in vivo* behaviour of these systems, their stability was tested in 55% FBS at 37°C, the percentage of serum present in the blood[129]. Samples of the exosome-like liposomes in these three conditions were taken at set timepoints to measure the size, PDI and surface charge.

3.5.7 Exosome-like liposomes hemolysis

Hemolysis is the rupture of erythrocytes (red blood cells) and the release of their contents (e.g., hemoglobin) into the surroundings, and can lead to anemia and other pathological conditions. Therefore, the blood compatibility of all intravenously administered pharmaceuticals, such as delivery systems, must be evaluated[130].

This assay was performed using pig blood obtained from the local butcher. The erythrocytes were obtained by washing the blood with a saline solution, by sequential centrifugations at 600 *g*, during 5 mins at 4°C, until a clear supernatant was obtained. Then, the sedimented erythrocytes were resuspended in PBS 1X. Two concentrations of empty exosomes-like liposomes with DODAP were tested: c=50 μg/ml and c=500 μg/ml[102]. The samples were incubated with the red blood cells at 37°C for 30 mins The positive control was performed by adding Triton 10x to the erythrocytes, a surfactant that lyses the cells[131]. After the incubation period, the samples were centrifuged under 600 *g*, for 5 min, at 4°C. The supernatant was collected, and the absorbance of hemoglobin was measured at 541 nm in a microplate reader.

3.5.8 Uptake of exosome-like liposomes for siRNA delivery

The uptake of loaded siRNA exosome-like liposomes was studied in the HEK293 cell line. To follow the uptake of the exosome-like liposomes, these systems were labelled with Oil Red O, a fat-soluble dye used to stain neutral lipids, cholesteryl esters, and lipoproteins[132].

The cells were plated at a density of 1 x 10^5 cells per well, in 24-well plates. After overnight stabilization, the cells were incubated with the exosome-like liposome loaded with siRNA and the respective control, empty exosome-like liposomes, at concentration of 2 x 10^{-4} M, for 1, 3 and 4h. This concentration induces approximately 50% of cell motility, after a 24h incubation period, being the higher concentration previously tested, for these liposomes[133]. The cellular internalization of the exosomes-like liposomes was observed by fluorescence microscopy in the TRITC filter.

3.5.9 Transfection of Luciferase mRNA

The uptake of Luciferase mRNA with lipofectamine was tested on the HEK293 cell line. The cells were plated at a density of 1 x 10^5 cells per well, in 24-well plates. After overnight stabilization, the cells were incubated with the transfection mixture. The transfection mixture was prepared by incubating 20 µl of mRNA (c= 0,05 µg/µl)[134] in 2 µl of Lipofectamine (Invitrogen) for 30 mins at room temperature[135]. Then, the lipoplexes were transferred to a completed DMEM medium without FBS. After 4h, 250 µl of DMEM medium with FBS were added to each well. After 48h, the medium was removed and a lysis buffer Nano-Glo with luciferin (Promega) was added. After 3 mins, the luminescence was measured in 96-well white opaque plate in a microplate reader (Tecan, Infinite MPlex).

3.6 Strategies for the treatment of AD after stablished AD models

After the AD models were established in the neuroblastoma cell line and zebrafish embryos, two therapeutical strategies were tested to counteract the $AlCl_3$ toxicity. First, the effect of anti-Tau siRNA and curcumin delivered by exosome-like liposomes was tested in both established AD models *in vitro* and *in vivo*. Secondly, petrosamine, was tested in the established AD models *in vitro* and *in vivo*. To our knowledge, petrosamine activity on these parameters has never been studied before, *in vitro,* or *in vivo*, as to identify properties of this compound against neurotoxicity.

3.6.1 Delivery of exosome-like liposomes loaded with anti-Tau siRNA and curcumin *in vitro*

To counteract the toxicity induced by aluminium, the effect of exosome-like liposomes loaded with anti-Tau siRNA and curcumin was tested in SH-SY5Y cell line. To evaluate this therapy, were performed two assays: Lactate Dehydrogenase (LDH) assay and RT-PCR, in collaboration with a member of our investigation group, Nelson Gomes. So, the method of RT-PCR will not be mentioned in this thesis, since it was already described previously[136]. LDH is a cytoplasmic oxidoreductase and, in the presence of reduced nicotinamide adenine dinucleotide (NADH), converts pyruvate to lactate. The leakage of LDH into the extracellular space in neurons culture is provoked by the presence of compromised or dead cells. In the presence of pyruvate and NADH, the LDH enzyme promotes the catalysis into lactate and NAD^+, and the LDH assay allows to access the levels of the enzyme from the neuron culture media based on the measurement of the NADH production spectrophotometrically. The cells were incubated at a cellular density of 1 x 10^5 cells per well in a 24-well microplate.

After overnight seeding, the cells were incubated with only one concentration of $AlCl_3$ (200 µM) for 24 h at 37° C. The supernatant was collected to Eppendorf's and centrifuged at 14000 rpm for 1 min. The supernatant was transferred to 96-well plates and stored at 4° C until the time of the assay. To dilute pyruvate, a solution of KH_2PO_4 (50 mM, pH 7.4) was prepared to dilute pyruvate (7 mM) and NADH (0.4 mM). Then, 200 µL of NADH solution were added to each well, and the plate is placed in the reader to warm up at 30° C. Afterwards, 10 µL were added to each well and the measured each 10 s during 3 min at 340 nm.

3.6.2 Delivery of exosome-like liposomes loaded with anti-Tau siRNA and curcumin *in vivo*

To counteract the toxicity induced by aluminium, the effect of exosome-like liposomes loaded with anti-Tau siRNA and curcumin was tested in zebrafish embryos. Embryo treatments were performed in 24-well plates with 10 embryos per well. The plates were incubated at 26°C and to each well were added 2 ml of test solutions renewed daily. Embryos were exposed to 50 µM and 200 µM of $AlCl_3$ during the first 72 hpf. At this time point, the $AlCl_3$ solutions were substituted by a mixed solution of exosome-like liposomes encapsulating anti-Tau siRNA (c=200 µM) and of exosome-like liposomes loaded with curcumin (c=200 µM), since the co-encapsulation of siRNA and curcumin in these systems have a lower encapsulation efficiency[118]. The embryos were subjected to this treatment until 120 hpf. The larvae were euthanized in the cold and stored at -20°C for the measurement of AChE activity, completed according to section 3.4.2.

3.6.3 Petrosamine as a therapy for AD

3.6.3.1 Biocompatibility of petrosamine

To test the biocompatibility of petrosamine it was performed the resazurin assay in the SH-SY5Y cell line, the survival rate of zebrafish embryos and the hemolysis assay with the following concentrations: 0.01, 0.05, 0.1 and 0.15 mg/ml. To test the biocompatibility of petrosamine in the zebrafish embryos, they were treated with the four concentrations of this natural compound from 72 hpf until 120 hpf and was observed their survival rate.

3.6.3.2 Effect of petrosamine in the established neuroblastoma cell line AD model

For these studies, two assays were performed (1) the measurement of lipid peroxidation and (2) the measurement of AChE activity. The SH-SY5Y cells were seeded into 96-well plates at a cellular density of 2 x 10^4 cells/well in 96-well plates. After seeding, they were incubated with the three stablished concentrations of $AlCl_3$ (50 µM, 200 µM and 1000 µM) for 24 h, at 37°C. The next day, the medium with $AlCl_3$ was removed and the petrosamine stock solution (c=1 mg/ml) was diluted in medium to obtain a final concentration of 0.05 mg/ml. The cells were left for another 24 h at 37°C. Then, the protocol to measure lipid peroxidation was followed exactly as mentioned in section 3.3.5, with the measurement of the AChE activity performed as indicated in section 3.3.6.

3.6.3.3 Effect of petrosamine in the established zebrafish embryos AD model

To evaluate the effect of petrosamine against aluminium toxicity in zebrafish embryos the FET was conducted. Embryo treatments were performed in 24-well plates with 10 embryos per well. The plates were incubated at 26°C and 2 ml of test solutions were added to each well, with each test condition being renewed every day of the treatment. Embryos were exposed to 50 µM and 200 µM of $AlCl_3$ during the first 72 hpf. At this time point, the $AlCl_3$ solutions were substituted by petrosamine (c= 0,05 mg/ml) until 120 hpf. The survival and hatching rate, the cardiac frequency and the yolk volume were evaluated. The larvae were euthanized in the cold and stored at -20°C for subsequently biochemical analyses. The AChE activity was assessed according to the description in section 3.4.6.

3.7 Statistical Analyses

The results were obtained from at least two independent experiments (n) and expressed as mean ± standard deviation (SD). All different statistical analyses were performed using GraphPad Prism version 8.3.4. for Windows, GraphPad Software, La Jolla California USA. Statistical significance of the results was determined using one-way ANOVA. Differences were considered statistically significant at $P<0.05$.

Chapter 4

Results

4. Results

4.1 Establishment of AD model in neuroblastoma cell line

For the establishment of AD model in the neuroblastoma cell line SH-SY5Y, the cells were submitted to $AlCl_3$ (50 μM, 200 μM and 1000 μM) toxicity for 24h and different assays were completed in order to validate this model.

4.1.1 Resazurin assay

The resazurin assay was used to monitor the viability of the SH-SY5Y cells, under the influence of three concentrations of $AlCl_3$. Two controls were included: a negative control and a positive control. The percentage of cell survival for each sample was expressed and normalized against the negative control (100% viability). Living cells are metabolically active and are able to reduce the nonfluorescent dye resazurin to the strongly-fluorescent dye resorufin in the mitochondria. Incubation of the substrate with viable cells will result in generation of a fluoresce signal that is proportional to the number of viable cells present. The results are expressed in **figure 17**.

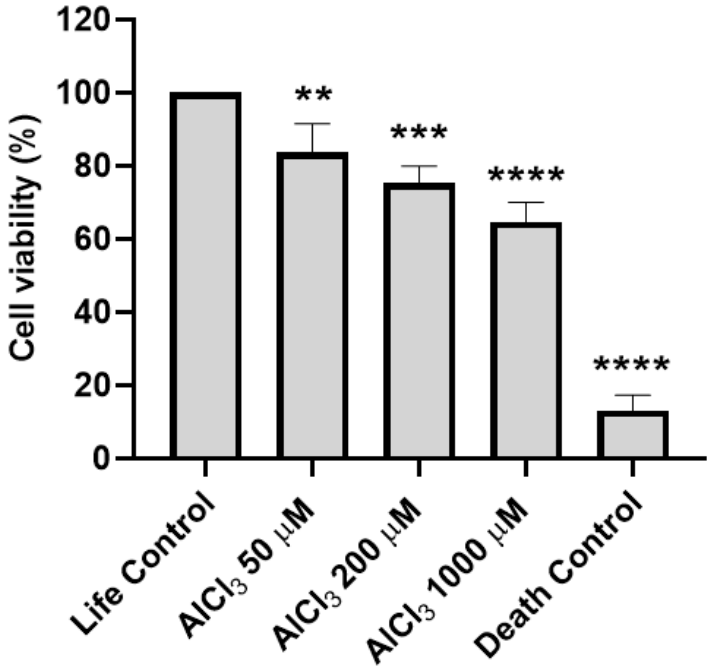


Figure 17. Cell viability (**3n**) after SH-SY5Y cell's exposure to three different concentrations of $AlCl_3$ (50 μM, 200 μM, and 1000 μM) for 24h. The results were expressed in relation to negative control (100%). Significant differences were identified ** $p < 0.01$, *** $p < 0.001$, **** $p < 0.0001$ as compared to negative control.

The results showed that $AlCl_3$ induced a dose-dependent reduction in cell viability, and direct cytotoxic effects that eventually lead to cell death. The results obtained are corroborated by the statistical analysis. The $AlCl_3$ concentration of 50 µM showed the least statistical significance with 16% less viability than the negative control, while the $AlCl_3$ concentration of 1000 µM had the higher statistical significance, equal to the death control, with 36% less viability compared to the negative control.

4.1.2 SRB assay

The SRB assay was also used to screen the cytotoxicity of $AlCl_3$ in the SH-SY5Y cell line. This assay is based in cell density determination, by measuring the total protein mass, which correlates with the number of cells. The results were normalized against the negative control (100% viability) and are presented in **figure 18**.

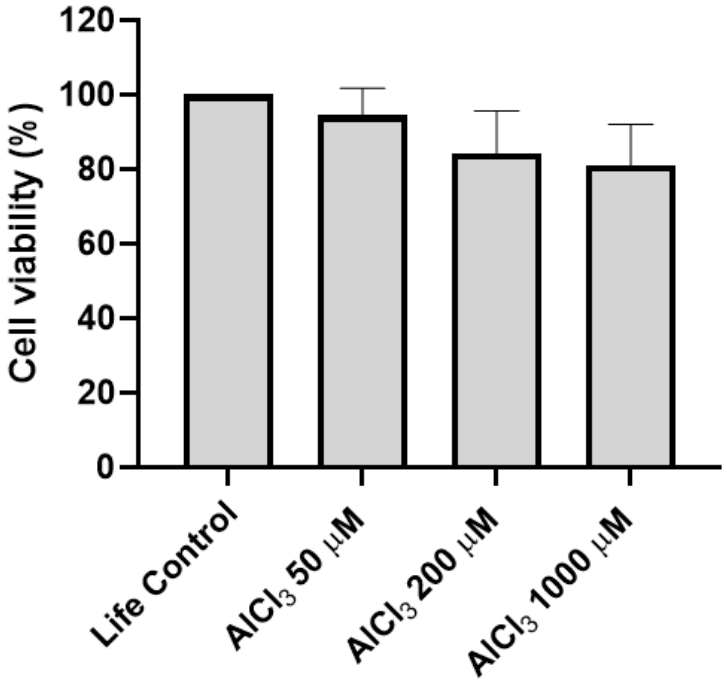


Figure 18. Cell viability (**3n**) after SH-SY5Y cell's exposure to three different concentrations of $AlCl_3$ (50 µM, 200 µM, and 1000 µM) for 24h. The results were expressed in relation to negative control (100%). No significant statistical differences were detected.

The results did not show statistically significant differences between the tested conditions, possibly due to wide error bars. However, the results show an evident trend, as cell viability decreases with the increase in $AlCl_3$ concentration.

4.1.3 Acridine Orange (AO)/ Propidium Iodide (PI) assay

Finally, AO/PI assay was used to determine the effect of $AlCl_3$ on cell viability. Both AO and PI are nucleic acid binding dyes, however, while AO is a cell permeable green fluorescence probe, PI is a red fluorescent probe that only dyes cells with compromised cell membranes and, consequently, stains apoptotic or necrotic nucleated cells.

For this assay, two controls were included, the negative control (**figure 19a**) and the positive control (**figure 19e**). The double staining of the cells incubated with $AlCl_3$ is presented in **figures 19b** to **19d**. Finally, the percentage of viable, early apoptotic, and apoptotic cells of each condition can be observed in **figure 19f**.

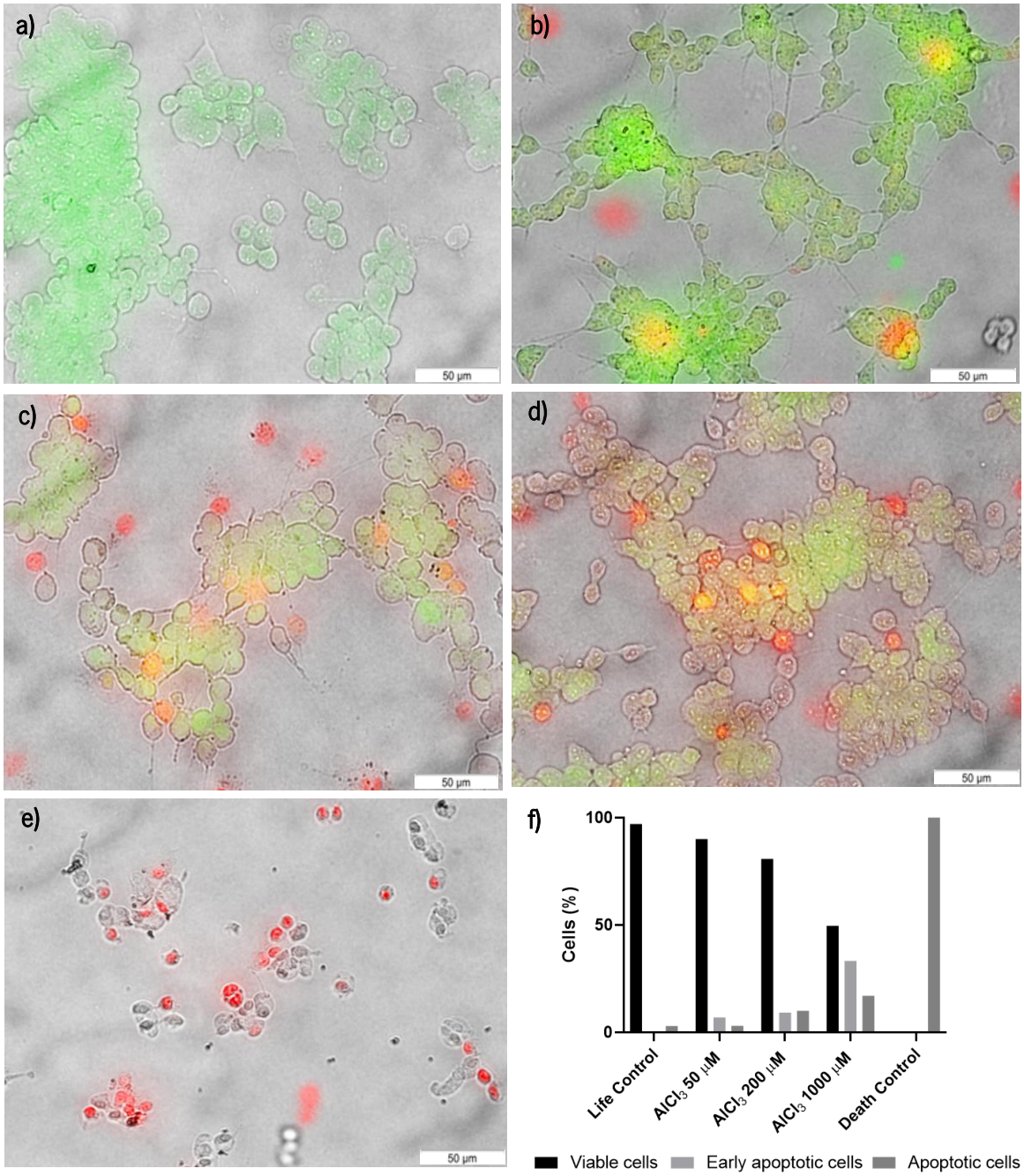


Figure 19. Microscopy of fluorescence of AO/PI assay showing SH-SY5Y cell line exposed to different concentrations of $AlCl_3$ for 24h. (a) Negative Control; (b) 50 µM $AlCl_3$; (c) 200 µM $AlCl_3$; (d) 200 µM $AlCl_3$; (e) Positive Control (30% DMSO). Scale bar = 50 µm. Graph (f) represents the number of viable cells (green), early apoptotic cells (yellow), and apoptotic cells (red) in each condition.

Green fluorescence on the nucleus of the cells is indicative of their viability, as cells labelled with yellow fluorescence indicate an early apoptotic state and those stained with red fluorescence indicates the cells that are undergoing apoptosis. The life control has 100% of viable cells, whereas 90% of cells incubated with 50 µM of $AlCl_3$ are viable, 80% of cells incubated with 200 µM of $AlCl_3$ are viable, 50% of cells incubated with 1000 µM of $AlCl_3$ are viable, and in the death control we can see that 0% of cells are viable. Additionally, the number of early apoptotic and apoptotic cells increases with higher concentrations of $AlCl_3$.

4.1.4 Determination of Reactive Oxygen Species - DCFDA assay

DCF was used as a fluorescent indicator of intracellular ROS formation. When H_2DCFDA is applied to the cells, it diffuses through the cell membrane into the cytoplasm, where the acetate groups are cleaved by esterase enzymes, trapping the H_2DCF inside the cells. Then, in the presence of ROS, H_2DCF is rapidly oxidized to DCF, a highly fluorescent molecule. Two controls were considered in this assay: the negative control and the positive (oxidant) control, with t-BHP (c= 1mM). The percentage of ROS for each sample was expressed and normalized against the positive control (oxidant t-BHP) (**figure 20**).

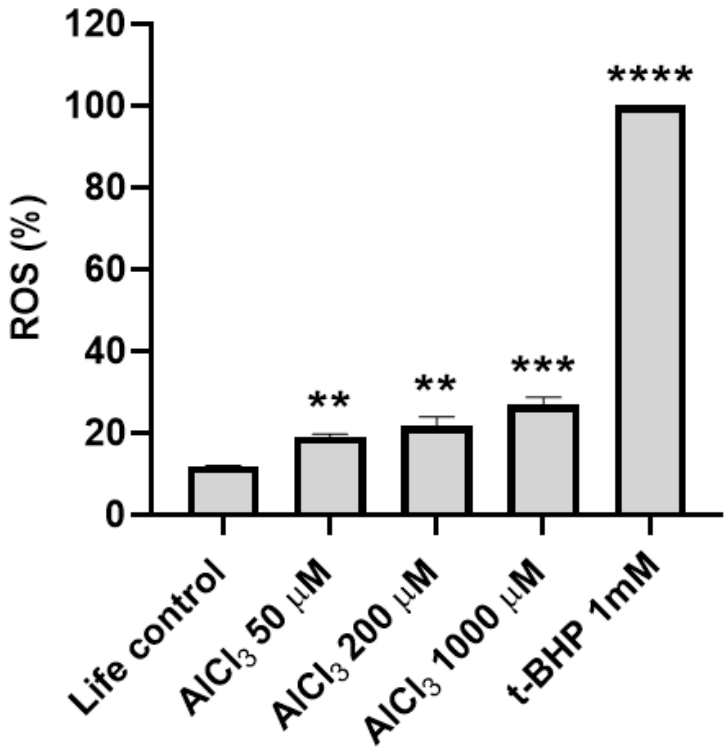


Figure 20. Reactive oxygen species quantified with the DCFHDA probe (**2n**) after SH-SY5Y cell's exposure to three different concentrations of $AlCl_3$ (50 µM, 200 µM, and 1000 µM) for 24h. Verified a significant statistical difference among means. ** $p < 0.01$, *** $p < 0.001$, **** $p < 0.0001$ as compared to the oxidant t-BHP (1mM).

The results obtained revealed that $AlCl_3$ induced production of ROS, which can lead to mitochondrial oxidative damage. The increasing $AlCl_3$ concentration has a direct correlation with the rising levels of ROS. A 38%, 45% and 56% increase in ROS levels is observed in cells exposed to 50, 200 and 1000 µM $AlCl_3$, respectively, when compared to the negative control. There is a statistically significant difference between all concentrations, with the 1000 µM concentration showing more statistical relevance.

4.1.5 Determination of lipid peroxidation

Lipid peroxidation occurs when ROS react with susceptible unsaturated lipids on the cell membrane, potentially causing irreversible damage. To determine the lipid peroxidation in SH-SY5Y cells, the TBARS assay was performed. This method measures MDA, one of the several end products formed through the oxidation of lipid substrates. The percentage of lipid peroxidation of each sample was expressed and normalized against the negative control (**figure 21**).

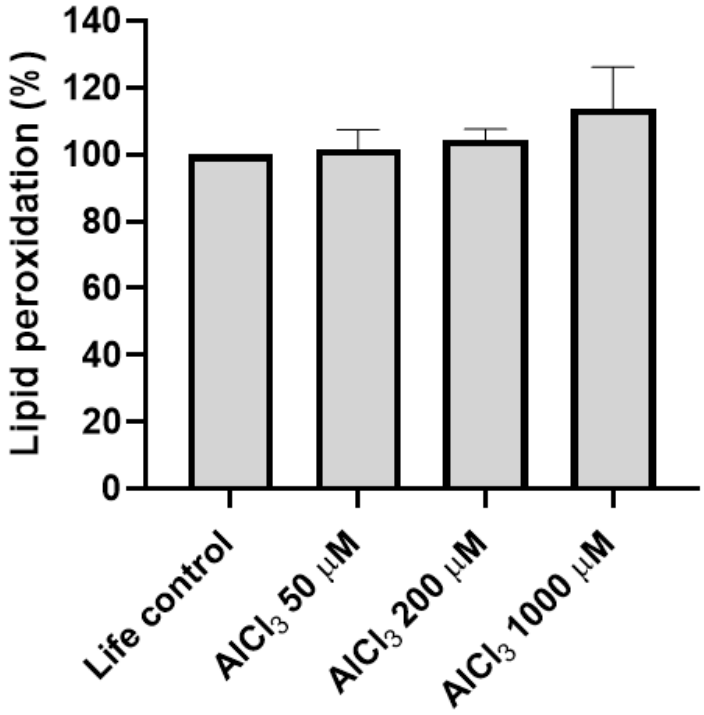


Figure 21. Lipid peroxidation percentage (**3n**) after SH-SY5Y cell's exposure to three different concentrations of $AlCl_3$ (50 µM, 200 µM, and 1000 µM) for 24h. The results were expressed in relation to negative control (100%). No significant differences were detected.

As observed in **figure 21**, there is no statistically significant difference in lipid peroxidation of cells submitted to treatment with the different concentrations of $AlCl_3$. However, a clear trend is verified with the percentage of lipid peroxidation increasing with higher concentrations of $AlCl_3$.

4.1.6 Determination of AChE activity

AChE is an important enzyme in the nervous system that hydrolyses the acetylcholine substract into acetate and thiocoline. The measurement of AChE activity is based on two steps: (1) quantification of total protein and the (2) measurement of AChE activity. The first step was to quantify the protein content, with the Bradford protein assay, a dye-binding assay based on the differential colour change of the dye in response to various protein's concentrations. The detection of AChE activity was possible by following the reaction between thiocoline and Ellman's reagent (DTNB), that yields a yellow chromophore that was followed photometrically. The results obtained can be observed in **figure 22**.

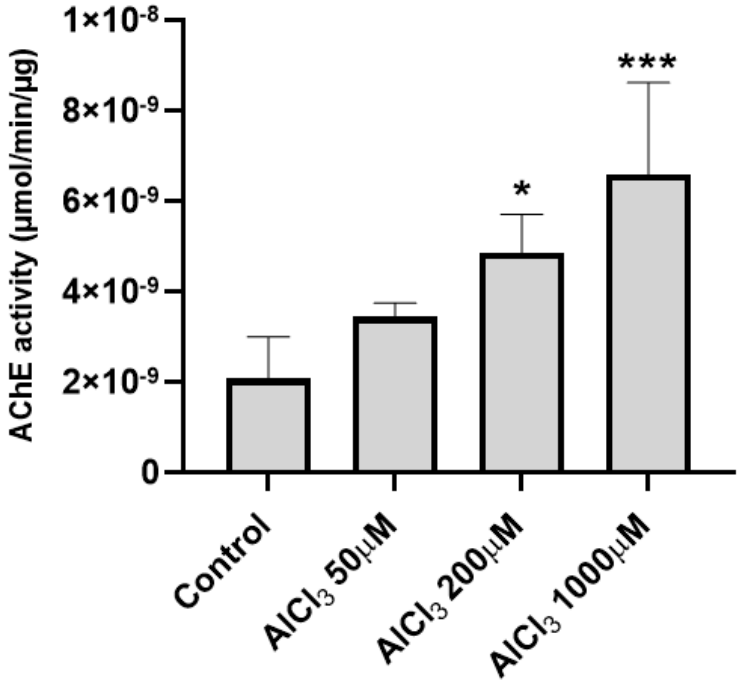


Figure 22. AChE activity (**4n**) after SH-SY5Y cell's exposure to three different concentrations of $AlCl_3$ (50 µM, 200 µM, and 1000 µM) for 24h. Verified a significant statistical difference among means. * $p < 0.05$, *** $p < 0.001$ as compared to the negative control.

Higher activity of acetylcholinesterase in the CNS is a hallmark of AD. In the results shown in **figure 22**, it is visible that the activity of this enzyme increases with the increasing concentration of $AlCl_3$. The AChE cellular activity of the cells incubated with 50, 200 and 1000 µM of $AlCl_3$ increased approximately 40%, 57% and 68%, respectively, compared to the negative control. Only the concentration of 200 and 1000 µM promotes an increment in the AChE activity with statistical relevance.

4.2 Establishment of AD model in zebrafish embryos

For the establishment of the AD model in zebrafish embryos, the FET assay during the 120 hpf was performed. The zebrafish embryos were submitted to $AlCl_3$ (50 µM and 200 µM) toxicity, in the first 72 hpf. Several phenotypic parameters were evaluated, and biochemical assays were also performed to validate this model.

4.2.1 Survival rate and Hatching rate of zebrafish embryos

To evaluate the neurotoxicity provoked by $AlCl_3$, the survival rate was evaluated every 24h until the 120 hpf (**figure 23a**). Additionally, the hatching rate was observed every 24h only until 72hpf, the timepoint when there is 100% of hatching (**figure 23b**).

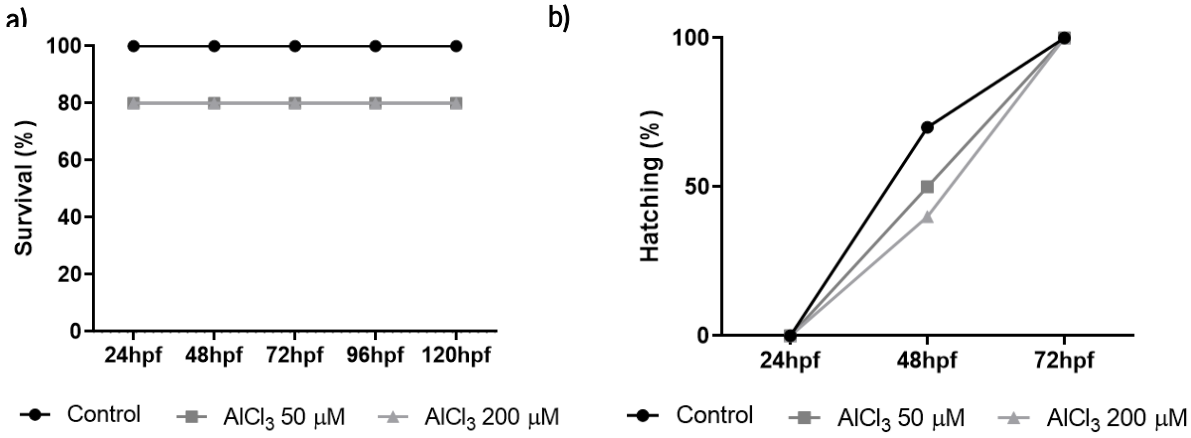


Figure 23. Analysis of zebrafish embryos development: (a) survival rate and (b) hatching rate.

The survival rate decreased by 20% in the first 24 hpf, both for the embryos treated with 50 µM and 200 µM of $AlCl_3$, when compared to the life control (100% survival), a value that is maintained during the remaining of the treatment.

The hatching rate has decreased 40% and 75% at 48 hpf, for the zebrafish embryos submitted to 50 µM and 200 µM of $AlCl_3$, respectively, when compared to the life control. However, at 72 hpf, all conditions had 100% of hatching.

4.2.2 Phenotypic Parameters of zebrafish embryos

The zebrafish embryos submitted to the neurotoxic effect of $AlCl_3$ were observed every 24h until 120hpf, regarding several phenotypic parameters, including epiboly, yolk volume, pupil volume, cardiac frequency, and larvae length. The embryos exposed to the two $AlCl_3$ concentrations developed phenotypic alterations in the parameters referred previously (**figure 24**) and developed phenotypic alterations concerning pericardial edema (**figure 25**).

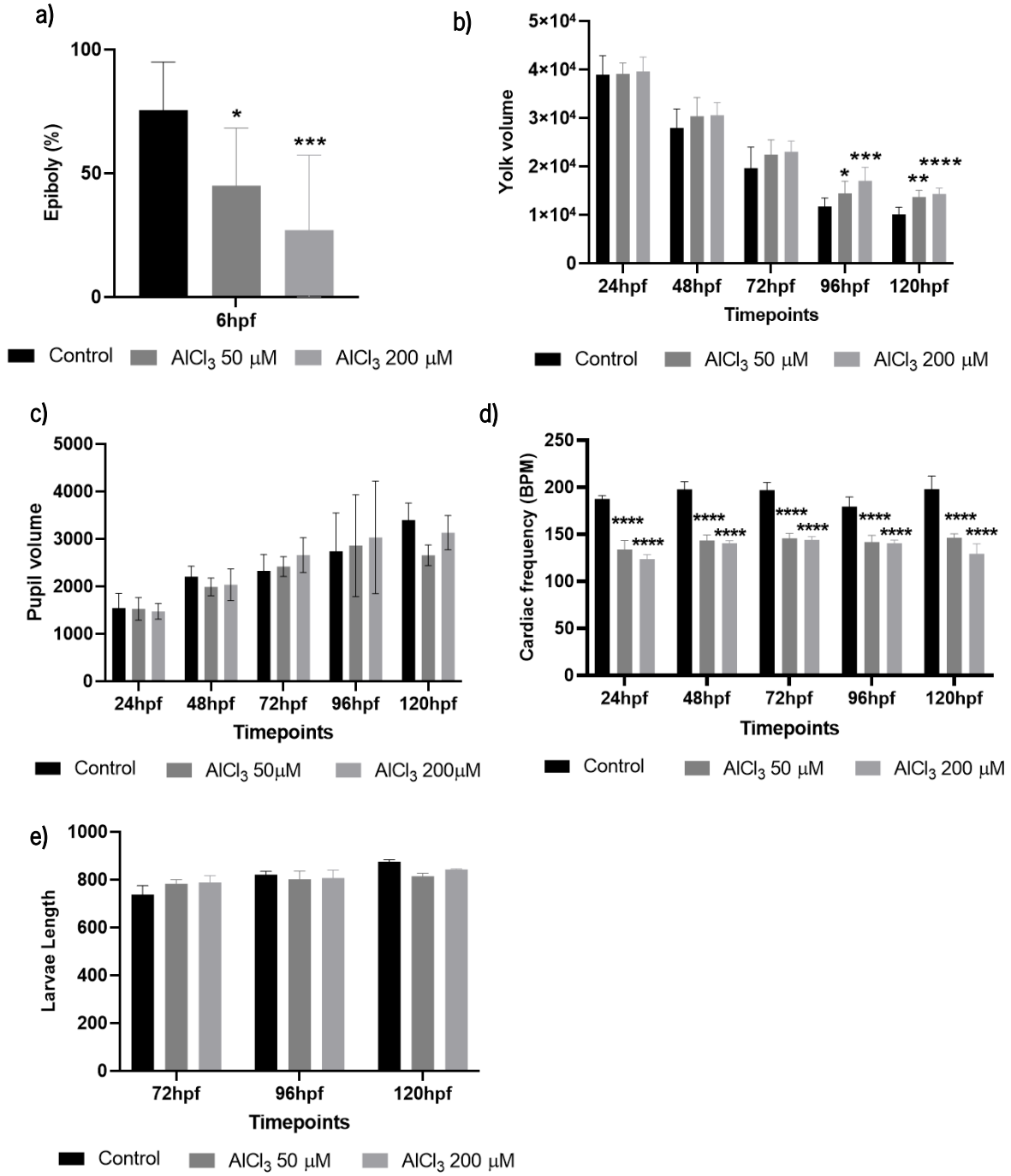


Figure 24. Phenotypic parameters. (a) Epiboly percentage, (b) Yolk volume, (c) Pupil volume, (d) Cardiac frequency, and (e) Larvae length.

Statistically significant differences between the embryos exposed to $AlCl_3$ and the control were observed in all phenotypic parameters, except for the pupil volume (**figure 24c**) and larvae length (**figure 24e**). Regardless, in both of these parameters a delayed development in the zebrafish embryos exposed to $AlCl_3$ was observed, compared to the control.

Epiboly is the first morphogenetic cell movement, initiated during zebrafish embryogenesis, that occurs during gastrulation[137]. The epiboly percentage (**figure 24a**), measured at 6 hpf, decreased when the embryos were in contact with a concentration of 50 µM of $AlCl_3$ and an even more significant decrease was verified, when the embryos are exposed to the concentration of 200 µM of $AlCl_3$, when compared to the control. This difference of epiboly between the control and the test conditions, indicates that the embryos exposed to $AlCl_3$ have a slower development.

A difference in the yolk volume can be observed at 48 hpf (**figure 24b**). At this timepoint, the yolk volume of the embryos treated with both conditions of $AlCl_3$ is higher than the control. However only the differences at 96 hpf and 120 hpf are of statistical significance. At these development stages, a difference between the embryos treated with the two concentrations of $AlCl_3$ is also observed, of which the concentration of 200 µM has a greater statistical significance, due to the higher yolk volume. The effect of $AlCl_3$ in the yolk volume translates into a diminished development of the zebrafish, since the yolk provides an energy source for the developing organism, being considered a nutrient reserve. If the yolk volume does not reduce overtime, it can be considered that the organism development is delayed.

The $AlCl_3$ exposure extremely diminished the cardiac frequency, and as early as the 24 hpf. Both $AlCl_3$ concentrations promote differences in the cardiac frequency with the same statistical significance every 24h. The zebrafish embryos of the control have a cardiac frequency always around 200 beats per minute, while the zebrafish embryos exposed to $AlCl_3$ have less or equal to 150 beats per minute.

As an example, in **figure 25**, a zebrafish embryo exposed to $AlCl_3$ (c= 50 µM) during the first 72 hpf can be observed. In **figure 25a** the embryo has a 30% epiboly stage at 6 hpf. Additionally, a pericardial edema was visible at 48 hpf of the treatment signalled by an arrow in **figure 25c**.

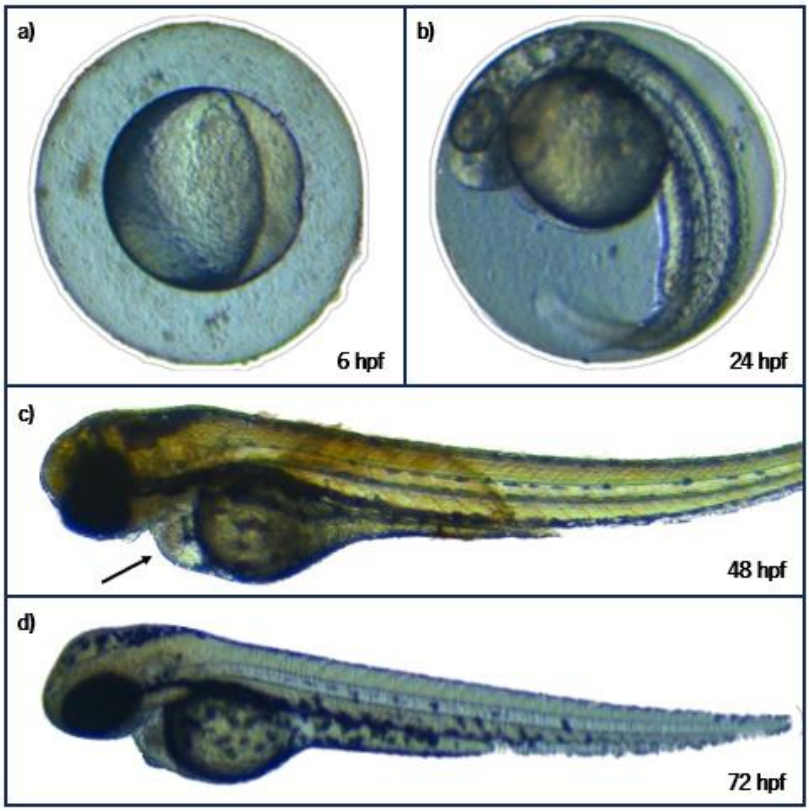


Figure 25. Zebrafish embryos submitted to 50 μM of $AlCl_3$ at (a) 6hpf, (b) 24hpf, (c) 48hpf, and (d) 72hpf. Arrow indicated a pericardial edema.

4.2.3 Analysis of Apoptosis

Acridine orange staining was used to analyse the apoptosis in control larvae, with normal phenotype, and larvae treated with 50 and 200 μM of $AlCl_3$, at 120 hpf, by fluorescence microscopy (**figure 26**).

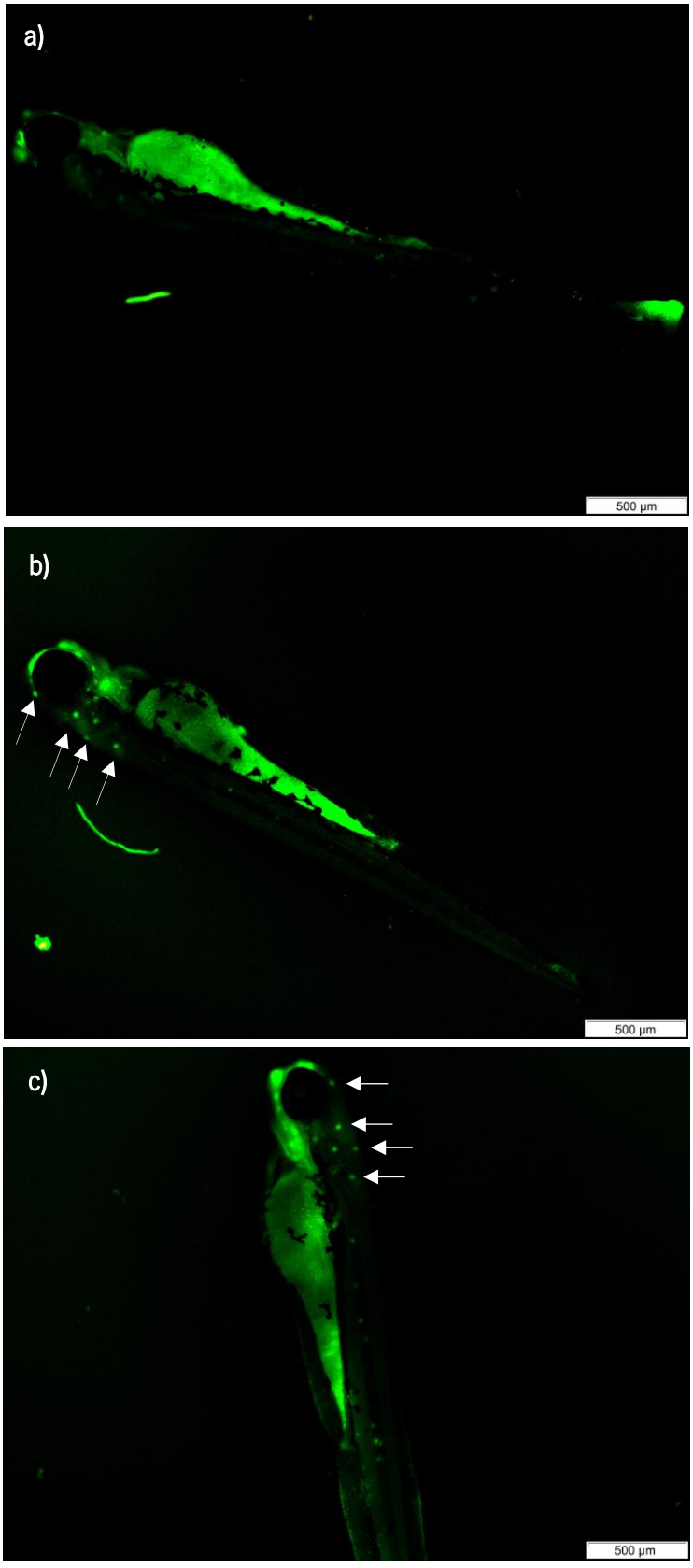


Figure 26. Acridine orange staining in zebrafish larvae with 120 hpf. (a) Whole body of Control larvae; (b) Whole body of larvae exposed to 50 µM $AlCl_3$; (c) Whole body of larvae exposed to 200 µM $AlCl_3$; and (d) Total fluorescence of green spots indicating identified apoptotic cells. Particular fluorescent cellular accumulations are indicated by arrows. Scale bar= 500 µm.

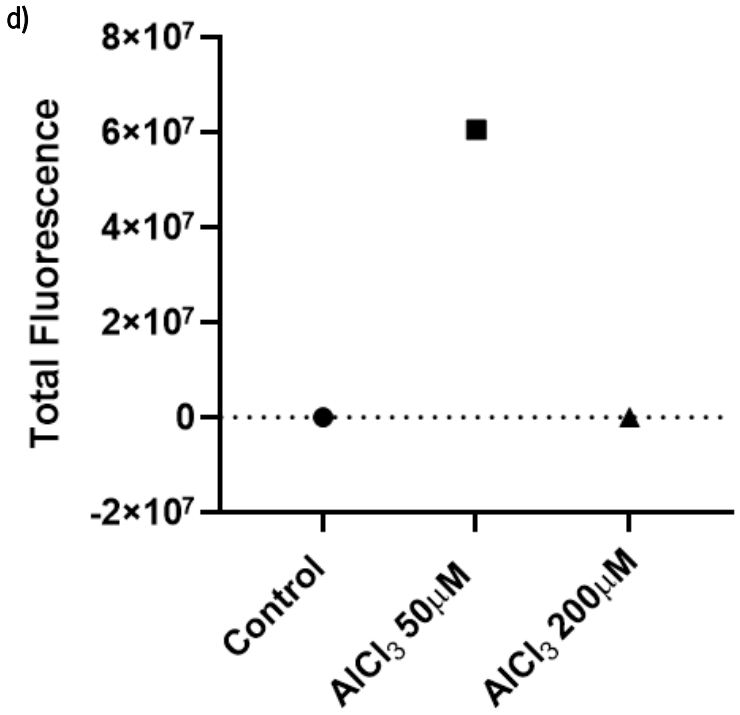


Figure 26. *Cont.*

A physiological presence of apoptotic cells can hardly be seen in control larvae (**figure 26a**). A particular distribution of apoptotic cells was observed in the head of treated larvae exposed to 50 μM (**figure 26b**) and 200 μM (**figure 26c**), in which apoptosis was localized in groups of cells of circumscribed area (indicated by arrows).

With the aim to better understand which concentration of $AlCl_3$ leads to a superior amount of apoptosis, was determined the fluorescence intensity of each green spot in the **figures 26a-c** in ImageJ software. As it is verified in **figure 26d**, the 50 μM concentration of $AlCl_3$ induces the higher level of apoptotic spots, as seen by an extremely higher fluorescence intensity, compared to the control and to the concentration of 200 μM of $AlCl_3$.

In **figure 26a-c**, a specific pattern of apoptotic spots was clearly visible, that suggests they are neuromasts, as explained in **figure 27**. *Manuel et* al. identified the local of neuromasts in the zebrafish lateral line[138] and a comparison between the neuromasts identified by these researchers and the green apoptotic spots identified in this thesis is represented in **figure 27**.

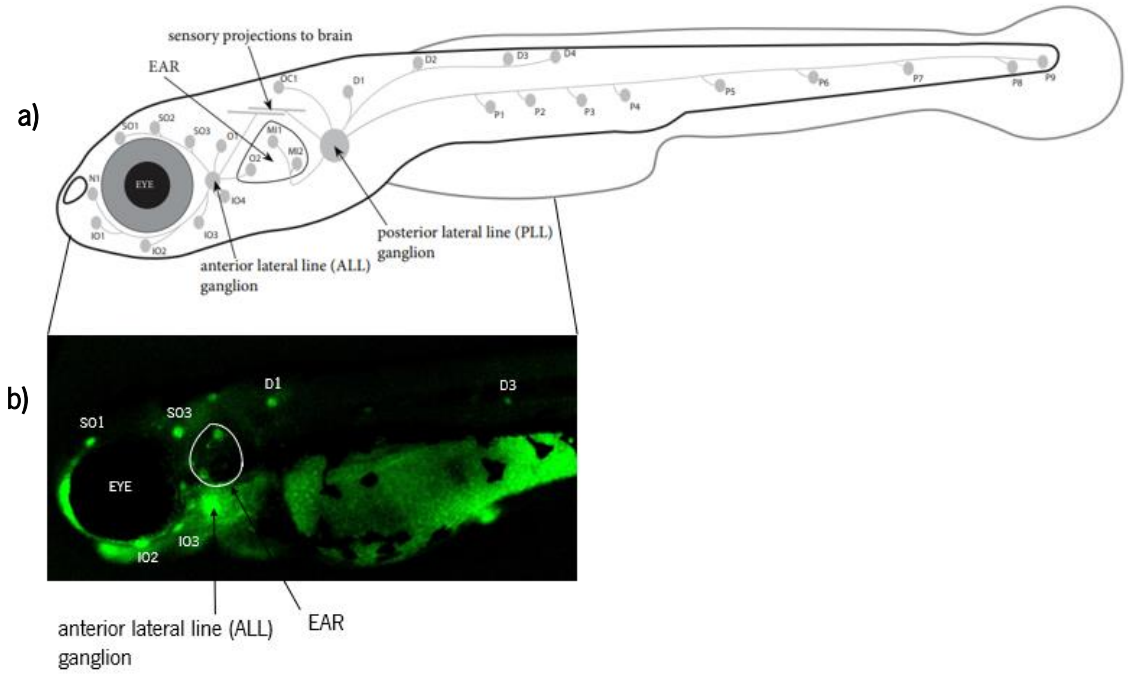


Figure 27. Schematic overview of the lateral line in zebrafish. (a) Location of the neuromasts in a zebrafish larva at 120 hpf. (b) Location of the neuromasts under apoptosis of zebrafish larvae submitted to 50 μM of $AlCl_3$ at 120 hpf. The neuromasts, the anterior and posterior sensory ganglia and the projections they send to the neuromasts and into the brain are indicated. Figure a) is edited from [138].

4.2.4 Determination of Lipid peroxidation

The TBARS assay is a method that was used to detect lipid peroxidation in zebrafish larvae with 120hpf (**figure 28**). The percentage of lipid peroxidation for each sample was expressed and normalized against the control.

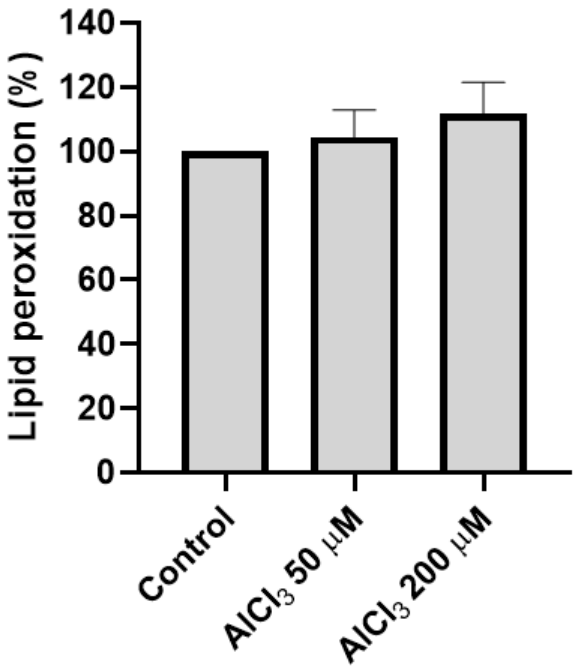


Figure 28. Lipid peroxidation percentage of whole body of larvae with 120 hpf after exposure to two different concentrations of $AlCl_3$ (50 µM and 200 µM). Not verified a significant difference among means.

In this assay no statistically significant difference was verified between the control larvae and the larvae submitted to the two concentrations of $AlCl_3$. However, a trend, in which the increase of the lipid peroxidation is directly proportional to the increase of the concentrations of $AlCl_3$ can be seen.

4.2.5 Determination of AChE activity

As mentioned previously, AChE activity is one of the main hallmarks of AD, its measurement is a fundamental assay to evaluate the strength of an AD model. The measurement of AChE activity, in zebrafish larvae with 120 hpf, was preformed according to Elman's assay (**figure 29**).

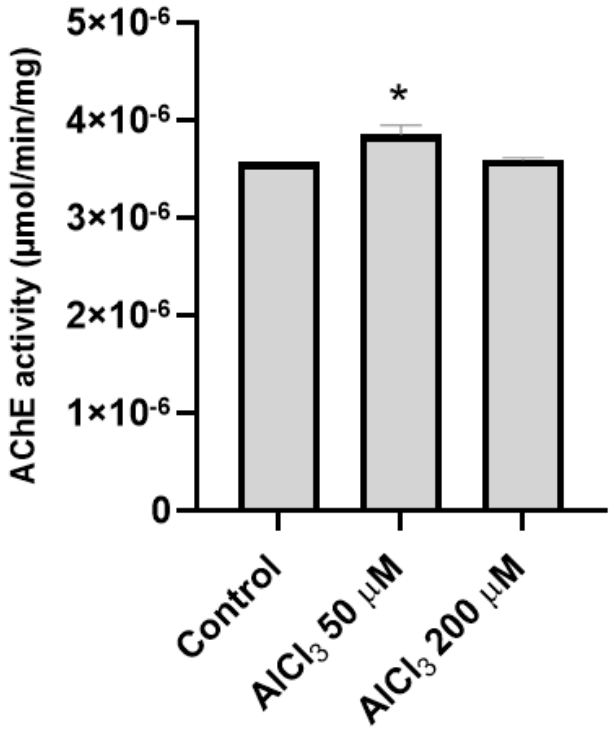


Figure 29. AChE activity of whole body of larvae with 120 hpf after exposure to two different concentrations of $AlCl_3$ (50 µM and 200 µM). Verified a significant statistical difference in $AlCl_3$ 50 µM * $p < 0.05$ as compared to the control.

Statistically significant differences were only observed with the concentration of 50 µM of $AlCl_3$, with an increase of 7% in AChE activity compared to the control. The AChE activity of the zebrafish embryos submitted to 200 µM of $AlCl_3$ was not statistically different to the control.

4.3 Characterization of exosome-like liposomes for RNA delivery

Exosome-like liposomes were produced for the vehiculation and delivery siRNA or mRNA, to develop RNA-based therapies for the treatment of AD. These systems were characterized in terms of size and PDI, by DLS, surface charge, by ELS, encapsulation efficiency, stability cytotoxicity and cellular uptake.

4.3.1 Size, PDI and zeta potential of exosome-like liposomes loaded with RNA

The size and PDI of exosome-like liposomes empty and loaded with siRNA and mRNA was measured by DLS (**figure 30a**), while the surface charge was de determined by measuring the ζ-potential by ELS (**figure 30b**).

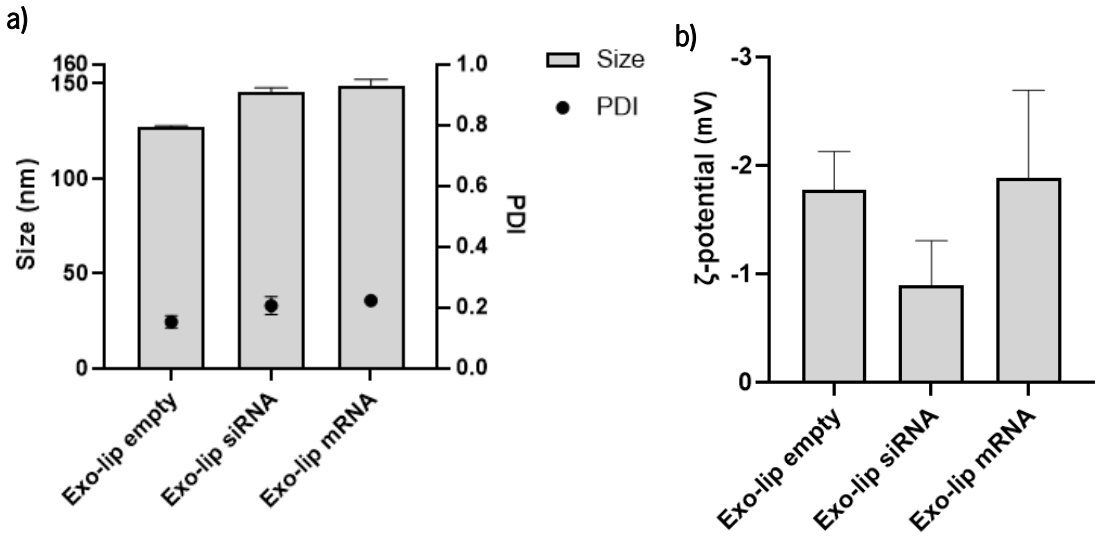


Figure 30. Characterization of empty exosome-like liposomes, exosome-like liposomes loaded with siRNA, and exosome-like loaded with mRNA. (a) Size and polydispersity index (PDI); (b) ζ-potential.

All exosome-like liposomes have a lower size than 150 nm and a PDI of approximately 0.2. Exosome-like liposomes loaded with siRNA have a size of 145.8 nm and exosome-like liposomes loaded with mRNA have a size of 149.1 nm. The surface charge of both liposomes is slightly negative, being almost neutral in HEPES buffer.

4.3.2 Encapsulation efficiency of mRNA

To determine the encapsulation efficiency of mRNA (**table 4**) in the exosome-like liposomes, first was essential to quantify the cholesterol of these systems, to calculate their final lipid concentration, as during the purification of the liposomes they are diluted, and the exact concentration becomes unknown. So, the quantification of cholesterol was fundamental to obtain the highest robust value possible in the encapsulation efficiency of mRNA.

The encapsulation efficiency of mRNA was determined with the help of the RNA intercalation probe Ribogreen and was shown to be 100%.

Table 4. Encapsulation efficiency of exosome-like liposomes loaded with mRNA.

Samples	Encapsulation Efficiency (%)
Exosome-like liposomes with mRNA	100

4.3.3 Stability in physiological conditions

The short-term stability of the exosome-like liposomes loaded with siRNA was measured over time at different timepoints until 24h, in three different conditions: HEPES pH 7.4, HEPES pH 5.0 and FBS, at 37° C.

4.3.3.1 Stability with HEPES pH 7.4 at 37°C

Figure 31 shows the size PDI and ζ-potential of the siRNA-loaded liposomes, over time, when incubated with HEPES buffer with a pH 7.4, at a temperature of 37°C, to mimic their circulation in the human body.

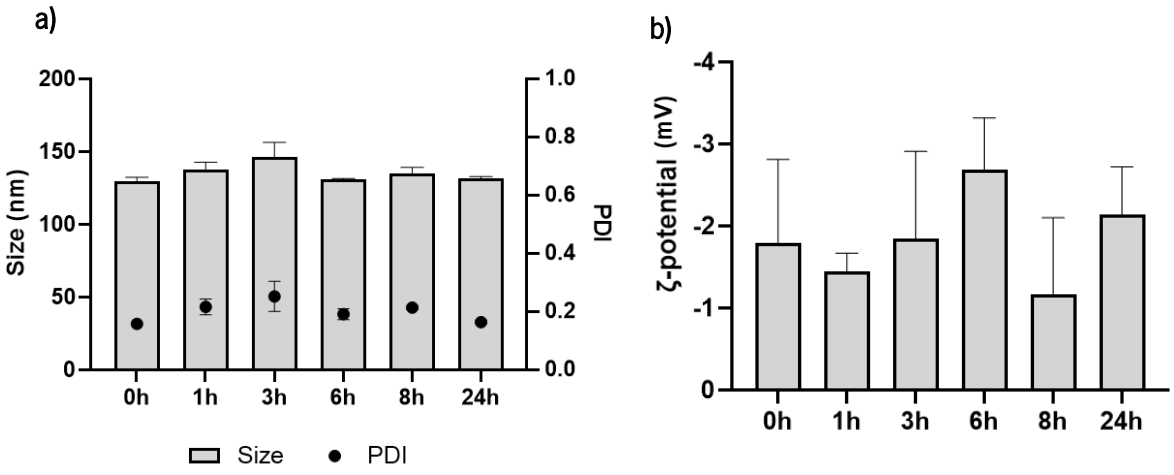


Figure 31. Stability of siRNA-loaded liposomes in HEPES pH 7.4 at 37°C. (a) Size and PDI. (b) ζ-potential.

As visible in **figure 31**, the size, PDI and ζ-potential, are stable during the timeline of the experiment, meaning that these systems are stable in similar conditions to those of the systemic circulation.

4.3.3.2 Stability with HEPES pH 5.0 at 37°C

The size, PDI and ζ-potential of the siRNA-loaded liposomes, when diluted in HEPES pH 5.0, was measured (**figure 32**). Exosome-like liposomes hold great potential to deliver therapeutic agents but can be hindered by entrapment in the endosome and end up in lysosomes, with an acidic pH of 5.0.

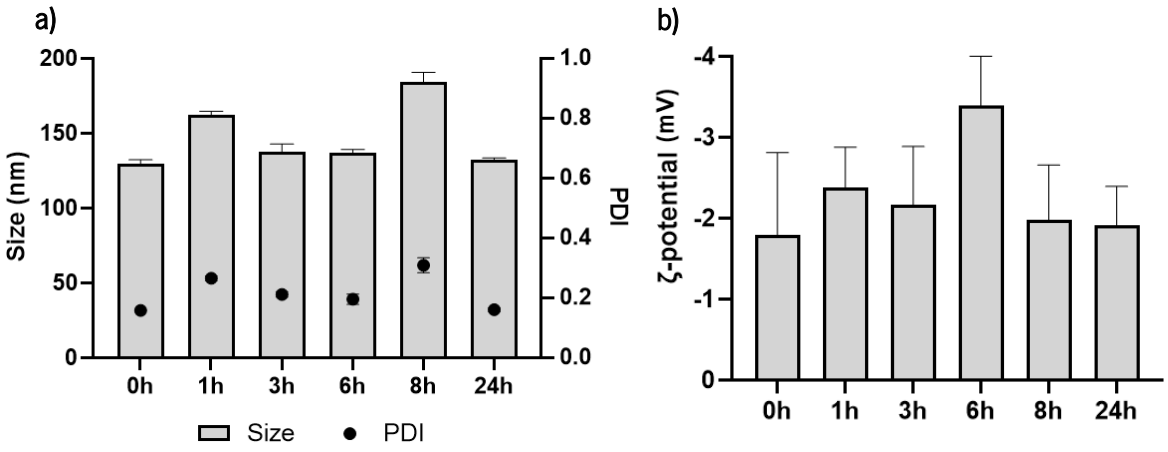


Figure 32. Stability of siRNA-loaded liposomes in HEPES pH 5.0 at 37°C. (a) Size and PDI. (b) ζ-potential.

As can be observed in **figure 32**, when the liposomes are incubated with HEPES pH 5.0, greater fluctuations on the size and PDI values are visible across the studied timepoints, when compared to the liposomes incubated with HEPES pH 7.4, in **figure 31**.

4.3.3.3 Stability with FBS at 37°C

The size, PDI and ζ-potential of the siRNA-loaded liposomes, incubated in 55% FBS, were measured (**figure 33**). For these systems to be applied in the systemic circulation, it is important to teste their stability in an environment that mimics the blood serum.

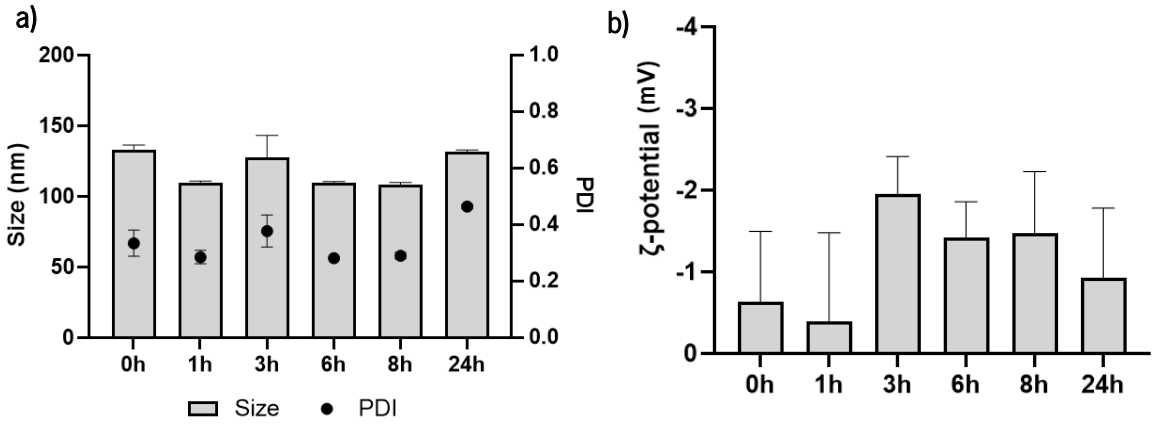


Figure 33. Stability of siRNA-loaded liposomes in FBS at 37°C. (a) Size and PDI. (b) ζ-potential.

As observed in **figure 33a**, the size and ζ-potential of the liposomes incubated in FSB remains stable along the 24h. The PDI, varies, however, probably due to the existence of serum proteins, and protein aggregates, and due to the interaction of the exosome-like liposomes with the proteins, leading to higher PDI values.

4.3.4 Hemolysis of empty exosome-like liposomes

Determination of hemolytic properties *in vitro* is an important assay for preliminary evaluation of the cytotoxicity of the exosome-like liposomes in the blood. Two concentrations of empty exosome-like liposomes were tested (50 and 500 µg/ml). In this assay (**figure 34**) two controls were used: a negative control with PBS (1X) and a positive with Triton (10X),a detergent that lyses the erythrocytes. The results are normalized against the positive control.

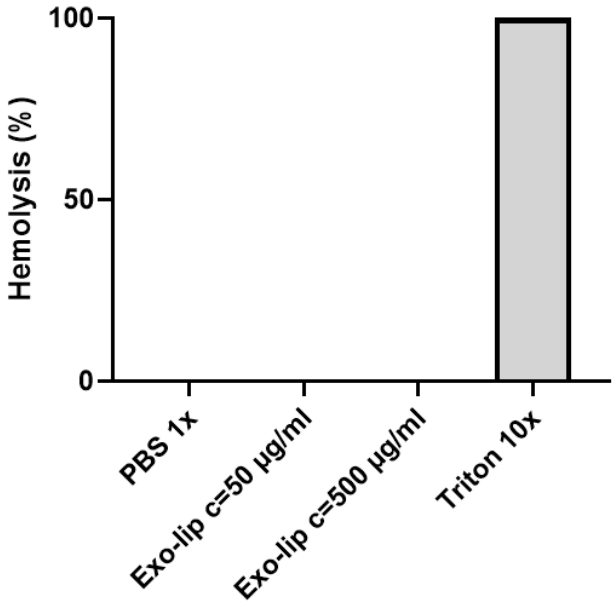


Figure 34. Evaluation of toxicity in erythrocytes incubated with empty exosome-like liposomes.

As observed in the results, the presence of these systems does not induce haemolysis, since no hemoglobin release was detected, when compared to the positive control (Triton 10x). Both concentrations of empty exosome-like liposomes were thus non-toxic for the red blood cells.

4.3.5 Uptake of exosome-like liposomes with siRNA in the HEK293 cell line

The plasma membrane is the first barrier that prevents the entrance of chemical entities, such as exosome-like liposomes, and obstructs their efficient intracellular delivery. Taking this into account, is crucial to study the uptake of these novel delivery systems to understand if they can be internalized by the cells. Additionally, is also important to research how much time it takes for the exosome-like liposomes to be uptaken by the cells.

For this assay, the exosome-like liposomes were stained with Oil Red O at the time of the production and incubated during three different timepoints (1h, 3h, and 4h) in the HEK293 cell line, which is highly transfectable (**figure 35**).

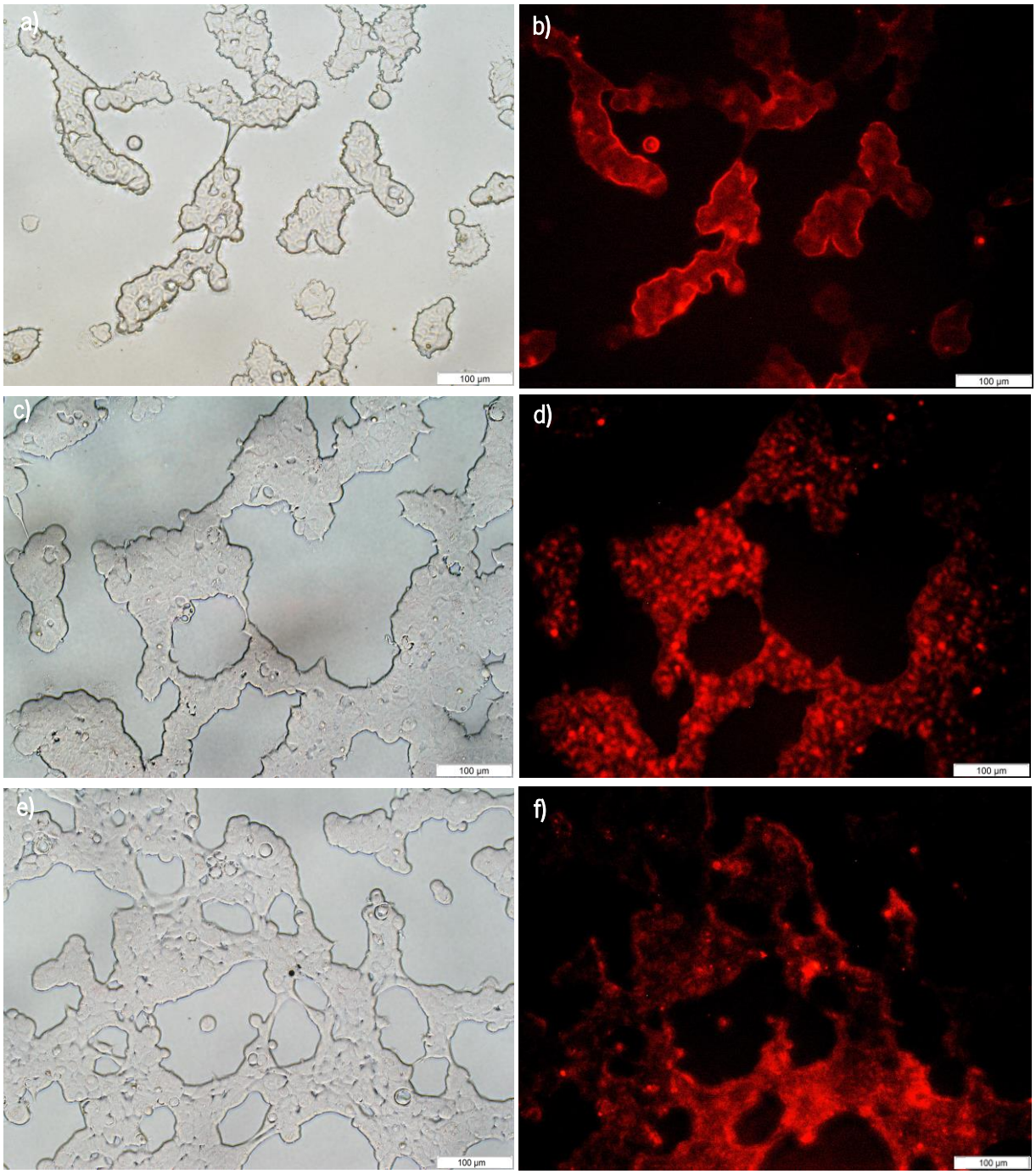


Figure 35. Internalization of exosome-like liposomes with siRNA stained with Oil Red O in 293T cells by microscopy of fluorescence in brightfield at (a) 1h, (c) 3h, (e) 4h and in TRITC filter at (b) 1h, (d) 3h, (f) 4h. Scale bar = 100 µm.

In **figures 35a-b**, corresponding to 1h of incubation, the exosome-like liposomes seem to be entering the cellular membrane, since the particular brighter red fluorescence, from the exosome-like liposomes, is observed in the outer surface of the cells. At 3h after incubation (**figures 35c-d**), the majority of exosome-like liposomes have already been internalized by the cells, and after 4 hours of incubation (figures **35e-f**), we can observe that the entirety of the liposomes have been internalized by the cells.

4.3.6 Transfection of Luciferase mRNA

When transfected with lipofectamine, vehiculating mRNA encoding for the luciferase protein, for 48h, the highly transfectable mammalian cells HEK-293, will express this luminescent protein, which was originally isolated from the firefly (*Photinus pyralis*). This mRNA was used to measure gene expression, since it leads to bioluminescence emission, in successfully transfected cells, in the presence of the substrate, luciferin. The results obtained can be observed in **Table 5**.

Table 5. Luminescence measured in HEK293 cells transfected with Luciferase mRNA using transfecting agent Lipofectamine 2000.

Samples	Luminescence (R.L.U)
Control	222
Lipofectamine + Luciferase mRNA	313

The results obtained are not satisfactory to conclude that uptake and transfection of mRNA was successful, and therefore this protocol has to be perfected before the transfectability of the exosome-like liposomes loaded with the same mRNA can be tested.

4.4 Strategies for the treatment of AD after stablished AD models

Following the validation of the AD model in neuroblastoma cell line and zebrafish embryos, they were used to test promising therapies to counteract the toxicity caused by aluminium chloride, (1) anti-Tau siRNA, (2) anti-Tau siRNA in combination with curcumin and (3) petrosamine. As mentioned previously, RNA requires a delivery system to be effectively delivered. Therefore, anti-Tau siRNA was delivered using the exosome-like liposomes, produced, and described in this work, into the zebrafish AD model. In addition to the anti-Tau siRNA, the combination of this RNA and curcumin, delivered with exosome-like liposomes, was also tested. Finally, petrosamine was tested in the two established AD models, to prove its potent inhibition of AChE activity.

4.4.1 Delivery of loaded anti-Tau siRNA and curcumin exosome-like liposomes *in vitro*

4.4.1.2 LDH activity

A common method for determining cytotoxicity is based on measuring the activity of cytoplasmic enzymes released by damaged cells. LDH is a stable cytoplasmic enzyme that is found in all cells. LDH is rapidly released into the cell culture supernatant when the plasma membrane is damaged, a key feature of cells undergoing apoptosis, necrosis, and other forms of cellular damage[139]. So, the LDH assay was performed to assess the capacity of the exosome-like liposomes loaded with anti-Tau siRNA and curcumin to restore cell viability after the established AD model *in vitro*, that induced AD-like phenotype (**figure 36**). The 200 μM concentration of $AlCl_3$ was the only used is this assay.

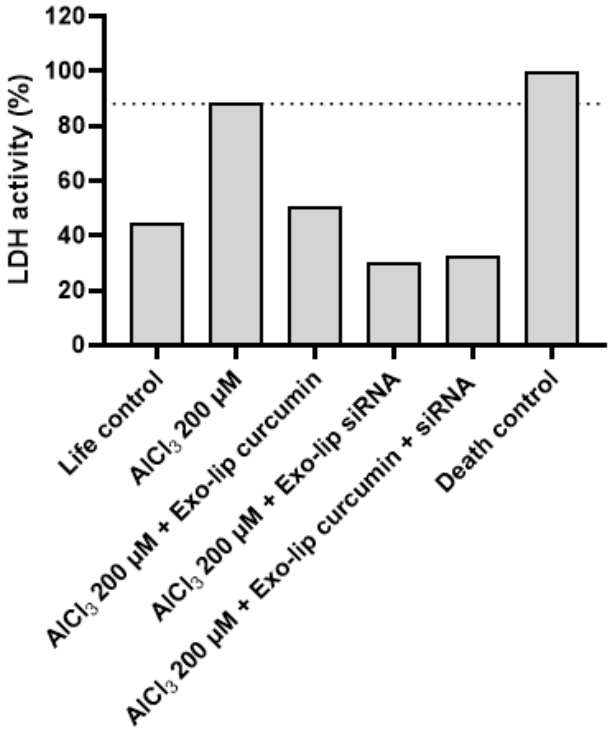


Figure 36. LDH activity (**1n**) after SH-SY5Y cell's exposure to 200 μM for 24h and further treatment with loaded exosome-like liposomes anti-Tau siRNA and curcumin for 24h.

As shown in **figure 36**, $AlCl_3$ compromises the cell membrane, leading to cellular damage. However, after applied the exosome-like liposomes loaded with anti-Tau siRNA and curcumin was verified an approximately decrease of 55% in the LDH activity, having a great impact in the restoration of cell viability.

4.4.1.2 RT-PCR

Real-Time Reverse Transcription PCR (RT-PCR) is a major development of PCR technology that enables reliable detection and measurement of products generated during each cycle of PCR process. The combination therapy of exosome-like liposomes with anti-Tau siRNA and curcumin was tested by RT-PCR to verify if these systems could decrease the fold change in Tau expression in SH-SY5Y cells, after induced neurotoxicity by 200 μM of $AlCl_3$ (**figure 37**).

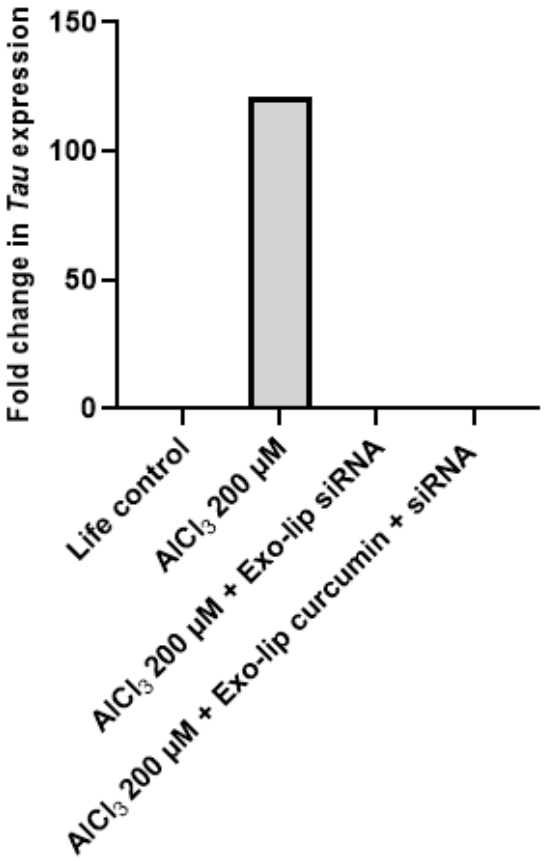


Figure 37. Fold change expression of Tau gene in SH-SY5Y cells exposed to $AlCl_3$ at 200 μM with a posterior incubation with exosome-like liposomes with anti-tau siRNA and curcumin.

As verified in **figure 37**, comparing the levels of expression of Tau in the induced neurotoxicity conditions with 200 μM of $AlCl_3$, we could verify that the levels of expression are much lower when the cells were incubated with exosome-like liposomes, leading back to a value equal to the control.

4.4.2 Delivery of loaded anti-Tau siRNA and curcumin exosome-like liposomes *in vivo*

4.4.2.1 Cardiac Frequency

As demonstrated previously, the cardiac frequency is a phenotypic parameter highly affected by $AlCl_3$ toxicity, so the evaluation of this parameter was important to study the possible effect of anti-Tau siRNA and curcumin against AD-like toxicity. The zebrafish embryos were submitted to 50 and 200 μM $AlCl_3$ exposure until 72 hpf and at this timepoint the embryos were incubated with the therapeutical exosome-like liposomes until 120 hpf (**figure 38**). The figure does not include the cardiac frequency at 24 hpf since the embryos were not fully developed.

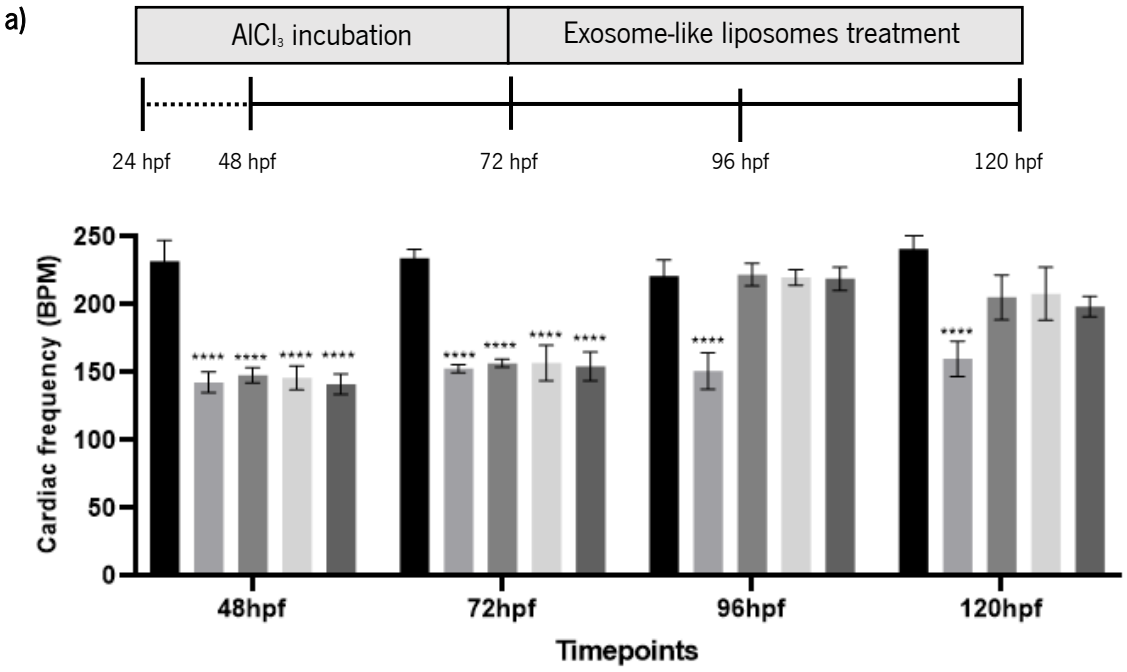


Figure 38. Cardiac frequency of zebrafish at 48, 72, 96 and 120 hpf. The embryos were submitted to (a) $AlCl_3$ 50 μM and to (b) $AlCl_3$ 200 μM the first 72 hpf and then treated with loaded exosome-like liposomes anti-Tau siRNA and curcumin until 120 hpf. Verified a significant difference among means. ** $p < 0.01$, **** $p < 0.0001$ as compared to the control.

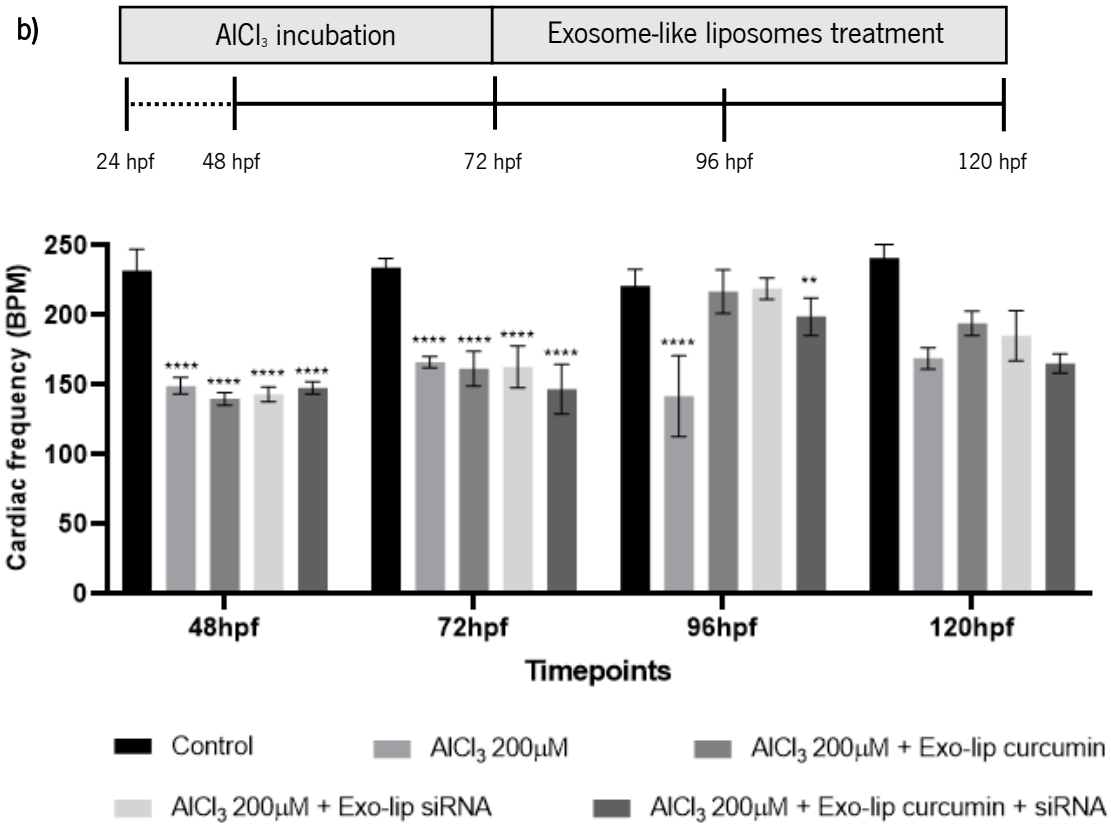


Figure 38. *Cont.*

In **figure 38a**, an extreme decrease in cardiac frequency, around 150 BPM until 120 hpf, is noticeable when the embryos were submitted to 50 µM of $AlCl_3$. However, when the embryos are treated with the exosome-like liposomes loaded with the therapy, we could see a restoration of the cardiac frequency to levels similar to those of the control. In this case, the anti-Tau siRNA loaded liposomes seem to be the system that better counteract the $AlCl_3$ toxicity at a cardiac level, where the cardiac frequency is restored from 156 BPM to 222 BPM, at 96 hpf.

In **figure 38b**, a massive decrease in the cardiac frequency is also observed when embryos are submitted to 200 µM $AlCl_3$. At 96 hpf after the treatment was applied, a high increase in the cardiac frequency, to levels almost equal to those of the control was verified. In this case, anti-Tau siRNA loaded liposomes, in conjuncture with curcumin loaded liposomes seem to be the best treatment to counteract the $AlCl_3$ toxicity, at a cardiac level.

4.4.2.2 Measurement of AChE activity

The measurement of the AChE activity is a crucial assay to be evaluated the potential of curcumin and anti-Tau siRNA loaded exosome-like liposomes in the treatment of $AlCl_3$ induced neurotoxicity (**figure 39**).

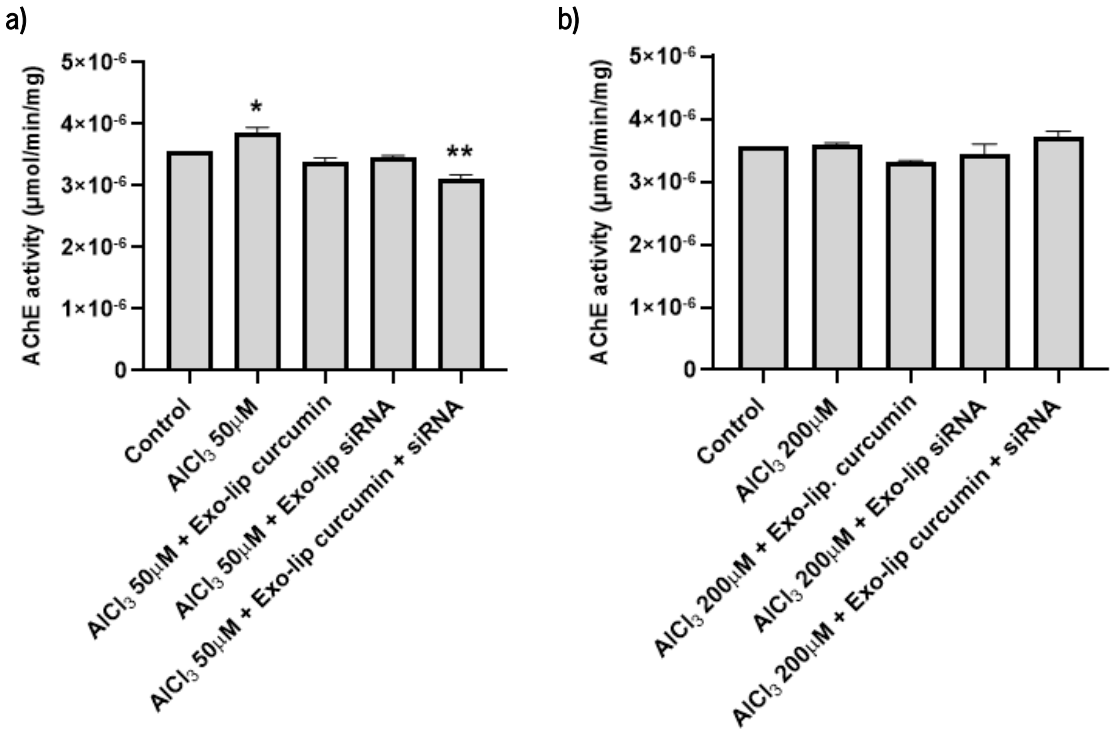


Figure 39. AChE activity of zebrafish submitted to (a) $AlCl_3$ 50 µM and to (b) $AlCl_3$ 200 µM the first 72 hpf and then treated with loaded exosome-like liposomes anti-Tau siRNA and curcumin until 120 hpf. Verified a significant difference among means. * $p < 0.05$ and ** $p < 0.01$.

As stated before, for the establishment of the zebrafish embryos AD model, only the concentration of 50 µM of $AlCl_3$ promoted a similar hallmark to AD, regarding the activity of AChE.

The results presented in **figure 39**, corroborate the results obtained previously. In **figure 39a**, a statistical significant difference was only observed when the embryos were submitted to 50 µM of $AlCl_3$, with the activity of AChE increasing in this condition. However, when the embryos were treated with both curcumin and anti-Tau siRNA loaded exosome-like liposomes, a decrease of 20% in the AChE activity is observed. This is indicative that this treatment is effective against this AD hallmark, as it prompted a reduction in the AChE activity to levels lower than those of the control.

The results presented in **figure 39b** indicate, once again, that the 200 μM of $AlCl_3$ concentration is not effective for the establishment of the AD model, regarding AChE activity, as it leads to activity levels similar to those of the control, and consequently no differences can be inferred from the tested treatments.

4.4.3 Petrosamine as a promising therapy for AD

4.4.3.1 Biocompatibility of Petrosamine

Firstly, to evaluate the biocompatibility of petrosamine a was performed a cell viability assay in the neuroblastoma cell line SH-SY5Y (**figure 40a**), was tested the survival rate of the zebrafish embryos (**figure 40b**) and performed the haemolysis assay (**figure 40c**) with four different concentrations was performed.

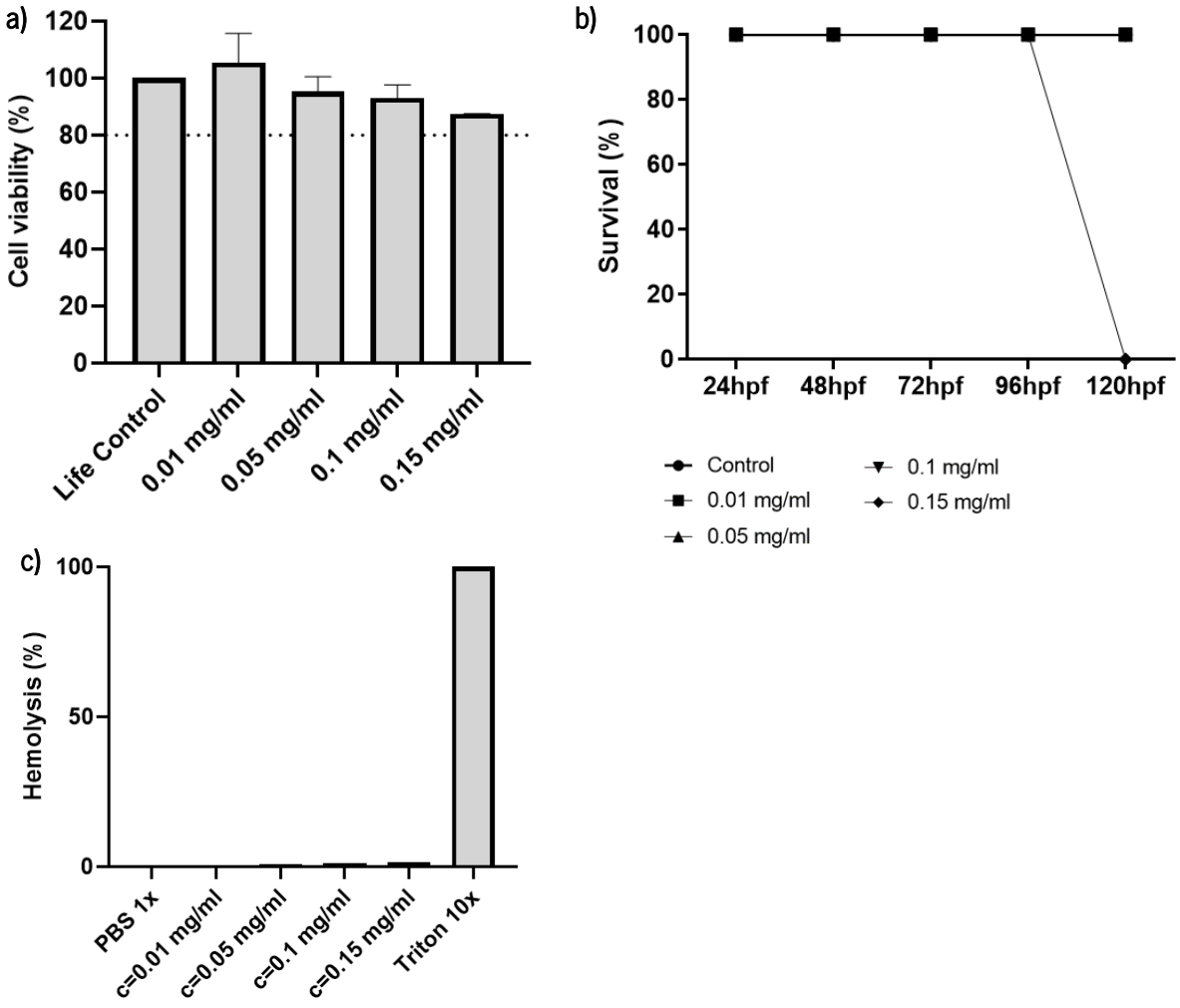


Figure 40. Biocompatibility of petrosamine. (a) Resazurin assay; (b) Survival rate of zebrafish embryos; and (c) Hemolysis assay.

As observed in **figure 40**, the petrosamine is biocompatible in the concentrations tested, as it did not induce any loss of cell viability, and was safe for the zebrafish embryos, during the entirety of the 120 hpf, since it did not influence their survival rate and caused no hemolysis.

4.4.3.2 Effect of petrosamine in the established AD model *in vitro*

The influence of petrosamine (c= 0.5 mg/ml) on the AChE activity was tested in the SH-SY5Y neuroblastoma cell line, after its establishment as an AD model (**figure 41**).

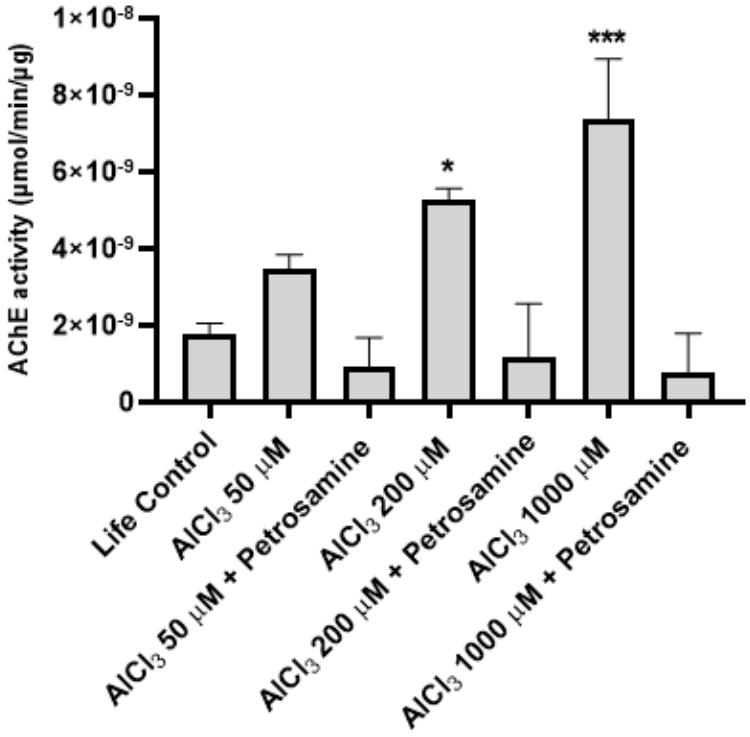


Figure 41: AChE activity (**3n**) after SH-SY5Y cell's exposure to three different concentrations of $AlCl_3$ (50 µM, 200 µM, and 1000 µM) for 24h and then treated with petrosamine (c= 0.05 mg/ml) for 24h. Verified a significant difference among means. * $p < 0.05$, *** $p < 0.001$ as compared to negative control.

In **figure 41**, it is visible that when petrosamine was administered to the cells, there is a decrease in AChE activity of 27.2%, 78.0% and 89.5% in the AChE activity, compared to the levels seen in cells treated with 50, 200 and 1000 µM of $AlCl_3$, respectively. These values of AChE activity are lower than the

control, which indicates that petrosamine is inducing a strong effect in the reduction of this enzyme's activity.

The effect of petrosamine against the lipid peroxidation was also evaluated (**figure 42**).

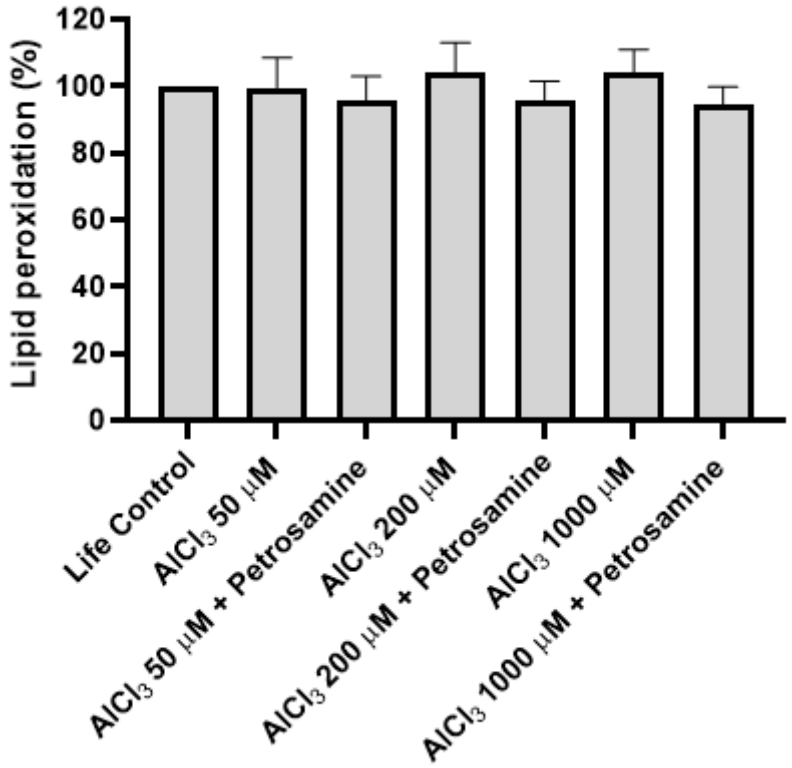


Figure 42. Lipid peroxidation percentage (**3n**) after SH-SY5Y cell's exposure to three different concentrations of $AlCl_3$ (50 µM, 200 µM, and 1000 µM) for 24h and then treated with petrosamine (c= 0.05 mg/ml) for 24h. The results were expressed in relation to negative control (100%). Not verified a significant difference among means.

As it can be observed in the figure, petrosamine has a tendency to decrease the lipid peroxidation levels, yet not to statistically significant levels.

4.4.3.3 Effect of petrosamine in AD model *in vivo*

To evaluate the potential of petrosamine in the AD model of zebrafish embryos, the FET assay was conducted. The survival and hatching rate are presented in **figure 43**, the yolk volume in **figure 44** and the cardiac frequency in **figure 45**. Additionally, the AChE activity levels are shown in **figure 46**.

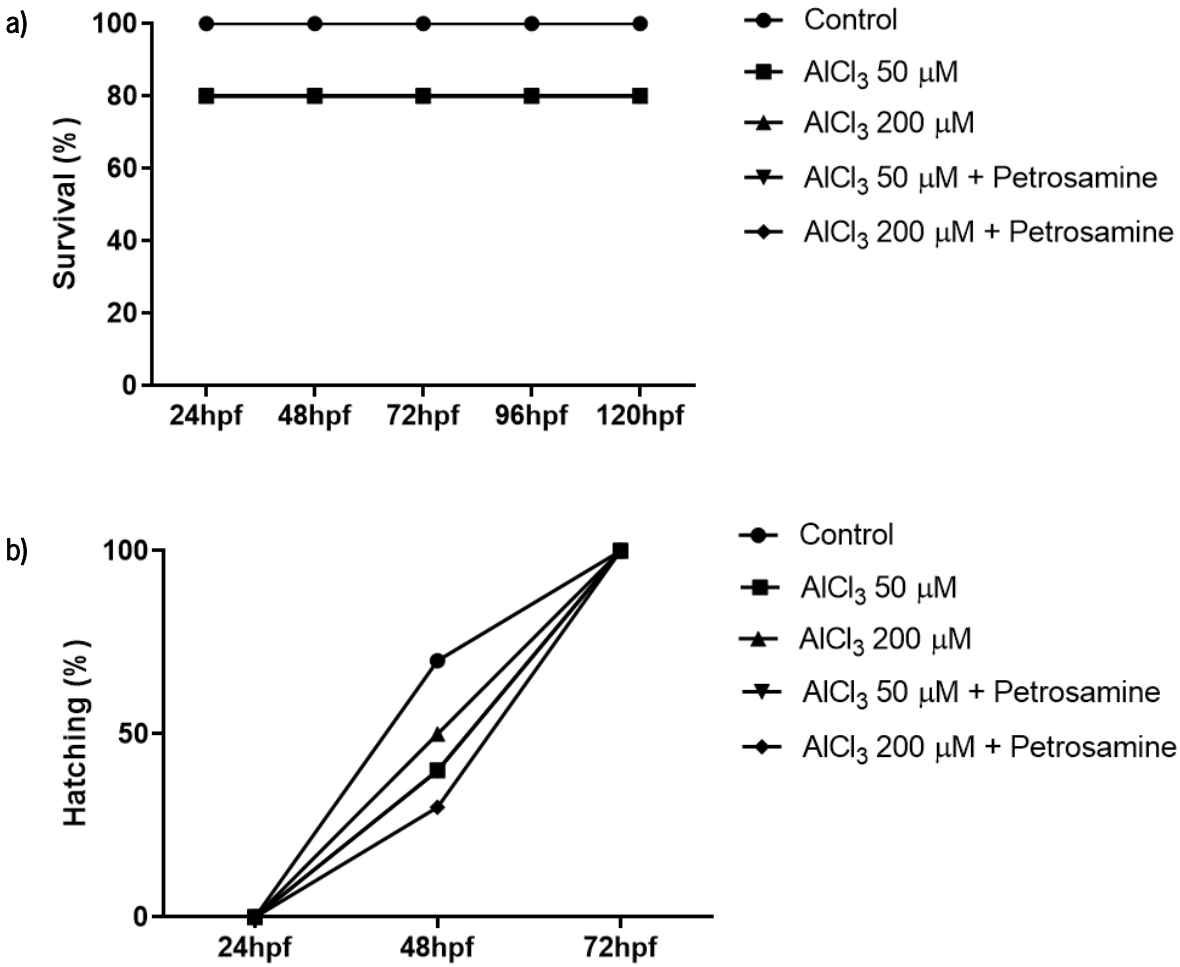


Figure 43: Analysis of zebrafish embryos development: (a) survival rate and (b) hatching rate.

As it can be observed in **figure 43a**, the survival rate of all of the conditions, except for the control, decreased to 80% in the first 24 hpf when the zebrafish embryos were exposed to $AlCl_3$. Also, in **figure 43b**, the embryos exposed to both concentrations of $AlCl_3$, were with a delayed hatching rate. This figure confirms the previous results obtained in the validation of the AD model in the zebrafish embryos, in which $AlCl_3$ lead to a decrease in the survival rate and a delay in the hatching rate. The survival and hatching rate are only affected by the toxicity of $AlCl_3$, and not by petrosamine, when applied at 72 hpf.

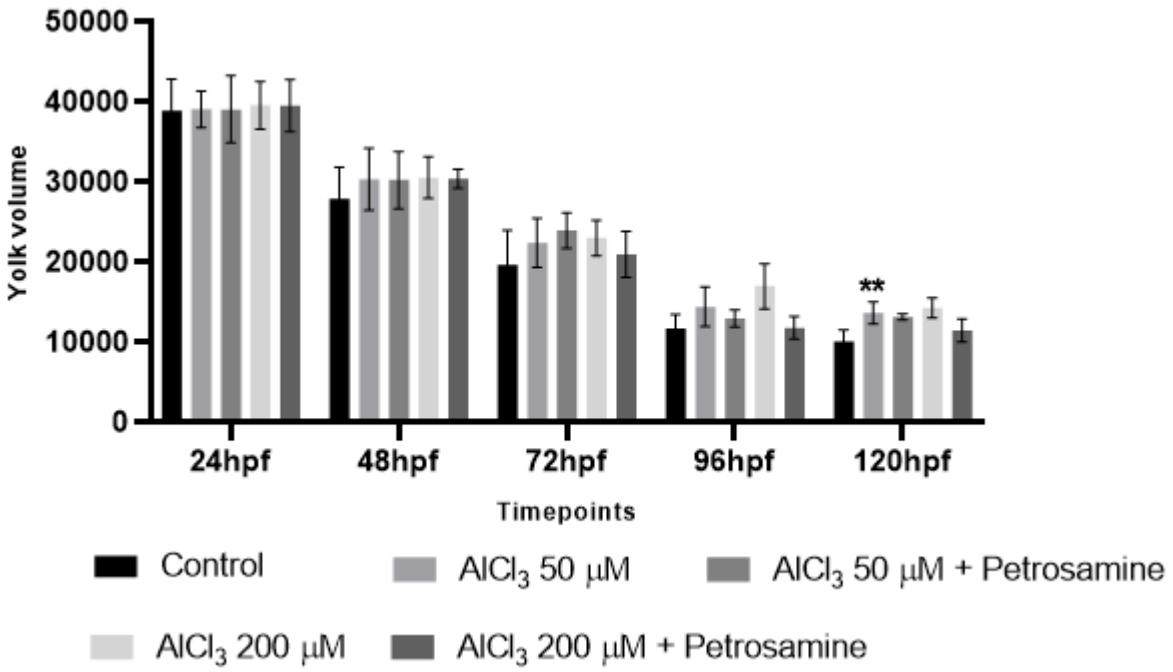


Figure 44: Effect of petrosamine after aluminium toxicity in zebrafish embryos yolk volume during 120 hpf.

Petrosamine had a positive effect in the yolk volume at 96 hpf and 120 hpf, since a decrease of the volume of the yolk was observed, which indicates that this marine compound is helping in the development of the zebrafish after ACl_3 neurotoxicity induction.

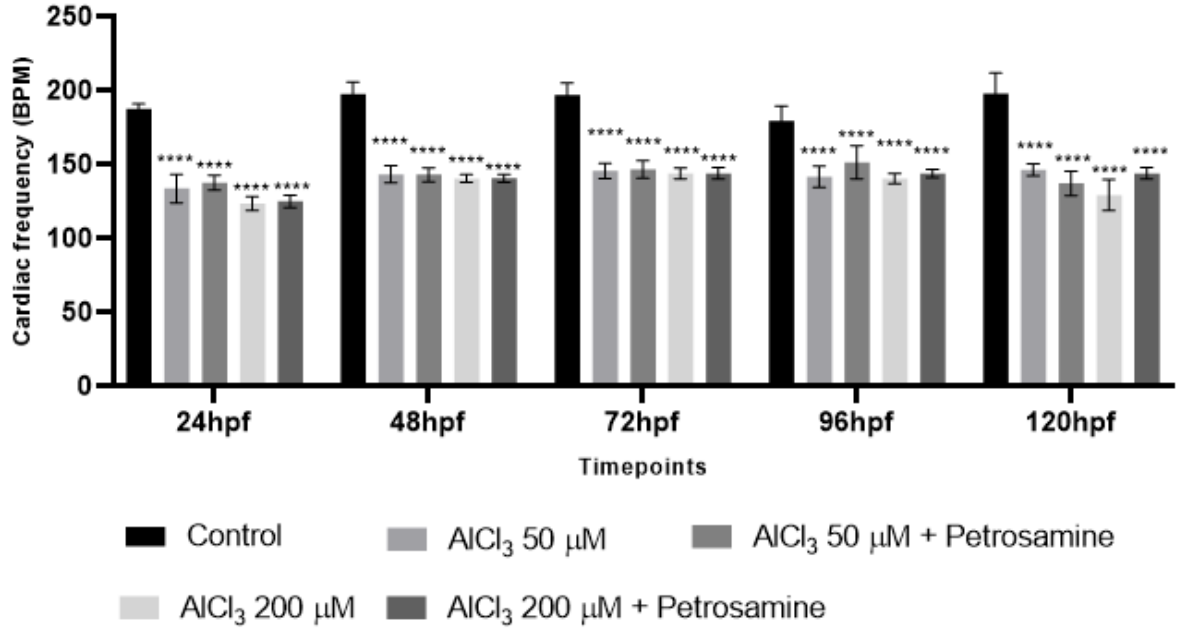


Figure 45: Effect of petrosamine after aluminium toxicity in zebrafish embryos cardiac frequency during 120 hpf.

In this case, petrosamine did not seem to induce a positive effect on the cardiac frequency after the embryos were induced with AD-like toxicity.

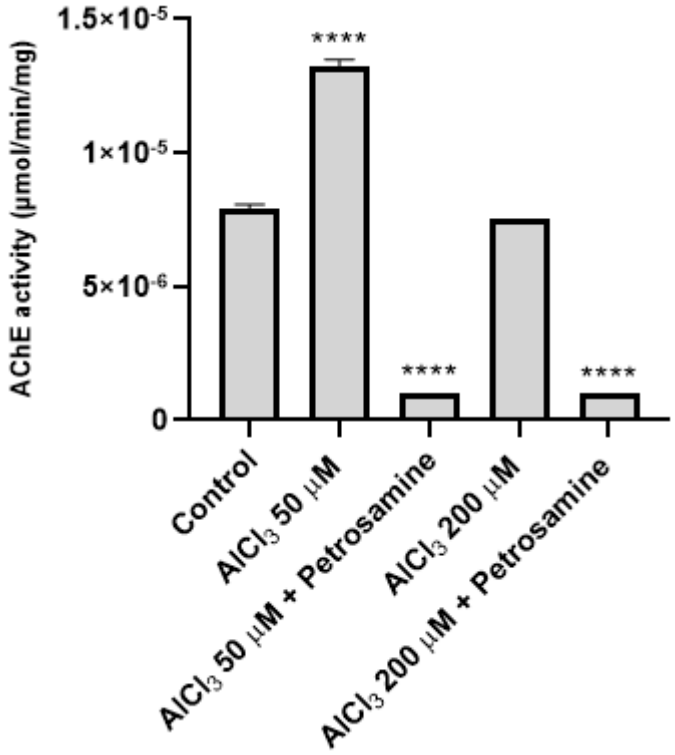


Figure 46: AChE activity of zebrafish embryos after exposure to two concentrations of $AlCl_3$ (50 and 200 µM) until 72 hpf, and then treated with petrosamine (c= 0.05 mg/ml), until 120 hpf. A significant difference among means was verified.**** $p < 0.0001$ as compared to negative control.

In the results regarding the AChE activity (**figure 46**), an increase in activity, relative to the control, is seen when the embryos are treated with 50 µM of $AlCl_3$. This activity is then lowered by a statistically significant margin (90.8%), when petrosamine is added to the treatment of the embryos.

Embryo incubation with 200 µM of $AlCl_3$ did not affect the AChE activity, as seen in other experiments, however, when the petrosamine is added to the treatment, a substantial decrease in AChE activity is also verified.

Chapter 5

Discussion

5. Discussion

In this thesis, two AD models, one based on a neuroblastoma cell line SH-SY5Y and the other on zebrafish embryos, were developed by treatment with $AlCl_3$. Alu is a well-established neurotoxin that adversely impacts several biological functions in the CNS and is suspected to be linked with AD pathogenesis. Accordingly, in this thesis was took advantage of the $AlCl_3$ neurotoxic properties to create a similar phenotype to AD. For the establishment of the AD model in the neuroblastoma cell line, the cells were incubated with $AlCl_3$ at three different concentrations (50 μM, 200 μM and 1000 μM). The results of the cytotoxicity evaluation with resazurin showed that all concentrations of $AlCl_3$ affected cell viability. A direct correlation between the increasing concentration of $AlCl_3$ and the decrease of cell viability was observed. The concentration of 200 μM reduced the cell viability to 75.3%, values very similar to those seen by Rizvi *et al,* that conducted a similar study (MTT assay) with 200 μM $Al(mal)_3$ (74.5% cell viability)[140]. Finally, the concentration of 1000 μM led to significant loss of cell viability, comparable to the cell viability seen for the death control. To corroborate these results, two other assays were completed: the SRB, that provides information about cell proliferation and AO/PI assays that measure cell apoptosis. These two methods supported that the concentration of 50 μM of $AlCl_3$ led to a minor difference in cell viability, while the AO/PI assay revealed that the concentration of 1000 μM of $AlCl_3$ led to a substantial percentage of apoptotic cells. Yang *et al.* have shown that the exposure of SH-SY5Y cells to concentrations of aluminium ions lower than 100 μM does not cause a significant decrease in cell viability and proliferation[141], which is consistent with the results obtained in this thesis.

Neurons are very sensitive to oxidative stress, which is the primary event in any neurological disorder[142]. Hence, the DCFDA assay was performed, as it is an important method to determine ROS accumulation. We observed that $AlCl_3$ caused redox imbalance in neuronal cells as evidenced by a significant rise in ROS at all concentrations. The higher levels of ROS were observed with incubation with1000 μM $AlCl_3$, which is in accordance with the previous cell viability results. With this concentration, we deduce that the excessive levels of ROS, that are majorly produced in mitochondria, lead to an impaired mitochondrial function, which is corroborated by the cells inability to metabolize resazurin, ultimately leading to loss of cell viability. Rizvi *et al.* verified a maximum ROS level at concentrations higher than 500 μM with $Al(mal)_3$ in the same neuroblastoma cell line[140], which is comparable to the results we have obtained. Furthermore, an excess of ROS induces lipid peroxidation, via enzymatic and nonenzymatic pathways, leading to cell death.[143] Peroxidation of membrane lipids may be one of the

mechanisms by which ROS contributes to the cascade of events leading to damage of cell membrane and also can induce peroxidation of myelin lipids[47,143]. In this context, the DCFDA results, were further supported by the TBARS assay, where higher levels of MDA, a product of lipid peroxidation, were detected when the cells were submitted to $AlCl_3$ toxicity.

Another fundamental assay performed was the measurement of AChE activity. The AChE activity increases with higher concentrations of $AlCl_3$, which indicates that this metal causes a higher activity of this enzyme, and ultimately can lead to an impaired synaptic function. The activity of AChE of the neuroblastoma cell line, under the effect of $AlCl_3$, has not yet been described in the literature, making these results important for this field of research, and to validate the *in vitro* model. It is nevertheless acknowledged, in the literature, that Alu can lead to a higher activity of AChE, influences acetyl-CoA and inhibits acetylcholine release[47], which agree with the results we obtained. The results relative to the establishment of an AD model in the neuroblastoma cell line, revealed that $AlCl_3$ induced cytotoxicity in a dose-dependent manner, and led to AD-like neurotoxicity.

Having established an *in vitro* neuroblastoma AD model, we proceeded with the establishment of the AD model *in vivo*, in zebrafish embryos via treatment with 50 μM and 200 μM of $AlCl_3$. In this study, we observed significant changes in phenotypic parameters, apoptosis, lipid peroxidation and AChE activity in zebrafish embryos exposed to sublethal levels of aluminium chloride (50 and 200 μM). Survival curves showed that both concentrations of $AlCl_3$ lead to death and decreased hatching rate. $AlCl_3$ induced major sub-lethal phenotypic alterations such as pericardial edema, and impaired cardiac function, being that alterations on heart rate were observed. These results are in accordance with Monaco *et al.*, which verified that $AlCl_3$ affected embryo viability, induced phenotypic modifications, inclusively pericardial edema, and reduced cardiac frequency[104].

Epiboly was also altered, indicating that the expansion of the embryo surface during the initial development was disturbed. Another phenotypic parameter influenced by Alu was the yolk volume. In this case, we observed that aluminium toxicity was higher in the larval stages than in the embryo stages. This occurs probably due to the absence of the chorion in larvae, which in the early stage of development exerts a good protection for the embryo.

Apoptosis levels were studied in the zebrafish larvae, with acridine orange, and a mosaic of apoptotic cells in the larvae head was observed. The lateral line is a sensory system used by aquatic animals to detect water flow. This morphological structure is modulated by efferent neurons located in

the brain and contain numerous sensory neuromasts[138]. Neuromasts are clusters of superficial hair cells, allowing fish to sense mechanical changes in water, playing a crucial role in behaviours such as rheotaxis, predator avoidance, and schooling[138]. The apoptotic cells detected seem to be neuromasts, according to the pattern of green spots observed. Additionally, the total fluorescence intensity in the concentration of 50 μM is much higher than the concentration of 200 μM, which is similar to that of the control. This indicates that the larvae exposed to 50 μM of $AlCl_3$ have several apoptotic cells in the neuromasts, which can suggest that the detection of water movement in these 5-day old larvae is ineffective. Capriello *et al.* concluded the same, in a study in which they evaluated apoptosis levels in zebrafish embryos treated with $AlCl_3$ (50, 100 and 200 μM). They verified an increase in apoptosis in the head and tail in the larvae exposed to the lowest concentration (50 μM), while those exposed to higher doses exhibited a decrease in the number of apoptotic cells. Also, they tested the larvae motility and concluded that motility drastically decreased in embryos exposed to 50 μM $AlCl_3$, but tended to increase in larvae exposed to high concentrations[111]. This is in good agreement with our results, where 50 μM of $AlCl_3$ lead to apoptosis in neuromasts.

The assessment of lipid peroxidation, by the TBARS assay, showed an increased in this parameter, with the increase of $AlCl_3$ concentration, which could be due to the inactivation of some antioxidant enzymes, due to conformational changes induced by $AlCl_3$[144]. The AChE activity was also determined and, once again, the activity of this enzyme was only affected by the concentration of 50 μM of $AlCl_3$. The conjecture of these results clearly points to a neurotoxic effect promoted by Alu. However, the mechanisms by which aluminium interacts with the nervous system are still only partly understood.

Gene therapy, namely gene therapy mediated through the use of siRNA or mRNA can be a promising strategy for the treatment of AD. One major obstacle to the wide application of this type of therapy, is the delivery of these molecules into the brain, due to the selectivity of the BBB. Nanoparticles, namely exosome-like liposomes, may aid in overcoming this limitation, due to their advantages, that include their high biocompatibility, capacity to incorporate hydrophilic molecules, such as nucleic acids and their lipidic composition that increases the chance for these systems to fuse with the endothelial cells of the BBB. Delivery systems must have several requirements for a successful delivery of the therapeutic agent: (1) have a desired size and PDI for the delivery purpose; (2) be loaded with a sufficient amount of drug, in order to promote a therapeutic response; (3) be stable in the blood stream until they reach their cellular target (by retaining their structure and cargo); (4) avoid the endosomal pathway; (5) be capable of being internalized by cells, and (5) be biocompatible[98].

In this thesis, exosome-like liposomes were produced to exploit their promising properties as a novel delivery system of siRNA or mRNA, for the treatment of AD. The size of exosome-like liposomes loaded with siRNA was 145.8 nm, and these nanoparticles had a PDI of 0.207, and the exosome-like liposomes loaded with mRNA had a size of 149.1 nm and a PDI of 0.224. The physico-chemical properties of these two liposomes were very similar, being the only difference between them the type of RNA encapsulated, which have very different lengths (21 bp vs ≈2000 bp). The size of exosome-like liposomes proved that these systems are compatible with intravenous application, since their size is inferior to 200 nm[102].

Additionally, a PDI of approximately 0.2 indicates that the liposomes are constituted by a homogenous (monodisperse) population of a certain size[121]. Hattori *et al.* produced siRNA-loaded liposomes, by the ethanolic injection method, with a similar composition to our system, and observed also a particulate size of 149.7 nm and a PDI of 0.200[145]. Lechanteur *et al.* also produced siRNA-loaded liposomes with an average size of 170.0 nm and a PDI lower than 0.2, while *Ji et* al. prepared a lipidic formulation of mRNA-liposomes, by the ethanolic-injection method, and obtained a size of 90.15 nm and a PDI of 0.210[146], although the formulation used in the work is not exactly the same as in the production of exosome-like liposomes. The percentage of each lipid in the formulation is not similar to the ones we used, which can explain the smaller size they achieved. Moreover, the ethanolic injection is a method highly dependent on the producer. Finally, Tang *et al.* produced mRNA lipoplexes by the ethanol injection method, and obtained a size in a higher range (284-313 nm) and a PDI between 0.150-0.250[147]. Considering the obtained physical-chemical properties of the exosome-like liposomes combined with previous studies, where we can observe in zebrafish embryos that these systems mostly concentrate in the areas containing higher lipid content[102], such as the brain probably due to its lipophilic nature, it is likely that exosome-like liposomes cross the BBB.

The exosome-like liposomes produced in this thesis, were highly effective encapsulating mRNA, with an encapsulation efficiency of 100%, an efficiency higher than that reported by . Ji *et al.*, who obtained a mRNA encapsulation efficiency of 93.40%[146].

An important factor that affects RNA release is the stability of liposomes in biological environments, and, hence they were tested in HEPES pH 7.4 HEPES pH 5.0 and FBS, at 37°C for 24h, to mimic the physiological conditions. HEPES pH 7.4 at 37°C was used to simulate pH and temperature of the circulatory system and HEPES pH 5.0 at 37°C to mimic the endocytosis pathway. When endocytosis occurs, the early endosomal compartment matures into a late endosome and ultimately

accumulates in the lysosome. In this process, the pH in the lysosome decreases from 7.4 to 5.0[148]. FBS at 37°C was used, as it resembles the blood serum, to infer the interaction of its constituting proteins with the liposomes. Overall, in the three different conditions, the size, PDI and surface charge was not drastically altered during the 24h incubation period. More importantly, the size of the exosome-like liposomes did not increase significantly. In case the size of this systems had increased considerably, it could have promoted leakage of their RNA content, with an impact on their cellular uptake, cytotoxicity and in tissue distribution. Shao *et al.* tested the liposome stability at pH 5.0 and pH 7.4 and verified similar results to those presented in this thesis, with no substantial changes in hydrodynamic size within the 72h of incubation, indicating that are highly stable[126]. The biocompatibility of these exosome-like liposomes was studied by testing their hemolysis in pig erythrocytes, an important parameter as these systems are designed to be administered via intravenous injection. In the hemolysis assay, the empty exosome-like liposomes have shown to be highly biocompatible, both at low (50 μg/ml) and high concentration (500 μg/ml). Fernade*s et al.* produced the exact same formulation of exosome-like liposomes, although encapsulating curcumin[102] instead of RNA, and verified no hemolytic activity, which is in accordance with the results we obtained.

The next step was to evaluate the cellular uptake of the liposomes in the HEK293 cell line at 1h, 3h and 4h. The exosome-like liposomes, stained with Oil Red O, are partially internalized after 1h and totally internalized after 3h-4h of incubation, which is in agreement with Zaremba-Czogalla *et al.*, who demonstrated, by fluorescence microscopy, that liposomes labelled with Nile Red were effectively internalized by BxPC-3 cell line, after 2h of incubation[149]. Additionally, one aim in this thesis was to observe the expression of the Luciferase protein by cell transfection with Luciferase encoding mRNA. However, this assay will have to be further optimized since the transfection of this mRNA in the HEK293 cell line with the commercial reagent Lipofectamine did not allow successful detection of luminescence.

In recent years, other nanocarriers for RNA delivery have been developed for AD therapy. Tanaka *et al.*, have developed lipid nanoparticles for mRNA delivery to brain neuronal cells to observe protein expression[150]. These NPs are composed of SS-cleavable proton-activated lipid-like material that becomes positively charged by the protonation of tertiary amines as the environment becomes acidic during endosome maturation, to promote endosomal escape. They verified that the mRNA-loaded NPs were capable to induce the production of exogenous proteins in neuronal cells and in astrocytes[150]. Also, Rassu *et al.*, designed chitosan-coated solid lipid nanoparticles composed by a short peptide derived from rabies virus glycoprotein known as RVG-9R, to increase the transcellular pathway in neuronal cells and deliver

BACE1 siRNA, useful in the treatment of AD[151]. However, the delivery of gene therapies, by nanocarriers, for AD treatment is still underexplored, making this study successful in validating this new concept of safe and effective liposomal carriers for RNA therapy of AD.

After the establishment of the two AD models and after the characterization of the exosome-like liposomes, a study with these delivery systems, loaded with anti-Tau siRNA and curcumin, was conducted to see if they could counteract the toxicity induced by the Alu in the two validated AD models. The exosome-like liposomes loaded with anti-Tau siRNA and curcumin were capable to restore cell viability and led to a high decrease in the fold change of Tau expression after the cells were exposed to an AD-like phenotype, showing great promising results in the treatment of this disease. Two of the main parameters highly affected by $AlCl_3$ in the zebrafish embryos were the reduced cardiac frequency and the increased AChE activity, so we focused on these two assays. Once again, we observed a drastic decrease in the cardiac frequency of the embryos when submitted to both concentrations of $AlCl_3$. However, when the delivery systems were applied at 72 hpf, the cardiac frequency recovered to values similar to those of the control. It has been reported that treatment with Alu induces Tau and Aβ protein accumulation[152]. Consequently, as the embryos were submitted to $AlCl_3$ for 72 hpf, it is likely that these animals have developed an accumulation of Tau protein, that is related to other harmful hallmarks, such as inflammation, and oxidative stress, leading to a vicious cycle. When the exosome-like liposomes, loaded with siRNA targeting this protein, were administered, they promoted a reduction of the Tau levels, leading to an offset of the $AlCl_3$ toxicity, that is verified by the stabilization of the cardiac frequency. Afterwards, the AChE activity of zebrafish embryos submitted to both concentrations of $AlCl_3$, and then treated with the aforementioned systems, was measured. We focused on the 50 μM concentration, which is the concentration that better mimics the AChE activity in the AD model. The results show that the AChE activity is increased in embryos that were submitted only to 50 μM of $AlCl_3$ treatment. However, when the exosome-like liposomes, loaded with anti-Tau siRNA and curcumin, are added to the treatment of the embryos, at 72 hpf, a distinct decrease in AChE activity is observed, leading to a lower levels of AChE activity than those seen for the control. These results prove that the combination of curcumin with anti-Tau siRNA, delivered by exosome-like liposomes, are highly effective in reducing AChE activity in AD-like toxicity. The addition of curcumin, a powerful antioxidant[67], to the anti-Tau siRNA therapy can attenuate the oxidative stress and the cycle of hallmarks triggered by $AlCl_3$. Akinyemi *et al.* performed a study in cadmium-treated rats to evaluate the effect of curcumin on AChE activity[153]. Cadmium is a metal that, similarly to Alu, can accumulate in the brain by crossing the BBB, leading to NDDs. Curcumin was

administered to the rats, after they were treated with cadmium, and it was verified that curcumin inhibited the AChE activity in a dose-dependent manner[153].

This result is in line with our study, as we have also seen an anti-acetylcholinesterase activity promoted by curcumin and anti-Tau siRNA, encapsulated in exosome-like liposomes. It has been also described that abnormal AChE expression in the AD brain occurs in association with NFTs, an accumulation of Tau proteins[12]. This can be an explanation as to why the combination of curcumin with the siRNA targeting Tau decreased the AChE activity, in our zebrafish AD model.

Petrosamine is a potent AChE inhibitor[65] never tested *in vitro* and *in vivo* and never studied in an AD model to evaluate its potential to inhibit the activity of AChE, a hallmark of AD. The tested petrosamine showed biocompatibility, as it did not induce hemolysis in pig erythrocytes, and was non-toxic to zebrafish embryos, once a 100% survival rate was observed in embryos exposed to 5 mg/ml of petrosamine. Petrosamine (c= 0,5 mg/ml) was also evaluated in the established neuroblastoma AD model. After the cells were incubated with different concentrations of $AlCl_3$ (50, 200 and 1000 μM), the AChE activity increased. Afterwards, the administration of petrosamine induced an extreme reduction, to values below those of the negative control, in AChE activity in all test conditions. It is important to highlight the positive impact that petrosamine exerted in the condition of 1000 μM of $AlCl_3$, in which the AChE activity decreased 89.5% when it was added. In order to find more effects of this compound against aluminium-induced AD-like toxicity, the TBARS assay was also performed, as to evaluate its effect on lipid peroxidation. However, this compound did not induce significant differences in MDA levels, which is indicative that this compound may not have a substantial effect in lipid peroxidation. To study the effect of petrosamine in the AD model of the zebrafish embryos, a FET assay was performed, to evaluate the survival and hatching rate, the yolk volume and the cardiac frequency of the embryos, followed by AChE activity and lipid peroxidation assays with 120 hpf embryos. In terms of survival rate, it was observed that the embryos exposed to $AlCl_3$ lost 20% of viability at 24 hpf and had a delayed hatching rate, as corroborated by the results obtained during the implementation of the AD model. Petrosamine had a positive effect when it was added at 72 hpf, since the yolk volume decreased at 96 and 120 hpf, reversing the delayed development seen for both concentrations of $AlCl_3$. Regarding the cardiac frequency, a slight difference was verified, and only at 120 hpf. As seen for the *in vitro* experiments, petrosamine had, once again, a great impact in the embryo's AChE activity, decreasing its activity after aluminium-induced toxicity. These results represent the first ever tentative to study the potential of petrosamine in AD therapy, and indicate its great promise in this field, especially as an AChE inhibitor.

Chapter 6

Conclusion and Future Perspectives

6. Conclusion and Future Perspectives

AD is a neurological disease that remains a public health challenge and still lacks effective treatments. One of the challenges of AD is to create models that best reproduce this pathology in order to evaluate promising disease-modifying therapeutics. Aluminium chloride is a neurotoxin with great potential to induce AD-like toxicity, when using the right concentrations. The first AD model proposed in this thesis, was the human neuroblastoma cell line SH-SY5Y treated with three concentrations of $AlCl_3$. Our study proved that exposure to aluminium affected a range of biological processes, including loss of neurons viability, higher accumulation of ROS and lipid peroxidation, and an increase of AChE activity. Evaluating the results we obtained, the concentration of $AlCl_3$ that best reproduced AD symptoms was 200 μM, which is the value to be used for further assays, and the SH-SY5Y cell line seems to be a good *in vitro* neuronal model to evaluate the toxicity induce by this metal.

The second AD model we intended to establish was in zebrafish embryos. This model complemented the previous study, since we worked with a reliable animal model with several advantages, such as their CNS similarity with those of mammals, that allowed the better understanding of the $AlCl_3$ induced neurotoxicity. Exposure to both concentrations of $AlCl_3$ lead to cardiotoxicity, pericardial edema, development delays, apoptotic neuromasts and lipid peroxidation. However, the concentration of 200 μM of $AlCl_3$ did not induced effects in the AChE activity and almost no apoptosis in neuromasts, while 50 μM greatly increased these parameters. These results contributed to elucidate that the 50 μM concentration of $AlCl_3$ is the best option to use in this *in vivo* model to evaluate modulation of AD-like symptoms. In summary, this study showed that the concentration of 50 μM of $AlCl_3$ causes changes in brain AChE activity, and in phenotypic parameters in zebrafish embryos, with the increased AChE activity possibly being involved in the neurotoxic effects induced by this metal. The few reports in the literature, together with our promising results, suggest that there is a need for further experiments to elucidate the mechanisms underlying the aluminium-induced neurotoxicity, including assays to assess its influence on the Tau and Aβ proteins, and studies in more complex animals, such as mouses to better validate these models. A further characterization of Tau phosphorylation is needed, due to its relevance in this disease. However, as no mutations on this protein are known, its study is very complex and the mechanisms of Tau destabilization, accumulation and aggregation need to be further explored in the future. Overall, we believe that the two AD models proposed in this thesis were successfully established and can be useful tools in the research of therapeutical pharmaceutical options for AD.

RNA therapeutics have been a rapidly growing area in the past few years and its application in AD treatment can be a promising strategy. However, for RNA molecules to cross the BBB and reach the target, they need to be vehiculated by safe and effective nanovectors, such as the exosome-like liposomes, which are novel systems that possess several advantages when compared to the natural exosomes. The exosome-like liposomes successfully encapsulated two types of RNA (siRNA and mRNA), with high encapsulation efficiencies, and had sizes of approximately 150 nm and a PDI around 0.2. Hence, these systems have promising characteristics, such as small size, with a monodisperse size population, and a lipidic composition, that potentiate BBB crossing. Overall, these systems proved to be stable in conditions mimicking those of the human body, when simulating the acidic environment of the lysosome, and when mimicking the interaction with serum proteins. We also demonstrated that siRNA loaded exosome-like liposomes were internalized by the cells after 3h of incubation. In the future, we will complete this study testing the uptake of Luciferase encoding mRNA encapsulated in these systems, to observe mRNA translation in the cells. Additionally, we will study the uptake of these systems, using an inhibitor of endocytosis, in order to infer the internalization pathway of the exosome-like liposomes.

After the establishment of the AD models, we evaluated the capacity of the exosome-like liposomes, loaded with anti-Tau siRNA and curcumin against AD-like toxicity in zebrafish embryos. These systems were successfully delivered since it was possible to verify the action of the anti-Tau siRNA and curcumin in the pre-established hallmarks, as we observed a decrease of the AChE activity when these systems were applied. This is also indicative that the exosome-like liposomes are reaching the brain of the zebrafish, since this enzyme is pervasive in the brain. In the future, it would be also interesting to study the effect of these systems in more complex AD models, but, overall, the results presented in this thesis showed that they have great promise for the treatment of several AD hallmarks.

Finally, petrosamine proved to be a safe, potent inhibitor of AChE in both established AD models, but further assays should be conducted in order to find its mechanism of action, and if it has potential in the treatment against other AD hallmarks. Additionally, petrosamine can be encapsulated in exosome-like liposomes for a targeted delivery.

7. References

1. Wilson, D. M. *et al.* Hallmarks of neurodegenerative diseases. *Cell* **186**, 693–714 (2023).
2. Forrest, S. L. & Kovacs, G. G. Current Concepts of Mixed Pathologies in Neurodegenerative Diseases. *Can. J. Neurol. Sci.* 1–17 (2022) doi:10.1017/cjn.2022.34.
3. Lamptey, R. N. L. *et al.* A Review of the Common Neurodegenerative Disorders: Current Therapeutic Approaches and the Potential Role of Nanotherapeutics. *IJMS* **23**, 1851 (2022).
4. Bloomingdale, P. *et al.* Hallmarks of neurodegenerative disease: A systems pharmacology perspective. *CPT Pharmacom & Syst Pharma* **11**, 1399–1429 (2022).
5. Sweeney, P. *et al.* Protein misfolding in neurodegenerative diseases: implications and strategies. *Transl Neurodegener* **6**, 6 (2017).
6. Wei, Z. *et al.* Synaptic Secretion and Beyond: Targeting Synapse and Neurotransmitters to Treat Neurodegenerative Diseases. *Oxidative Medicine and Cellular Longevity* **2022**, 1–22 (2022).
7. DeTure, M. A. & Dickson, D. W. The neuropathological diagnosis of Alzheimer's disease. *Mol Neurodegeneration* **14**, 32 (2019).
8. Scheltens, P. *et al.* Alzheimer's disease. *The Lancet* **397**, 1577–1590 (2021).

9. The top 10 causes of death. https://www.who.int/news-room/fact-sheets/detail/the-top-10-causes-of-death.

10. Li, X. *et al.* Global, regional, and national burden of Alzheimer's disease and other dementias, 1990–2019. *Front. Aging Neurosci.* **14**, 937486 (2022).

11. Salahuddin, P. *et al.* The role of amyloids in Alzheimer's and Parkinson's diseases. *International Journal of Biological Macromolecules* **190**, 44–55 (2021).

12. García-Ayllón, M.-S. Revisiting the role of acetylcholinesterase in Alzheimer's disease: cross-talk with P-tau and β-amyloid. *Front. Mol. Neurosci.* **4**, (2011).

13. Meftah, S. & Gan, J. Alzheimer's disease as a synaptopathy: Evidence for dysfunction of synapses during disease progression. *Front. Synaptic Neurosci.* **15**, 1129036 (2023).

14. Yu, H. & Wu, J. Amyloid-β: A double agent in Alzheimer's disease? *Biomedicine & Pharmacotherapy* **139**, 111575 (2021).

15. Roda, A., Serra-Mir, G., Montoliu-Gaya, L., Tiessler, L. & Villegas, S. Amyloid-beta peptide and tau protein crosstalk in Alzheimer's disease. *Neural Regen Res* **17**, 1666 (2022).

16. Sehar, U., Rawat, P., Reddy, A. P., Kopel, J. & Reddy, P. H. Amyloid Beta in Aging and Alzheimer's Disease. *IJMS* **23**, 12924 (2022).

17. Tatulian, S. A. Challenges and hopes for Alzheimer's disease. *Drug Discovery Today* **27**, 1027–1043 (2022).

18. Naseri, N. N., Wang, H., Guo, J., Sharma, M. & Luo, W. The complexity of tau in Alzheimer's disease. *Neuroscience Letters* **705**, 183–194 (2019).

19. d'Errico, P. & Meyer-Luehmann, M. Mechanisms of Pathogenic Tau and Aβ Protein Spreading in Alzheimer's Disease. *Front. Aging Neurosci.* **12**, 265 (2020).

20. Gao, Y.-L. *et al.* Tau in neurodegenerative disease. *Ann. Transl. Med.* **6**, 175–175 (2018).

21. Chong, F. P., Ng, K. Y., Koh, R. Y. & Chye, S. M. Tau Proteins and Tauopathies in Alzheimer's Disease. *Cell Mol Neurobiol* **38**, 965–980 (2018).

22. Zhou, Y., Zhen, Y., Wang, G. & Liu, B. Deconvoluting the Complexity of Reactive Oxygen Species (ROS) in Neurodegenerative Diseases. *Front. Neuroanat.* **16**, 910427 (2022).

23. Agrawal, I. & Jha, S. Mitochondrial Dysfunction and Alzheimer's Disease: Role of Microglia. *Front. Aging Neurosci.* **12**, 252 (2020).

24. Bai, R., Guo, J., Ye, X.-Y., Xie, Y. & Xie, T. Oxidative stress: The core pathogenesis and mechanism of Alzheimer's disease. *Ageing Research Reviews* **77**, 101619 (2022).

25. Birla, H., Minocha, T., Kumar, G., Misra, A. & Singh, S. K. Role of Oxidative Stress and Metal Toxicity in the Progression of Alzheimer's Disease. *CN* **18**, 552–562 (2020).

26. Reed, T. T. Lipid peroxidation and neurodegenerative disease. *Free Radical Biology and Medicine* **51**, 1302–1319 (2011).

27. Marucci, G. *et al.* Efficacy of acetylcholinesterase inhibitors in Alzheimer's disease. *Neuropharmacology* **190**, 108352 (2021).

28. Vecchio, I., Sorrentino, L., Paoletti, A., Marra, R. & Arbitrio, M. The State of The Art on Acetylcholinesterase Inhibitors in the Treatment of Alzheimer's Disease. *J Cent Nerv Syst Dis* **13**, 117957352110291 (2021).

29. Vecchio, I., Sorrentino, L., Paoletti, A., Marra, R. & Arbitrio, M. The State of The Art on Acetylcholinesterase Inhibitors in the Treatment of Alzheimer's Disease. *J Cent Nerv Syst Dis* **13**, 117957352110291 (2021).

30. Fish, P. V., Steadman, D., Bayle, E. D. & Whiting, P. New approaches for the treatment of Alzheimer's disease. *Bioorganic & Medicinal Chemistry Letters* **29**, 125–133 (2019).

31. Conti Filho, C. E. *et al.* Advances in Alzheimer's disease's pharmacological treatment. *Front. Pharmacol.* **14**, 1101452 (2023).

32. Yiannopoulou, K. G., Anastasiou, A. I., Zachariou, V. & Pelidou, S.-H. Reasons for Failed Trials of Disease-Modifying Treatments for Alzheimer Disease and Their Contribution in Recent Research. *Biomedicines* **7**, 97 (2019).

33. Behl, T. *et al.* AChE as a spark in the Alzheimer's blaze – Antagonizing effect of a cyclized variant. *Ageing Research Reviews* **83**, 101787 (2023).

34. Drummond, E. & Wisniewski, T. Alzheimer's disease: experimental models and reality. *Acta Neuropathol* **133**, 155–175 (2017).

35. Sweeney, M. D., Sagare, A. P. & Zlokovic, B. V. Blood–brain barrier breakdown in Alzheimer disease and other neurodegenerative disorders. *Nat Rev Neurol* **14**, 133–150 (2018).

36. Daneman, R. & Prat, A. The Blood–Brain Barrier. *Cold Spring Harb Perspect Biol* **7**, a020412 (2015).

37. Pardridge, W. M. Treatment of Alzheimer's Disease and Blood–Brain Barrier Drug Delivery. *Pharmaceuticals* **13**, 394 (2020).

38. López-Ornelas, A. *et al.* The Impairment of Blood-Brain Barrier in Alzheimer's Disease: Challenges and Opportunities with Stem Cells. *IJMS* **23**, 10136 (2022).

39. Wu, D. *et al.* The blood–brain barrier: structure, regulation, and drug delivery. *Sig Transduct Target Ther* **8**, 217 (2023).

40. Sharma, N. S., Karan, A., Lee, D., Yan, Z. & Xie, J. Advances in Modeling Alzheimer's Disease In Vitro. *Advanced NanoBiomed Research* **1**, 2100097 (2021).

41. Vignon, A., Salvador-Prince, L., Lehmann, S., Perrier, V. & Torrent, J. Deconstructing Alzheimer's Disease: How to Bridge the Gap between Experimental Models and the Human Pathology? *IJMS* **22**, 8769 (2021).

42. Sini, P. *et al.* Cyanobacteria, Cyanotoxins, and Neurodegenerative Diseases: Dangerous Liaisons. *IJMS* **22**, 8726 (2021).

43. Vilariño, N. *et al.* Human Poisoning from Marine Toxins: Unknowns for Optimal Consumer Protection. *Toxins* **10**, 324 (2018).

44. Hu, Y., Chen, J., Fan, H., Xie, P. & He, J. A review of neurotoxicity of microcystins. *Environ Sci Pollut Res* **23**, 7211–7219 (2016).

45. Islam, F. *et al.* Exposure of metal toxicity in Alzheimer's disease: An extensive review. *Front. Pharmacol.* **13**, 903099 (2022).

46. Vasefi, M., Ghaboolian-Zare, E., Abedelwahab, H. & Osu, A. Environmental toxins and Alzheimer's disease progression. *Neurochemistry International* **141**, 104852 (2020).

47. Kawahara, M. & Kato-Negishi, M. Link between Aluminum and the Pathogenesis of Alzheimer's Disease: The Integration of the Aluminum and Amyloid Cascade Hypotheses. *International Journal of Alzheimer's Disease* **2011**, 1–17 (2011).

48. Wang, Z. *et al.* Chronic exposure to aluminum and risk of Alzheimer's disease: A meta-analysis. *Neuroscience Letters* **610**, 200–206 (2016).

49. Huat, T. J. *et al.* Metal Toxicity Links to Alzheimer's Disease and Neuroinflammation. *Journal of Molecular Biology* **431**, 1843–1868 (2019).

50. Song, J. Animal Model of Aluminum-Induced Alzheimer's Disease. in *Neurotoxicity of Aluminum* (ed. Niu, Q.) vol. 1091 113–127 (Springer Singapore, 2018).

51. Savory, J. Intracellular mechanisms underlying aluminum-induced apoptosis in rabbit brain. *Journal of Inorganic Biochemistry* **97**, 151–154 (2003).

52. Radagdam, S. *et al.* Evaluation of dihydrotestosterone and dihydroprogesterone levels and gene expression of genes involved in neurosteroidogenesis in the SH-SY5Y Alzheimer disease cell model. *Front. Neurosci.* **17**, 1163806 (2023).

53. Agholme, L., Lindström, T., Kågedal, K., Marcusson, J. & Hallbeck, M. An In Vitro Model for Neuroscience: Differentiation of SH-SY5Y Cells into Cells with Morphological and Biochemical Characteristics of Mature Neurons. *JAD* **20**, 1069–1082 (2010).

54. Akhtar, A. *et al.* Preclinical Models for Alzheimer's Disease: Past, Present, and Future Approaches. *ACS Omega* **7**, 47504–47517 (2022).

55. Kalueff, A. V., Stewart, A. M. & Gerlai, R. Zebrafish as an emerging model for studying complex brain disorders. *Trends in Pharmacological Sciences* **35**, 63–75 (2014).

56. Ribas, L. & Piferrer, F. The zebrafish (*Danio rerio*) as a model organism, with emphasis on applications for finfish aquaculture research. *Rev Aquacult* **6**, 209–240 (2014).

57. Adhish, M. & Manjubala, I. Effectiveness of zebrafish models in understanding human diseases—A review of models. *Heliyon* **9**, e14557 (2023).

58. Choi, T.-Y., Choi, T.-I., Lee, Y.-R., Choe, S.-K. & Kim, C.-H. Zebrafish as an animal model for biomedical research. *Exp Mol Med* **53**, 310–317 (2021).

59. Saleem, S. & Kannan, R. R. Zebrafish: an emerging real-time model system to study Alzheimer's disease and neurospecific drug discovery. *Cell Death Discov.* **4**, 45 (2018).

60. Noori, T., Dehpour, A. R., Sureda, A., Sobarzo-Sanchez, E. & Shirooie, S. Role of natural products for the treatment of Alzheimer's disease. *European Journal of Pharmacology* **898**, 173974 (2021).

61. Andrade, S., Ramalho, M. J., Loureiro, J. A. & Pereira, M. D. C. Natural Compounds for Alzheimer's Disease Therapy: A Systematic Review of Preclinical and Clinical Studies. *IJMS* **20**, 2313 (2019).

62. Ribeiro, J., Lopes, I. & Gomes, A. C. *A New Perspective for the Treatment of Alzheimer's Disease: Exosome-Like Liposomes to Deliver Natural Compounds and RNA Therapies*. https://www.preprints.org/manuscript/202306.1273/v1 (2023) doi:10.20944/preprints202306.1273.v1.

63. Da Rosa, M. M. *et al.* The promising role of natural products in Alzheimer's disease. *Brain Disorders* **7**, 100049 (2022).

64. Gartshore, C. J., Wang, X., Su, Y. & Molinski, T. F. Petrosamine Revisited. Experimental and Computational Investigation of Solvatochromism, Tautomerism and Free Energy Landscapes of a Pyridoacridinium Quaternary Salt. *Marine Drugs* **21**, 446 (2023).

65. Nukoolkarn, V. S. *et al.* Petrosamine, a potent anticholinesterase pyridoacridine alkaloid from a Thai marine sponge Petrosia n. sp. *Bioorganic & Medicinal Chemistry* **16**, 6560–6567 (2008).

66. Shabbir, U., Rubab, M., Tyagi, A. & Oh, D.-H. Curcumin and Its Derivatives as Theranostic Agents in Alzheimer's Disease: The Implication of Nanotechnology. *IJMS* **22**, 196 (2020).

67. Chen, M. *et al.* Use of curcumin in diagnosis, prevention, and treatment of Alzheimer's disease. *Neural Regen Res* **13**, 742 (2018).

68. Bhat, B. A. *et al.* Natural Therapeutics in Aid of Treating Alzheimer's Disease: A Green Gateway Toward Ending Quest for Treating Neurological Disorders. *Front. Neurosci.* **16**, 884345 (2022).

69. Zogg, H., Singh, R. & Ro, S. Current Advances in RNA Therapeutics for Human Diseases. *IJMS* **23**, 2736 (2022).

70. Wu, Y., Ng, D. Y. W., Kuan, S. L. & Weil, T. Protein–polymer therapeutics: a macromolecular perspective. *Biomater. Sci.* **3**, 214–230 (2015).

71. Kim, Y.-K. RNA therapy: rich history, various applications and unlimited future prospects. *Exp Mol Med* (2022) doi:10.1038/s12276-022-00757-5.

72. Feng, R., Patil, S., Zhao, X., Miao, Z. & Qian, A. RNA Therapeutics - Research and Clinical Advancements. *Front. Mol. Biosci.* **8**, 710738 (2021).

73. Damase, T. R. *et al.* The Limitless Future of RNA Therapeutics. *Front. Bioeng. Biotechnol.* **9**, 628137 (2021).

74. Niazi, S. K. RNA Therapeutics: A Healthcare Paradigm Shift. *Biomedicines* **11**, 1275 (2023).

75. Zhu, Y., Zhu, L., Wang, X. & Jin, H. RNA-based therapeutics: an overview and prospectus. *Cell Death Dis* **13**, 644 (2022).

76. Manczak, M. & Reddy, P. H. RNA silencing of genes involved in Alzheimer's disease enhances mitochondrial function and synaptic activity. *Biochimica et Biophysica Acta (BBA) - Molecular Basis of Disease* **1832**, 2368–2378 (2013).

77. Wang, P. *et al.* Systemic delivery of BACE1 siRNA through neuron-targeted nanocomplexes for treatment of Alzheimer's disease. *Journal of Controlled Release* **279**, 220–233 (2018).

78. Senechal, Y., Kelly, P. H., Cryan, J. F., Natt, F. & Dev, K. K. Amyloid precursor protein knockdown by siRNA impairs spontaneous alternation in adult mice: *In vivo* knockdown of APP by RNAi. *Journal of Neurochemistry* **102**, 1928–1940 (2007).

79. Smilansky, A. *et al.* The Voltage-dependent Anion Channel 1 Mediates Amyloid β Toxicity and Represents a Potential Target for Alzheimer Disease Therapy. *Journal of Biological Chemistry* **290**, 30670–30683 (2015).

80. Xu, H. *et al.* Tau Silencing by siRNA in the P301S Mouse Model of Tauopathy. *CGT* **14**, 343–351 (2014).

81. Kandimalla, R. J., Wani, W. Y., Bk, B. & Gill, K. D. siRNA against presenilin 1 (PS1) down regulates amyloid b42 production in IMR-32 cells. (2012).

82. Lin, C.-Y. *et al.* Messenger RNA-based therapeutics for brain diseases: An animal study for augmenting clearance of beta-amyloid by intracerebral administration of

neprilysin mRNA loaded in polyplex nanomicelles. *Journal of Controlled Release* **235**, 268–275 (2016).

83. Shin, H. *et al.* Recent Advances in RNA Therapeutics and RNA Delivery Systems Based on Nanoparticles. *Adv. Therap.* **1**, 1800065 (2018).
84. Teleanu, D., Chircov, C., Grumezescu, A., Volceanov, A. & Teleanu, R. Blood-Brain Delivery Methods Using Nanotechnology. *Pharmaceutics* **10**, 269 (2018).
85. Thi, T. T. H. *et al.* Lipid-Based Nanoparticles in the Clinic and Clinical Trials: From Cancer Nanomedicine to COVID-19 Vaccines. *Vaccines* **9**, 359 (2021).
86. Nsairat, H. *et al.* Liposomes: structure, composition, types, and clinical applications. *Heliyon* **8**, e09394 (2022).
87. García-Pinel, B. *et al.* Lipid-Based Nanoparticles: Application and Recent Advances in Cancer Treatment. *Nanomaterials* **9**, 638 (2019).
88. Betzer, O. *et al.* The effect of nanoparticle size on the ability to cross the blood–brain barrier: an *in vivo* study. *Nanomedicine* **12**, 1533–1546 (2017).
89. Kong, F.-Y. *et al.* Unique Roles of Gold Nanoparticles in Drug Delivery, Targeting and Imaging Applications. *Molecules* **22**, 1445 (2017).
90. Zhu, Y., Liu, C. & Pang, Z. Dendrimer-Based Drug Delivery Systems for Brain Targeting. *Biomolecules* **9**, 790 (2019).
91. Ribovski, L., Hamelmann, N. M. & Paulusse, J. M. J. Polymeric Nanoparticles Properties and Brain Delivery. *Pharmaceutics* **13**, 2045 (2021).

92. Calabrese, G. *et al.* Carbon Dots: An Innovative Tool for Drug Delivery in Brain Tumors. *IJMS* **22**, 11783 (2021).

93. Doyle, L. & Wang, M. Overview of Extracellular Vesicles, Their Origin, Composition, Purpose, and Methods for Exosome Isolation and Analysis. *Cells* **8**, 727 (2019).

94. Gurung, S., Perocheau, D., Touramanidou, L. & Baruteau, J. The exosome journey: from biogenesis to uptake and intracellular signalling. *Cell Commun Signal* **19**, 47 (2021).

95. Rech, J., Getinger-Panek, A., Gałka, S. & Bednarek, I. Origin and Composition of Exosomes as Crucial Factors in Designing Drug Delivery Systems. *Applied Sciences* **12**, 12259 (2022).

96. Burtenshaw, D. *et al.* Exosomal Composition, Biogenesis and Profiling Using Point-of-Care Diagnostics—Implications for Cardiovascular Disease. *Front. Cell Dev. Biol.* **10**, 853451 (2022).

97. García-Fernández, J. & Fuente Freire, M. D. L. Exosome-like systems: Nanotechnology to overcome challenges for targeted cancer therapies. *Cancer Letters* **561**, 216151 (2023).

98. Antimisiaris, S., Mourtas, S. & Marazioti, A. Exosomes and Exosome-Inspired Vesicles for Targeted Drug Delivery. *Pharmaceutics* **10**, 218 (2018).

99. Abdellatif, A. A. H. *et al.* Lipid nanoparticles technology in vaccines: Shaping the future of prophylactic medicine. *Colloids and Surfaces B: Biointerfaces* **222**, 113111 (2023).

100. Swetha, K. *et al.* Recent Advances in the Lipid Nanoparticle-Mediated Delivery of mRNA Vaccines. *Vaccines* **11**, 658 (2023).

101. Vieira, D. & Gamarra, L. Getting into the brain: liposome-based strategies for effective drug delivery across the blood–brain barrier. *IJN* **Volume 11**, 5381–5414 (2016).

102. Fernandes, M. *et al.* Novel concept of exosome-like liposomes for the treatment of Alzheimer's disease. *Journal of Controlled Release* **336**, 130–143 (2021).

103. Dekevic, G., Tasto, L., Czermak, P. & Salzig, D. Statistical experimental designs to optimize the transient transfection of HEK 293T cells and determine a transfer criterion from adherent cells to larger-scale cell suspension cultures. *Journal of Biotechnology* **346**, 23–34 (2022).

104. Monaco, A., Grimaldi, M. C. & Ferrandino, I. Aluminium chloride-induced toxicity in zebrafish larvae. *J Fish Dis* **40**, 629–635 (2017).

105. Barai, P., Raval, N., Acharya, S. & Acharya, N. Neuroprotective effects of Bergenia ciliata on NMDA induced injury in SH-SY5Y cells and attenuation of cognitive deficits in scopolamine induced amnesia in rats. *Biomedicine & Pharmacotherapy* **108**, 374–390 (2018).

106. Vajrabhaya, L. & Korsuwannawong, S. Cytotoxicity evaluation of a Thai herb using tetrazolium (MTT) and sulforhodamine B (SRB) assays. *J Anal Sci Technol* **9**, 15 (2018).

107. Mascotti, K., McCullough, J. & Burger, S. R. HPC viability measurement: trypan blue versus acridine orange and propidium iodide. *Transfusion* **40**, 693–696 (2000).

108. Ellman, G. L., Courtney, K. D., Andres, V. & Featherstone, R. M. A new and rapid colorimetric determination of acetylcholinesterase activity. *Biochemical Pharmacology* **7**, 88–95 (1961).

109. Sun, W. *et al.* Study of acetylcholinesterase activity and apoptosis in SH-SY5Y cells and mice exposed to ethanol. *Toxicology* **384**, 33–39 (2017).

110. Braunbeck, T. *et al.* The fish embryo test (FET): origin, applications, and future. *Environ Sci Pollut Res* **22**, 16247–16261 (2015).

111. Capriello, T. *et al.* Apoptosis, oxidative stress and genotoxicity in developing zebrafish after aluminium exposure. *Aquatic Toxicology* **236**, 105872 (2021).

112. Leyden, C. *et al.* Efficacy of Tricaine (MS-222) and Hypothermia as Anesthetic Agents for Blocking Sensorimotor Responses in Larval Zebrafish. *Front. Vet. Sci.* **9**, 864573 (2022).

113. Gazsi, G. *et al.* Physiological, Developmental, and Biomarker Responses of Zebrafish Embryos to Sub-Lethal Exposure of Bendiocarb. *Water* **13**, 204 (2021).

114. Vieira, R. S. F., Venâncio, C. A. S. & Félix, L. M. Embryonic zebrafish response to a commercial formulation of azoxystrobin at environmental concentrations. *Ecotoxicology and Environmental Safety* **211**, 111920 (2021).

115. Gravato, C., Abe, F. R., de Oliveira, D. P., Soares, A. M. V. M. & Domingues, I. Acetylcholinesterase (AChE) Activity in Embryos of Zebrafish. in *Toxicity Assessment*

(eds. Palmeira, C. M. M., de Oliveira, D. P. & Dorta, D. J.) vol. 2240 119–124 (Springer US, 2021).

116. Shaker, S., Gardouh, A. & Ghorab, M. Factors affecting liposomes particle size prepared by ethanol injection method. *Res Pharma Sci* **12**, 346 (2017).

117. Gouda, A., Sakr, O. S., Nasr, M. & Sammour, O. Ethanol injection technique for liposomes formulation: An insight into development, influencing factors, challenges and applications. *Journal of Drug Delivery Science and Technology* **61**, 102174 (2021).

118. Fernandes, M. Development of nanocarriers for Alzheimer's disease treatment. (University of Minho, 2019).

119. Cullis, P. R. & Hope, M. J. Lipid Nanoparticle Systems for Enabling Gene Therapies. *Molecular Therapy* **25**, 1467–1475 (2017).

120. Falke, S. & Betzel, C. Dynamic Light Scattering (DLS): Principles, Perspectives, Applications to Biological Samples. in *Radiation in Bioanalysis* (eds. Pereira, A. S., Tavares, P. & Limão-Vieira, P.) vol. 8 173–193 (Springer International Publishing, 2019).

121. Danaei, M. *et al.* Impact of Particle Size and Polydispersity Index on the Clinical Applications of Lipidic Nanocarrier Systems. *Pharmaceutics* **10**, 57 (2018).

122. Raval, N. *et al.* Importance of Physicochemical Characterization of Nanoparticles in Pharmaceutical Product Development. in *Basic Fundamentals of Drug Delivery* 369–400 (Elsevier, 2019). doi:10.1016/B978-0-12-817909-3.00010-8.

123. Huang, G. *et al.* Symmetric electrophoretic light scattering for determination of the zeta potential of colloidal systems. *Colloids and Surfaces A: Physicochemical and Engineering Aspects* **587**, 124339 (2020).

124. Markova, N. *et al.* Biophysical Characterization of Viral and Lipid-Based Vectors for Vaccines and Therapeutics with Light Scattering and Calorimetric Techniques. *Vaccines* **10**, 49 (2021).

125. Jones, L. J., Yue, S. T., Cheung, C.-Y. & Singer, V. L. RNA Quantitation by Fluorescence-Based Solution Assay: RiboGreen Reagent Characterization. *Analytical Biochemistry* **265**, 368–374 (1998).

126. Shao, X.-R. *et al.* Effects of Micro-environmental pH of Liposome on Chemical Stability of Loaded Drug. *Nanoscale Res Lett* **12**, 504 (2017).

127. Cazzola, R., Viani, P., Allevi, P., Cighetti, G. & Cestaro, B. pH sensitivity and plasma stability of liposomes containing N-stearoylcysteamine. *Biochimica et Biophysica Acta (BBA) - Biomembranes* **1329**, 291–301 (1997).

128. Bonté, F. & Juliano, R. L. Interactions of liposomes with serum proteins. *Chemistry and Physics of Lipids* **40**, 359–372 (1986).

129. Aylward, L. L. Biomarkers of Environmental Exposures in Blood.

130. Dobrovolskaia, M. A. *et al.* Method for Analysis of Nanoparticle Hemolytic Properties in Vitro. *Nano Lett.* **8**, 2180–2187 (2008).

131. Koley, D. & Bard, A. J. Triton X-100 concentration effects on membrane permeability of a single HeLa cell by scanning electrochemical microscopy (SECM). *Proc. Natl. Acad. Sci. U.S.A.* **107**, 16783–16787 (2010).

132. Du, J., Zhao, L., Kang, Q., He, Y. & Bi, Y. An optimized method for Oil Red O staining with the salicylic acid ethanol solution. *Adipocyte* **12**, 2179334 (2023).

133. Ferreira, T. Development of nanocarriers for the treatment of Alzheimer's disease. (University of Minho, 2021).

134. Meyer, R. A., Hussmann, G. P., Peterson, N. C., Santos, J. L. & Tuesca, A. D. A scalable and robust cationic lipid/polymer hybrid nanoparticle platform for mRNA delivery. *International Journal of Pharmaceutics* **611**, 121314 (2022).

135. Avci-Adali, M. *et al.* Optimized conditions for successful transfection of human endothelial cells with in vitro synthesized and modified mRNA for induction of protein expression. *J Biol Eng* **8**, 8 (2014).

136. Gomes, N. Development of neuroprotective lipid nanocarriers for Alzheimer's disease. (University of Minho, 2023).

137. Bruce, A. E. E. Zebrafish epiboly: Spreading thin over the yolk. *Developmental Dynamics* **245**, 244–258 (2016).

138. Manuel, R., Iglesias Gonzalez, A. B., Habicher, J., Koning, H. K. & Boije, H. Characterization of Individual Projections Reveal That Neuromasts of the Zebrafish Lateral Line are Innervated by Multiple Inhibitory Efferent Cells. *Front. Neuroanat.* **15**, 666109 (2021).

139. Kumar, P., Nagarajan, A. & Uchil, P. D. Analysis of Cell Viability by the Lactate Dehydrogenase Assay. *Cold Spring Harb Protoc* **2018**, pdb.prot095497 (2018).

140. Mustafa Rizvi, S. H. *et al.* Aluminium Induced Endoplasmic Reticulum Stress Mediated Cell Death in SH-SY5Y Neuroblastoma Cell Line Is Independent of p53. *PLoS ONE* **9**, e98409 (2014).

141. Yang, M.-H. *et al.* Reduction of aluminum ion neurotoxicity through a small peptide application – NAP treatment of Alzheimer's disease. *Journal of Food and Drug Analysis* **27**, 551–564 (2019).

142. Biswas, K., Alexander, K. & Francis, M. M. Reactive Oxygen Species: Angels and Demons in the Life of a Neuron. *NeuroSci* **3**, 130–145 (2022).

143. Su, L.-J. *et al.* Reactive Oxygen Species-Induced Lipid Peroxidation in Apoptosis, Autophagy, and Ferroptosis. *Oxidative Medicine and Cellular Longevity* **2019**, 1–13 (2019).

144. Ferretti, G., Marchionni, C., Bacchetti, T., Galeazzi, T. & Dousset, N. Effect of Aluminium on Lipid Peroxidation of Human High Density Lipoproteins. *Free Radical Research* **37**, 515–521 (2003).

145. Hattori, Y. *et al.* Optimal combination of cationic lipid and phospholipid in cationic liposomes for gene knockdown in breast cancer cells and mouse lung using siRNA lipoplexes. *Mol Med Rep* **26**, 253 (2022).

146. Ji, A. *et al.* Lipid Microparticles Show Similar Efficacy With Lipid Nanoparticles in Delivering mRNA and Preventing Cancer. *Pharm Res* **40**, 265–279 (2023).

147. Tang, M. *et al.* Efficient mRNA Delivery with mRNA Lipoplexes Prepared Using a Modified Ethanol Injection Method. *Pharmaceutics* **15**, 1141 (2023).

148. Smith, S. A., Selby, L. I., Johnston, A. P. R. & Such, G. K. The Endosomal Escape of Nanoparticles: Toward More Efficient Cellular Delivery. *Bioconjugate Chem.* **30**, 263–272 (2019).

149. Zaremba-Czogalla, M. *et al.* Evaluation of the In Vitro Cytotoxic Activity of Caffeic Acid Derivatives and Liposomal Formulation against Pancreatic Cancer Cell Lines. *Materials* **13**, 5813 (2020).

150. Tanaka, H. *et al.* In Vivo Introduction of mRNA Encapsulated in Lipid Nanoparticles to Brain Neuronal Cells and Astrocytes via Intracerebroventricular Administration. *Mol. Pharmaceutics* **15**, 2060–2067 (2018).

151. Rassu, G. *et al.* Nose-to-brain delivery of BACE1 siRNA loaded in solid lipid nanoparticles for Alzheimer's therapy. *Colloids and Surfaces B: Biointerfaces* **152**, 296–301 (2017).

152. Neurotoxicity of aluminum and its link to neurodegenerative diseases. (2021).

153. Akinyemi, A. J., Oboh, G., Fadaka, A. O., Olatunji, B. P. & Akomolafe, S. Curcumin administration suppress acetylcholinesterase gene expression in cadmium treated rats. *NeuroToxicology* **62**, 75–79 (2017).